SCUOLA DI DOTTORATO
UNIVERSITÀ DEGLI STUDI DI MILANO-BICOCCA

Dipartimento di / Department of
Fisica G. Occhialini

Dottorato di Ricerca in / PhD program in Fisica e Astronomia Ciclo / Cycle XXX

Curriculum in Fisica della Materia Condensata, Fisica dei plasmi e Biofisica

Development of neutron and gamma-ray spectrometers for fusion plasma applications

Cognome / Surname: Rigamonti Nome / Name: Davide

Matricola / Registration number: 710015

Tutore / Tutor: Dr. Marco Tardocchi

Coordinatore / Coordinator: Prof. Marta Calvi

ACADEMIC YEAR 2016 / 2017

A Mio Zio Mario,
a Mamma, Papà e Nicolò,
a Federica.

Riassunto

Il plasma è una forte sorgente di neutroni e raggi gamma i quali, essendo neutri, sfuggono dal volume di plasma e possono essere rivelati mediante tecniche non invasive. I neutroni sono emessi dalle reazioni di fusione e trasportano informazioni dirette sugli ioni di combustibile. L'emissione di raggi gamma, invece, avviene attraverso reazioni tra particelle cariche veloci e le impurezze presenti nel plasma. Nei futuri reattori a fusione nucleare di alta potenza, la spettroscopia gamma e di neutroni potrebbero essere le sole diagnostiche di ioni veloci funzionanti. L'alto flusso neutronico e gamma previsto al JET per plasmi DT, insieme alla necessità di fornire misure con risoluzione temporale di 10-100 ms, richiedono l'utilizzo di spettrometri in grado di operare a tassi di conteggio nel range del MHz. Inoltre, il bisogno di misure ad alta risoluzione energetica pone ulteriori vincoli sulle prestazioni dei rivelatori. Questa tesi si è incentrata sullo sviluppo, la caratterizzazione e l'implementazione di nuovi rivelatori compatti ad alta risoluzione per la spettroscopia di neutroni e raggi gamma in grado di operare ad altissimi tassi di conteggio. All'interno di un progetto europeo finalizzato all'aggiornamento della gamma camera (GC) del JET, è stato sviluppato un prototipo di spettrometro gamma compatto basato su un cristallo a scintillazione $LaBr_3$ accoppiato ad un Silicon PhotoMultiplier (SIPM). Lo spettrometro offre una buona risoluzione energetica del 5% a 662 keV che migliora a energie più alte permettendo misure accurate di raggi gamma nel range energetico 2-6 MeV. Il rivelatore implementa un circuito di formatura del segnale dedicato in grado di accorciare la durata temporale del segnale in uscita dal SiPM. Ciò permette di minimizzare la presenza di eventi di pile-up consentendo il funzionamento a tassi di conteggio superiori a 1 MCounts/s. Presso l'acceleratore di Legnaro è stata dimostrata la capacità di operare fino a 3 MCounts/s. I 19 rivelatori sono stati calibrati e installati nella GC del JET nel 2017 e sono pronti a raccogliere dati nelle prossime campagne. L'avanzata risoluzione energetica della GC permetterà di evitare artefatti nella ricostruzione del profilo degli ioni veloci, mentre l'alta capacità di conteggio permetterà per la prima volta di monitorare i cambiamenti del profilo ionico in tempi comparabili al loro tempo caratteristico di rallentamento. Per quanto riguarda la spettroscopia neutronica, una matrice di 12 diamanti monocristallini è stata installata lungo una linea di vista verticale del JET permettendo misure simultanee di neutroni da 2.5 MeV e 14 MeV. La risposta dei diamanti ai neutroni dipende fortemente dalla loro energia. Per neutroni da 2.5 MeV, la risposta è dominata dallo scattering elastico e anelastico sul carbonio mentre per neutroni da 14 MeV si aprono diversi canali di reazione, che permettono misure di spettroscopia ad alta risoluzione. La funzione di risposta della matrice di diamanti è stata misurata per neutroni monoenergetici presso acceleratori nucleari a diverse energie. La validazione della matrice di diamanti con neutroni da 2.5 MeV è stata eseguita confrontando i dati

misurati dallo spettrometro di riferimento al JET, cioè il TOFOR. I risultati hanno evidenziato il corretto funzionamento della matrice e una moderata risoluzioni energetica per plasmi di D. Le eccellenti capacità spettroscopiche dei diamanti per neutroni da 14 MeV, sono state investigate durante la caratterizzazione di un generatore di neutroni DT. I neutroni sono prodotti dal generatore attraverso reazioni deuterio-trizio che avvengono tra il fascio di ioni misti $D_x^+/T_x^+/DT^+$ (x=1,2) accelerati verso il bersaglio imbevuto di D e T. I diamanti hanno permesso per la prima volta di risolvere le complesse strutture dello spettro di energia dei neutroni risultanti dalle diverse specie D^+, T^+, D_2^+, T_2^+, DT^+ presenti nel fascio. Questo risultato apre nuove prospettive per la diagnostica di plasmi DT su JET e ITER. L'analisi dettagliata del picco $^{12}C(n,\alpha)^9Be$ del diamante, infatti, permette di identificare in modo accurato le componenti sovra-termiche in plasmi DT e di studiare fenomeni non classici nel rallentamento degli ioni di fascio. I risultati presentati rappresentano un avanzamento nello sviluppo di spettrometri di neutroni e raggi gamma per la diagnostica di plasmi da fusione, che combinano la capacità di operare a tassi di conteggio del MHz con la buona risoluzione energetica. I rivelatori sviluppati offrono dimensioni estremamente compatte, ideali per l'integrazione in camere con linee di vista multiple sui futuri reattori a fusione come ITER e DEMO.

Summary

A burning plasma is a strong source of neutrons and gamma-rays which can escape the plasma volume and be detected providing information on fuel and fast ions. Unlike present mid-size tokamaks, in the next high power devices neutron and gamma-ray spectroscopy will benefit of the significant increment of neutrons and gamma-rays fluxes and might be the only working fast ion diagnostics. Neutrons are emitted by fusion reactions carrying information on the fuel ions, allowing measuring ion temperature T_i of the thermal plasma component and to diagnose the supra-thermal components. Gamma-rays emission in fusion plasmas comes from reactions between fuel nuclei or fast charged particles with plasma impurities. The high neutron and gamma-ray fluxes expected at JET in DT plasmas, together with the need to provide time resolution in the range of 10-100 ms, translates into the need of spectrometers capable to operate at counting rates in the MHz range. Moreover, measurements with high energy resolution are necessary to infer detailed information on fast and fuel ions. These pose very challenging requirements on the needed detector performances. This thesis is focused on the development, characterization and implementation of new compact gamma-ray and neutron spectrometers which combine high counting rate capabilities and high energy resolutions. A prototype compact gamma-ray spectrometer has been developed within a European project which is upgrading the JET gamma ray camera (GC) detectors. The prototype detector is based on a $LaBr_3$ scintillator crystal coupled to a Silicon PhotoMultiplier (SIPM). The developed prototype spectrometer features an energy resolution of 5% at 662 keV, which improves for higher energies and provides accurate measurements in the energy range up to a few MeVs. A suitable shaping circuit of the SIPM signal has been implemented to minimize the presence of piled up events allowing operation at counting rates in excess of 1 MCounts/s, as demonstrated with record values 3 MCounts/s at an accelerator. The 19 new detectors have been successfully calibrated and installed during 2017 in the JET GC and are ready to collect data in the next campaigns. The enhanced energy resolution of GC will allow avoiding artifacts in the reconstructed fast ions profile, while the improved time resolution will open the possibility to track for the first time the fast ions profile changes during their slowing down times. In the neutron spectroscopy field, a 12-pixels single crystal diamond matrix has been installed on a vertical line of sight of JET allowing simultaneous measurements of 2.5 MeV and 14 MeV neutrons. The response of diamond neutron spectrometers to 2.5 and 14 MeV neutrons is very different, namely it is dominated by elastic and inelastic scattering for 2.5 MeV neutrons while for 14 MeV neutrons several nuclear reaction channels open up, offering the possibility to perform high resolution spectroscopy. The diamond matrix response function has been measured at nuclear accelerators for incoming different monoenergetic neutron energies. The data

validation of the diamond matrix with 2.5 MeV neutrons has been performed by comparing with data taken by the reference 2.5 MeV neutron spectrometer at JET, namely TOFOR, which shares the same line of sight of the diamond. The results indicated that the spectrometer works well and can provide a moderated energy resolution in D plasmas. The excellent spectroscopic capabilities for 14 MeV neutrons, instead, has been explored during the characterization of a 14 MeV DT neutron generator at the National Physical Laboratory. Neutrons were produced by deuterium-tritium reactions occurring by accelerating a mixed beam of $D_x^+/T_x^+/DT^+$ ions (x=1,2) onto a titanium target containing T/D. Diamond detectors allowed resolving for the first time the complex features of the neutron energy spectra resulting from the simultaneous presence of D^+, T^+, D_2^+, T_2^+, DT^+ species in the beam. These results open up to new prospects for diagnosing DT plasmas on JET and ITER. The analysis of the diamond $^{12}C(n,\alpha)^9Be$ peak, in fact, will allow accurately identifying supra-thermal components in DT plasma operations and studying non classical phenomena on the beam slowing down. The results presented in this thesis represent a step forward in the development of neutron and gamma-ray spectrometers for fusion plasma diagnostics which combine the MHz counting rate capability with the enhanced energy resolution. The developed instruments feature compact size and are therefore suitable for integration in a multi line of sight camera on the next step burning plasma fusion devices such as ITER and DEMO.

List of papers

This thesis is based on the following papers, which are referred to in the text by their Roman numerals:

I. D. Rigamonti, A. Muraro, M. Nocente, V. Perseo, G. Boltruczyk, A. Fernandes, J. Figueiredo, L. Giacomelli, G. Gorini, M. Gosk, V. Kiptily, S. Korolczuk, S. Mianowski, A. Murari, R. C. Pereira, E. Perelli Cippo, I. Zychor, M. Tardocchi and JET Contributors, "*Performance of the prototype LaBr3 spectrometer developed for the JET gamma-ray camera upgrade*", Rev. Sci. Instrum., 87, 11E717 (2016)

II. M. Nocente, D. Rigamonti, V. Perseo, M. Tardocchi, G. Boltruczyk, A. Broslawski, A. Cremona, G. Croci, M. Gosk, V. Kiptily, S. Korolczuk, M. Mazzocco, A. Muraro, E. Strano, I. Zychor, G. Gorini and JET Contributors, "*Gamma-ray spectroscopy at MHz counting rates with a compact LaBr3 detector and silicon photomultipliers for fusion plasma applications*", Rev. Sci. Instrum., 87, 11E714 (2016)

III. D. Rigamonti, M. Nocente, L. Giacomelli, M. Tardocchi, M. Angelone, A. Broslawski, C. Cazzaniga, J. Figueiredo, G. Gorini, V. Kiptily, S. Korolczuk, A. Murari, M. Pillon, R. Pilotti, I. Zychor and JET Contributors, "*Characterization of a compact LaBr3(Ce) detector with Silicon photomultipliers at high 14 MeV neutron fluxes*" 2017 JINST 12 C10007

IV. D. Rigamonti, M. Tardocchi, C. Cazzaniga, M. Rebai, G. Croci, L.C. Giacomelli, G. Grosso, A. Muraro, M. Nocente, E. Perelli Cippo, P. Calvani, M. Gerolami, D. M.Trucchi, M. Angelone, M. Pillon, J. Figuereido, A. Murari, G. Gorini and JET Contributors, "*Capabilities of a Diamond Detector matrix for neutron spectroscopy measurements at JET*", Proceedings of the First EPS conference on Plasma Diagnostics, Proceedings of Science, PoS (ECPD2015) 061 (2015)

V. L. Giacomelli, M. Nocente, M. Rebai, D. Rigamonti, A. Milocco, M. Tardocchi, Z. J. Chen, T. F. Du, T. S. Fan, Z. M. Hu, X. Y. Peng, A. Hjalmarsson, G. Gorini and JET Contributors, "*Neutron emission spectroscopy of DT plasmas at enhanced energy resolution with diamond detectors*", Rev. Sci. Instrum., 87, 11D822 (2016)

VI. D. Rigamonti, L. Giacomelli, G. Gorini, M. Nocente, M. Rebai, M. Tardocchi, M. Angelone, P. Batistoni, A. Cufar, Z. Ghani, S. Jednorog, A. Klix, E.

Laszynska, S. Loreti, M. Pillon, S. Popovichev, N. Roberts, D. Thomas, "*Neutron spectroscopy measurements of 14 MeV neutrons at unprecedented energy resolution and implications for deuterium-tritium fusion plasma diagnostics*". 2018 Meas. Sci. Technol. https://doi.org/10.1088/1361-6501/aaa675

Papers published on peer-reviewed journals that were not included in this thesis:

VII P. Batistoni, S. Popovichev, A. Cufar, Z. Ghani, L. Giacomelli, S. Jednorog, A. Klix, S. Lilley, E. Laszynska, S. Loreti, L. Packer, A. Peacock, M. Pillon, R. Price, M. Rebai, D. Rigamonti, N. Roberts, M. Tardocchi, D. Thomas and JET Contributors, "*14 MeV calibration of JET neutron detectors-phase 1: calibration and characterization of the neutron source*", Nucl. Fusion 58 (2018) 026012

VIII S. Jednoroga, E. Laszynska, P. Batistoni, B. Bienkowska, A. Cufar, Z. Ghani, L. Giacomelli, A. Klix, S. Loreti, K. Mikszuta, L. Packer, A. Peacock, M. Pillon, S. Popovichev, M. Rebai, D. Rigamonti, N. Roberts, M. Tardocchi, D. Thomas and JET Contributors, "*Activation measurements in support of the 14 MeV neutron calibration of JET neutron monitors*", Fusion Engineering and Design 125 (2017) 50-56, http://dx.doi.org/10.1016/j.fusengdes.2017.10.024

IX X. Litaudon, et al., "*Overview of the JET results in support to ITER*", Nucl. Fusion 57 (2017) 102001 (41pp), https://doi.org/10.1088/1741-4326/aa5e28

X M. Nocente, M. Tardocchi, R. Barnsley, L. Bertalot, B. Brichard, G. Croci, G. Brolatti, L. Di Pace, A. Fernandes, L. Giacomelli, I. Lengar, M. Moszynski, V. Krasilnikov, A. Muraro, R.C. Pereira, E. Perelli Cippo, D. Rigamonti, M. Rebai, J. Rzadkiewicz, M. Salewski, P. Santosh, J. Sousa, I. Zychor and G. Gorini, "*Conceptual design of the radial gamma ray spectrometers system for a particle and runaway electron measurements at ITER*", Nuclear Fusion 57 (2017) 076016

XI G. Boltruczyk, A. Broslawski, M. Gosk, S. Korolczuk, R. Kwiatkowski, M. Linczuk, A. Urban, J. Bielecki, R. Costa Pereira, A. Fernandes, J. Figueiredo, V. Kiptily, A. Murari, M. Nocente, V. Perseo, D. Rigamonti, B. Santos, M. Tardocchi, I. Zychor and JET contributors, "*Development of MPPC-based detectors for high count rate DT campaigns at JET*", Fusion Eng. Des. (2017), http://dx.doi.org/10.1016/ j.fusengdes.2017.03.040

XII M. Rebai, L. Giacomelli, A. Milocco, M. Nocente, D. Rigamonti, M. Tardocchi, F. Camera, C. Cazzaniga, Z. J. Chen, T. F. Du, T. S. Fan, A. Giaz, Z. M. Hu, T. Marchi, X. Y. Peng, G. Gorini and JET Contributors, "*Response function of single crystal synthetic diamond detectors to 1-4 MeV neutrons for spectroscopy of D plasmas*", Rev. Sci. Instrum., 87 11D823 (2016); doi: 10.1063/1.4960490

XIII A. Muraro, L. Giacomelli, M. Nocente, M. Rebai, D. Rigamonti, F. Belli, P. Calvani, J. Figueiredo, M. Girolami, G. Gorini, G. Grosso, A. Murari, S. Popovichev, D. M. Trucchi, M. Tardocchi and JET Contributors, "*First neutron spectroscopy measurements with a pixelated diamond detector at JET*", Rev. Sci. Instrum., 87, 11D833 (2016); https://doi.org/10.1063/1.4961557

XIV C. Cazzaniga, A. Cremona, M. Nocente, M. Rebai, D. Rigamonti, M. Tardocchi, G. Croci, G. Ericsson, A. Fazzi, A. Hjalmarsson, M. Mazzocco, E. Strano, G. Gorini, "*Light response of YAP:Ce and LaBr3:Ce scintillators to 4-30 MeV protons for applications to Telescope Proton Recoil neutron spectrometers*", Nucl. Instrum. Methods Phys. Res. Sect. A 820(2016), 85-88. http://dx.doi.org/10.1016/j.nima.2016.03.026

XV I. Zychor, G. Boltruczyk, A. Burakowska, T. Craciunescu, A. Fernandes, J. Figueiredo, L. Giacomelli, G. Gorini, M. Gierlik, M. Gosk, M. Grodzicka, J. Iwanowska-Hanke, G. Kaveney, V. Kiptily, S. Korolczuk, R. Kwiatkowski, S. Mianowski, M. Moszynsk, A. Murari, M. Nocente, R. C. Pereira, V. Perseo, D. Rigamonti, J. Rzadkiewicz, P. Sibczynski, B. Santos, S. Soare, A. Syntfeld-Kazuch, L. Swiderski, M. Szawlowski, T. Szczesniak, J. Szewinski, A. Szydlowsk, M. Tardocchi, A. Urban,V. L. Zoita and JET contributors, "*High performance detectors for upgraded gamma ray diagnostics for JET DT campaigns*", Physica Scripta 91(2016) 064003 DOI: 10.1088/0031- 8949/91/6/064003

XVI M. Girolami, A. Bellucci, P. Calvani, C. Cazzaniga, M. Rebai, D. Rigamonti, M. Tardocchi, M. Pillon and Daniele M. Trucchi, "*Mosaic diamond detectors for fast neutrons and large ionizing radiation fields*", Phys. Status Solidi A, 1–7 (2015) / DOI 10.1002/pssa.201532191

XVII C. Cazzaniga, M. Nocente , M. Tardocchi, A. Fazzi, A. Hjalmarsson, D. Rigamonti, G. Ericsson and G. Gorini. "*Thin YAP:Ce and LaBr3:Ce scintillators as proton detectors of a thin-film proton recoil neutron spectrometer for fu-*

sion and spallation sources applications", Nucl. Instrum. Methods Phys. Res. Sect. A 751 (2014) 19-22

Contents

Chapter 1

Introduction

Nowadays the energy supply is one of key factors ruling the quality of life. In the most industrialized areas of the world, the demand for new energy production is steadily increasing. Despite, a tangible solution satisfying both the economic feasibility and the environmental sustainability is not yet found in the existing portfolio of options. That is where controlled thermonuclear fusion comes into the picture. Due to its many attractive features such as, safety, abundance of fuel reserves and minimal impact on the environment, fusion could play an important role in the future energy production. Furthermore, by considering the large quantity of electricity which it can be provided by fusion in an uninterrupted and reliable manner, it can become the major contributor to the world's energy supply. To make this become a reality, scientists need to overcome difficult scientific and engineering challenges connected to the fusion process in order to develop an economically competitive power plant.

1.1 Thermonuclear fusion and magnetic confinement

Nuclear fusion is the process in which two light elements goes close enough to overcome the electrostatic Coulomb barrier and merge together creating a heavier nucleus and releasing energy. A temperature higher than the one in the center of the sun is required (T $> 10^8$ K) to overcome the repulsive Coulomb force and allowing nuclear fusion on the earth. At these temperatures, matter is fully ionized becoming plasma. Suitable nuclei candidates for fusion on the earth are the hydrogen isotopes (hydrogen ^{1}H, deuterium ^{2}H or D and tritium ^{3}H or T) and the light isotope of helium ^{3}He. Relevant fusion reactions for fusion energy applications are as follows:

$$D + D \rightarrow {}^3_2He + n + 3.27\,MeV$$

$$D + D \rightarrow T + p + 4.03\, MeV$$

$$D + T \rightarrow \alpha + n + 17.6\, MeV$$

$$D +^3_2 He \rightarrow \alpha + p + 18.3\, MeV$$

where p and n denote a proton and a neutron, respectively. In order to be competitive reactions, they need to feature a high energy release (Q), a high cross section (σ) and the reactants have to be available in abundance. The D-D reaction would be the most desirable reaction in term of unlimited fuel supply but, due to its small release of energy and to a lower cross section, it is not the primary focus of current fusion research [1]. The D-^{3}He reaction instead, features the highest energy gain but there are no natural ^{3}He supplies on earth. Consequently, the best fusion reaction is the D-T reaction in which an alpha particle (indicted as α which is a ^{4}He nucleus) and a neutron are produced releasing 17.6 MeV of energy. This large amount of energy appears in form of kinetic energy and it is shared between the α particle and the n according to their mass. D-T reaction has high energy gain and high cross section but has the disadvantage that tritium is a radioactive isotope which decays with a half-time of 12.26 years. For this reason, there is no natural tritium on earth but it can be produced by breeding reactions using lithium which is an abundant metal presents in the earth's crust. The interesting reactions for the breeding process are [1]:

$$^6_3Li + n(slow) \rightarrow \alpha + T + 4.8\, MeV$$

$$^7_3Li + n(fast) \rightarrow \alpha + T + n - 2.5\, MeV$$

in which the interacting neutron is the one emitted by the fusion reaction. Thus, all these aspects make the D-T reaction the best choice for energy production and, in particular, the best mixture is 50% of deuterium and 50% of tritium. In the ideal condition, the energy required to keep the plasma hot is provided by the alpha particles which by slowing down heats the plasma. Evaluation of the reaction rate in hot D-T plasma is an important parameter and it requires the integration over the distribution functions of both species [2]. The total reaction rate per unit volume between two species with velocity v_1 and v_2 can be obtained as $R = \sigma(v')\, v' f_1(v_1) f_2(v_2)$ where $v' = v_1 - v_2$ is the relative velocity and f_1 and f_2 are the distribution functions. If the plasma is in thermal equilibrium the

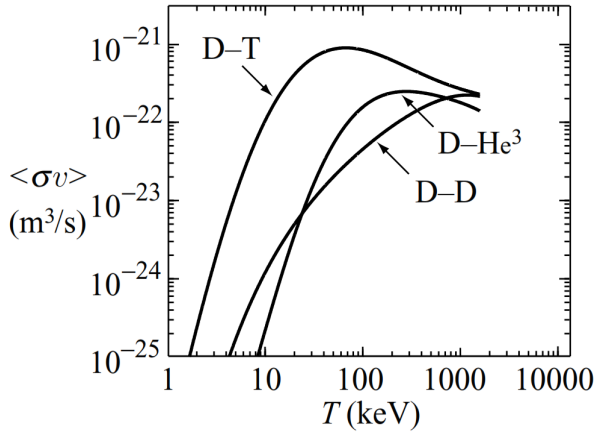

Figure 1.1: Velocity average cross section for the D-T, D-D, D-^{3}He fusion reactions as a function of temperature. Courtesy by [1].

Maxwell-Boltzmann distribution function describes the particles velocity distribution:

$$f_j\left(v_j\right) = n_j \left(\frac{m_j}{2\pi T}\right)^{3/2} \exp\left(-\frac{m_j v_j^2}{2T}\right) \tag{1.1}$$

where j denotes the specie D or T, n_j, m_j and T are the number density, the mass and the temperature. R can be written as:

$$R = \iint \sigma\left(v'\right) v' f_1\left(v_1\right) f_2\left(v_2\right) d^3v_1 d^3v_2. \tag{1.2}$$

After resolving the integral, can be more conveniently written as:

$$R = n_1 n_2 < \sigma v > \tag{1.3}$$

where $< \sigma v >$ is the average reactivity which represents the effectiveness of a fusion fuel. From the formula of the reaction rate, we can also directly infer that for a given ion density, the maximum reaction rate is obtained when $n_1 = n_2$. In particular, for D-T reaction the best mixture is 50% of deuterium and 50% of tritium. Figure 1.1 shows the graph of the reactivity $< \sigma v >$ for D-T, D-D and D-^{3}He reactions as a function of the T temperature of the reactants. The reactivity for the D-T reaction is maximum at 70 keV and drops by order of magnitudes for T$<$1 keV. Despite, the optimum operating temperature is on the order of 15 keV because the most of the fusion reactions occur on the high energy tail of the Maxwellian distribution function. At these temperatures matter is fully ionized becoming plasma. Plasma is a quasi-neutral mass of ionized gas in which electromagnetic interactions are dominant. A way to keep this hot fuel inside a chamber is by using a magnetic field according to Lorentz force. The tokamak is a toroidal plasma confinement system that has shown the better results so far. In this device, the principal

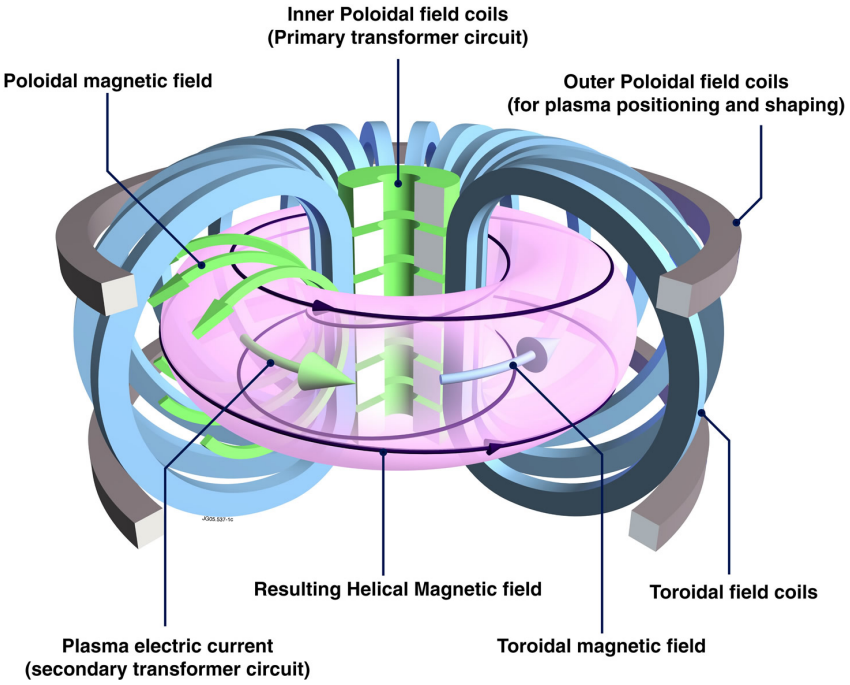

Figure 1.2: The electromagnetic coil arrangement at JET [3].

magnetic field is the toroidal field produced by external coils. Since this component is not enough to keep the particles confined, which undergo to a slow cross drift, in the tokamak a poloidal field produced by the plasma current is also applied. The combination results in magnetic field lines which have a helical trajectory around the torus as shown in figure 1.2.

1.1.1 Joint European Torus

At present, the Joint European Torus (JET) is the largest existing tokamak, located at the Culham Centre for Fusion Energy, United Kingdom. Its construction started in 1978 and it came into operation in 1983 by marking a major step for the route to a fusion reactor. The toroidal vacuum vessel has the major radius of about 3 m, minor radius of 1 m and a total plasma volume of 90 m^3. The whole device is approximately 15 m in diameter and 12 m in height. Other JET parameters can be found in table 1. JET is the only tokamak capable to operate with tritium and in 1991 it achieved the first controlled deuterium-tritium fusion reaction. Was in 1997 when JET made another step forward by achieving the world record of produced fusion power (16 MW) from 25 MW input power (Q=fusion power/input power=0.67) and demonstrating the α particle heating [4].

Plasma major radius	2.96 m
Plasma minor radius	1.25 m (horizontal) 2.10 m (vertical)
Toroidal magnetic field (on plasma axis)	3.45 T
Plasma volume	~ 90 m^3
Plasma current	3.2 MA (circular) 4.8 MA (D-shape)
Heating	38 MW
Weight of iron core	2800 tons

Table 1.1: JET parameters.

1.1.2 ITER

ITER (the Latin word for "The Way") is a large-scale international scientific experiment aiming to resolve the critical scientific and technical issues in order to prove the scientific feasibility of fusion as energy source [5]. ITER is currently under construction in Cadarache (France) and will be twice as large as JET, with a plasma volume 10 times larger and equal to about 840 m^3. ITER has been designed to produce 500 MW of fusion power achieving a gain factor ≥ 10 (Q=fusion power/input power ≥ 10) for long pulses (400-600 s).

1.2 Plasma heating

Due to energy losses, fusion plasma need to be continuously heated by external systems (see figure 1.3). In present tokamaks, the three main plasma heating systems are the follows:

1. Ohmic heating: when a current is passing through a conductive plasma, it generates dissipation heat according to Ohm's law $P_\Omega = R \cdot i^2$. Since the plasma resistance scales as $R \propto T^{-3/2}$, the ohmic heating system is suitable only for initial heating. At JET, approximately 1 MW of power is provided by ohmic heating given by plasma currents up to 4 MA [3]. This plasma current is also providing the poloidal magnetic field.

2. Neutral Beam Injection (NBI): it consists in the injection of neutral high energy atoms into the plasma, which undergo ionization and release their energy to the plasma. When a neutral atom is injected into the plasma, it travels in straight line. When the atoms become ionized through collisions with the plasma particles, the ions and the electrons are then confined by magnetic field lines. The orbit of the resulting ions depend by their energy, angle of injection and point of deposition [2]. At this point, the energetic ions gradually transfer their energy to the plasma through Coulomb collisions. The neutral beams are usually formed by hydrogen

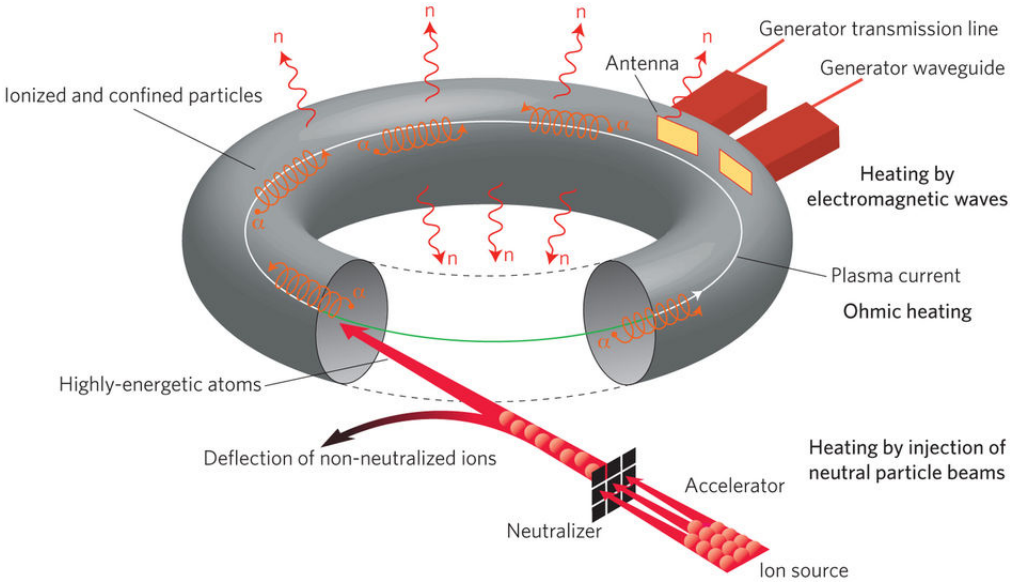

Figure 1.3: Different plasma heating systems in a tokamak [6].

ions which are accelerated by a high-voltage electric field and then neutralized via charge-exchange interactions with a gas cloud [3].

3. Radio-Frequency heating: since plasma ions and electrons rotate around the magnetic field lines, electromagnetic waves with appropriate frequency can resonate and transfer their energy to the particle species. Since the rotational frequency of the ions depends on their mass, charge and magnetic field, ($\omega = {}^{q \cdot B}/_{m}$) it is possible to target ions by injecting waves with appropriate frequency. The waves are injected by antennas placed in the vessel wall. Ion cyclotron resonant heating (ICRH) is routinely used at JET providing up to 5/10 MW of power with resonant frequencies in the range of 23-57 MHz [3].

1.3 Power balance

The high reaction cross sections, together with the high energy gain and the possibility to brewed tritium, make the deuterium-tritium reaction the best choice for energy production. The thermonuclear power per unit volume (p_{fus}) in a deuterium-tritium plasma is given by:

$$p_{fus} = n_d n_t < \sigma v > \varepsilon \tag{1.4}$$

where ε is the energy released per reaction. In particular, when considering a mixture of 50% of deuterium and 50% of tritium ($n_d = n_t$) with a total ion density equal to

$n = n_d + n_t$, the thermonuclear power density can be written as:

$$p_{fus} = \frac{1}{4} n^2 < \sigma v > \varepsilon \tag{1.5}$$

The total thermonuclear power (P_{fus}) can be derived as follows:

$$P_{fus} = \frac{1}{4} n^2 < \sigma v > \varepsilon \cdot V \tag{1.6}$$

where V is the plasma volume. Assuming the reactants at rest (with respect to the products), the high energy released per D-T reaction ($\varepsilon = 17.5\ MeV$) is distributed between the neutron and the α as following:

$$\begin{cases} \varepsilon = \frac{1}{2} m_\alpha v_\alpha^2 + \frac{1}{2} m_n v_n^2 \\ m_\alpha v_\alpha = m_n v_n \end{cases} \tag{1.7}$$

which leads to:

$$\varepsilon_n = \frac{m_\alpha}{m_n + m_\alpha} \varepsilon = \frac{4}{5} \varepsilon = 14.1\ MeV \tag{1.8}$$

$$\varepsilon_\alpha = \frac{m_n}{m_n + m_\alpha} \varepsilon = \frac{1}{5} \varepsilon = 3.5\ MeV \tag{1.9}$$

Neutrons, since they have no charge, are free to leave the tokamak and to pass through an ad-hoc designed lithium blanket which aims to convert their kinetic energy in thermal energy. α particles, instead, remain confined in the plasma and they transfer their energy to reactants keeping the plasma hot through collisions in the bulk plasma. Thus the total α particles heating is:

$$P_\alpha = \frac{1}{4} n^2 < \sigma v > \varepsilon_\alpha \cdot V = \frac{1}{5} P_{fus} \tag{1.10}$$

In the present tokamaks, to compensate the energy losses from the plasma and to keep the plasma hot, auxiliary heating systems need to be used. For net fusion power production, the useful output power P_{out} must be larger then the input power P_{in} provided by external heating systems $P_{out} > P_{in}$ [7]. Here the useful P_{out} is only a fraction of the released fusion power, due to losses in converting all the neutrons energy into electrical energy. Furthermore, radiative emissions such as visible light, x-rays and gamma-rays contribute to inevitable power losses (P_{loss}) from the tokamak. Despite, this can be compensated by the self heating (P_{self}) provided by the slowing down of the α particles into the bulk plasma. Since the average energy of plasma particles at temperature T is $\frac{3}{2} T$ and there is an equal number of electrons and ions, the plasma energy per unit volume is $3nT$. By multiplying the latter by the plasma volume, the total energy of a plasma in thermal equilibrium can be derived $W = 3nT \cdot V$. Now, the power loss can be defined

as the rate of the energy loss which is characterized by the energy confined time τ_E as follows:

$$P_{loss} = \frac{W}{\tau_E} = \frac{3nTV}{\tau_E} \tag{1.11}$$

In order to have a thermal equilibrium plasma, the power loss has to be balanced by internal (α particle heating) and external heating:

$$P_{self} + P_{in} = P_{loss} \tag{1.12}$$

When the only self heating is enough to compensate the P_{loss} and the auxiliary heating systems can be switched off, the ignition condition is reached ($P_{self} \geq P_{loss}$). Fortunately an economically sustainable commercial power reactor does not have to reach fully ignition, as long as $P_{fus} \gg P_{in}$. In any case, a key role toward the feasible thermonuclear fusion reactor is played by the α particles which have to deliver as much energy as possible to the bulk plasma.

An important parameter used to evaluate the energy balance in a reactor is the physics gain factor Q. It is defined as follows [1]:

$$Q = \frac{net\ thermal\ power\ out}{heating\ power\ in} =$$

$$= \frac{total\ thermal\ power\ out - heating\ power\ in}{heating\ power\ in} =$$

$$= \frac{P_{out} - P_{in}}{P_{in}}$$

where now P_{out} is the total thermal power output which includes all the contributions providing heating: the neutrons fusion P_n, the Bremsstrahlung radiation P_B and the plasma thermal conduction P_k (due to plasma temperature gradients that warms the reactor wall). No α heating contribution has been taken into account since their energy remains in the plasma. Consequentially, the physics gain factor Q can be written as follows:

$$Q = \frac{4P_\alpha + P_B + P_k - P_{in}}{P_{in}} \tag{1.13}$$

where $P_n = 4 \cdot P_\alpha$. Finally, from equation 1.13, in which the power losses are due to Bremsstrahlung radiation and to plasma thermal conduction ($P_{loss} = P_B + P_k$), the factor Q can be written as:

$$Q = \frac{5 \cdot P_\alpha}{P_{in}} = \frac{P_{fus}}{P_{in}} \tag{1.14}$$

From equation 1.14, it is possible to highlight that the factor is simply the ratio of the

total fusion power produced to the power input.

Chapter 2

Nuclear plasma diagnostics

In nuclear fusion experiments, the measurement and the estimation of the plasma parameters covers a fundamental role for the understanding of the plasma behavior and the optimization of the plasma performances. A burning plasma is a strong source of nuclear radiation which includes neutrons and γ-rays. Since both are not affected by magnetic fields, they escape the plasma volume and can be detected by dedicated diagnostic instruments. As mostly demonstrated at JET, Neutron Emission Spectroscopy (NES) and Gamma-Ray Spectroscopy (GRS) are among the primary techniques for studying the fast ions [8]. Specifically, neutron spectroscopy aims to diagnose the supra-thermal components of the fuel ions, whereas the measurement of γ-rays can be used to diagnose fusion alpha particles and energetic ions. Due to the harsh environment that characterize the fusion plasma devices, γ-ray and neutron spectroscopy become tough and requires dedicated diagnostic systems. Furthermore, unlike present mid-size tokamaks where the neutron and γ-rays fluxes are limited and other diagnostics can be preferred, in the next high power devices the nuclear diagnostics might be the only working fast ion diagnostics [7]. For instance, NES and GRS will benefit on ITER due to the significant increment of neutrons and γ-rays fluxes. This motivates the efforts in developing new detectors and technologies that are the topics addressed by this thesis.

2.1 Neutron diagnostics

Neutron diagnostics are one of the most important techniques for plasma diagnostics. Neutrons are directly emitted by DD (E_n= 2.5 MeV) and DT (E_n= 14.1 MeV) nuclear fusion reactions, carrying direct information on fuel ions which can be used to assess plasma information such as the fusion power, power density, ion temperature and the energy-spatial distribution of fast ions. The neutron detection is carried out by non-invasive instrumentation placed far away the plasma. For JET, the neutron measurements

can be gathered as follows:

1. Neutron flux measurements: made by fission chambers (KN1) with time resolve capability and in-vessel activation system (KN2) both able to measure the absolute neutron emission rate over a range from 10^8 n/s up to 10^{19} n/s in DT plasma. The neutron emission rate is intrinsically connected to the occurring fusion reaction rate which in turn is linked to the fusion power produced.

2. Neutron emission profile: is the measurement of the neutron emissivity over a poloidal section which provides the spatial distribution of the neutron emission source. On JET, these measurements are performed by using the neutron/gamma profile monitor consisting in 19 fan-shaped lines-of-sight (LOS). A liquid scintillator (NE213) and a plastic Bicron BC418 are placed at the end of each collimated channel. The NE213 is able to discriminate neutrons and γ-rays, instead the BC418 is used for 14 MeV neutrons. A third detector can also be inserted for γ-rays measurements. For a more detailed description of the instrument see section 2.2.

3. Neutron Emission Spectroscopy (NES): is the high resolution measurement of the neutrons energy distribution along a selected line of sight which allows measuring ion temperature T_i of the thermal plasma component and to diagnose the supra-thermal components of the fuel ions. So far, the TOFOR and the MPR spectrometers have been the reference neutron spectrometers at JET, which are optimized to measure 2.5 MeV and 14 MeV neutrons, respectively. TOFOR is based on the time-of-flight technique optimized for high rate measurements. The time of flight is measured by two detectors S1 and S2 placed on the constant time-of-flight sphere. Neutrons leave a signal in the two detectors through the elastic scattering on hydrogen. S1 gives the start signal and S2 the stop one. The relation between the neutron energy E_n and the time-of-flight $t_{TOF} = t_{S1} - t_{S2}$ is given by $E_n = {}^{2m_n r^2}/_{t^2_{TOF}}$ where m_n is the neutron mass and r is the radius of the constant TOF sphere. The MPR, namely the magnetic proton recoil spectrometer has been used at JET to provide 14 MeV neutron measurements with 5% resolution. It is based on the proton recoil technique though elastic scattering of collimated neutrons on hydrogen nuclei occurring in a thin converter foil (CH2). The resulting forward emitted protons are selected and passively separated by magnetic fields according to their energy. Finally, the position of the protons is actively measured by a scintillator array placed in the curved focal plane of the magnet (the hodoscope).

2.1.1 Neutron Emission Spectroscopy

In D and DT thermonuclear plasmas, neutrons are emitted by the two body exothermic fusion reactions $\mathrm{D} + \mathrm{D} \rightarrow {}^3_2\mathrm{He}\ (0.8\ \mathrm{MeV}) + n\ (2.5\ \mathrm{MeV})$ and $\mathrm{D} + \mathrm{T} \rightarrow \alpha\ (3.5\ \mathrm{MeV}) + n\ (14.1\ \mathrm{MeV})$, respectively. For the DT reaction case, the kinetic neutron energy is determined by the kinematic of the reaction and in the laboratory system is given by:

$$E_n = \frac{m_\alpha}{m_\alpha + m_n}(Q + K) + \frac{1}{2}m_n V_{CM}^2 + V_{CM} \cdot \cos\theta \cdot \left(\frac{2m_n m_\alpha}{m_\alpha + m_n}(Q + K)\right)^{1/2} \qquad (2.1)$$

as obtained using non-relativistic kinematics [9][8]. Here Q is the Q-value of the DT reaction (17.58 MeV), m_n and m_α are the masses of the neutron and the α-particle, respectively. K is the relative kinetic energy of the reactants (D and T) in the CM system, V_{CM} is the centre of mass velocity and θ is the angle in the CM system between the velocity of the neutron u_n and V_{CM}. K and V_{CM} are defined as

$$K = \frac{1}{2}\mu(v_{rel})^2$$

$$V_{CM} = \frac{(m_d \mathbf{v_d} + m_t \mathbf{v_t})}{m_d + m_t}$$

where $v_{rel} = |\mathbf{v_t} - \mathbf{v_d}|$ is the relative velocity of the reactants in the laboratory system and μ is their reduced mass. If the reactants are at rest ($K \rightarrow 0$ and $V_{CM} \rightarrow 0$), the neutron energy would be constant and equal to $E_0 = m_\alpha/(m_\alpha + m_n) \cdot Q = 14.0$ MeV and 2.5 MeV for DT and DD reactions, respectively. When the velocities of the reactants increase, the neutron energy is shifted by a quantity ΔE_s that depends on the reactants energy (and temperature T_i) and on the emission direction of the neutrons which is ruled by the term $V_{CM} \cdot \cos\theta$ in eq. 2.1. The latter represents the projection of V_{CM} along the direction of the neutron velocity in the CM system and is responsible for the Doppler broadening effects in the neutron emission. As the neutrons are observed along a certain line of sight (see figure 2.1), the measured neutron energy distribution represents the distribution of V_{CM} along this direction [10]. For the case of thermal plasma in which both ion populations are in equilibrium with a Maxwellian velocity distribution of ion temperature T_i, the distribution of V_{CM} is isotropic and the resulting neutron distribution is Gaussian shape with a thermal Doppler broadening proportional to the square root of the ion temperature $\sqrt{T_i}$. Furthermore, due to collective motion effects such as plasma rotation, an additional shift in the mean neutron energy can occur. The measurement of the width and the mean energy of the neutron energy distribution is a direct estimation of T_i and of the plasma rotation. When external heating is applied (NB and ICRH), the fuel ion energy distribution presents non-Maxwellian or even anisotropic components

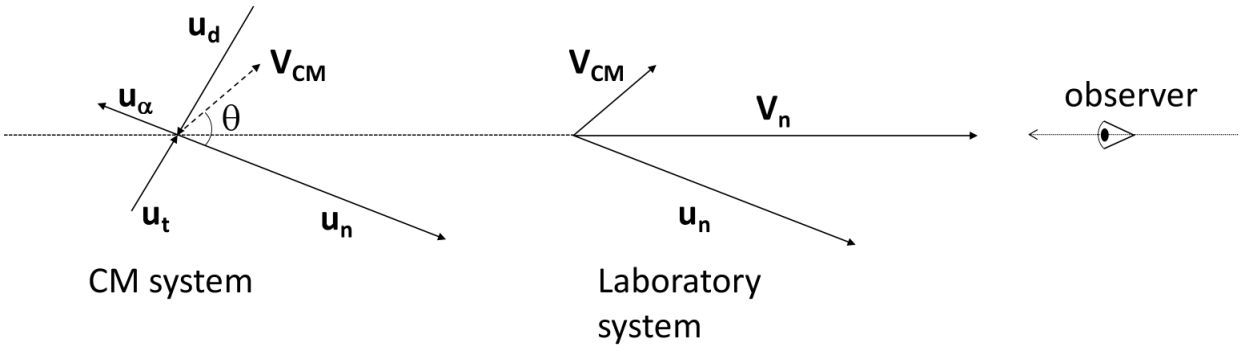

Figure 2.1: Kinematics of the reaction D(T,n)α in the CM system and in the Laboratory system.

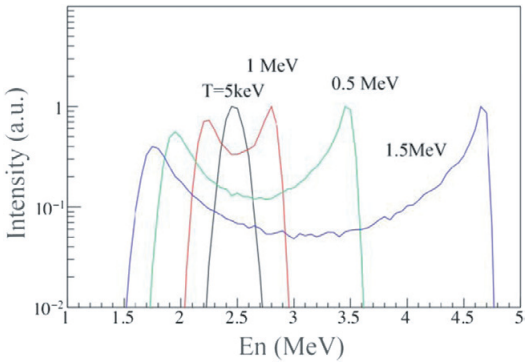

Figure 2.2: Simulated neutron spectra for three monoenergetic deuterons having a pitch angle of 90° (coloured curves) and reacting with a 5 keV thermal plasma (black curve) [8].

with respect to the magnetic field direction, producing suprathermal ions. This results in high energy components in the neutron energy spectrum which are typically of low intensity. An example representative of the ICRH heating case is shown in figure 2.2. Here the neutron spectra viewed at 90° with respect to the magnetic field are exhibited when monenergetic deuterons (energies equal to E_d = 0.1, 0.5 and 1.5 MeV) with 90° pitch angle reacts with a 5 keV D bulk plasma [8]. The resulting neutron spectra are anisotropic and much broader then the thermal one.

2.2 Gamma-ray diagnostics

The use of γ-rays detection as diagnostics tool for tokamak fusion plasmas has been evolving for decades. Historically, the spectrometry of γ-rays from nuclear reactions within the plasma had been proposed as a complementary tool to the neutron flux measurements in order to asses the rate at which the energy producing reactions occurs. Since the final goal of fusion experiments is the energy production, the measurement of these rates are an essential diagnostic. In addition, in case of aneutronic fusion reactions such as D^3He,

γ-rays detection might represents the unique available technique determining these rates [11]. Of comparable importance to nuclear reaction rates is the behavior of the fusion reaction products as well as of the other energetic plasma constituents. That is where γ-rays spectroscopy as fast ions diagnostics comes in. γ-rays emission from fusion plasmas occurs by different types of reactions: reactions between fuel nuclei (H, D, T, ^{3}He), or fast charged particles (p, d, t, α, ^{3}He) with plasma impurities (such as ^{9}Be and ^{12}C) and reactions with specially doped impurities (^{7}Li, ^{10}B and ^{11}B) [12]. There are three main sources of energetic ions at JET which are involved in the γ emission processes[12]:

- Fusion products such as fast tritons, protons, ^{3}He and ^{4}He ions in the MeV energy range:

$$D + D \rightarrow t(1.0\,\mathrm{MeV}) + p(3.0\,\mathrm{MeV})$$

$$D + D \rightarrow^3 He(0.8\,\mathrm{MeV}) + n(2.5\,\mathrm{MeV})$$

$$D + T \rightarrow^4 He(3.5\,\mathrm{MeV}) + n(14.1\,\mathrm{MeV})$$

$$D +^3 He \rightarrow^4 He(3.7\,\mathrm{MeV}) + p(14.7\,\mathrm{MeV})$$

$$T + T \rightarrow^4 He(3.5\,\mathrm{MeV}) + n + n + 11.3\,\mathrm{MeV}$$

- H, D, T, ^{4}He and ^{3}He minority ions accelerated to energies in the MeV range by ion cyclotron resonance heating (ICRH).

- High-energy ions D, T, H, ^{4}He and ^{3}He ions introduced by neutral beam injection (NBI) heating with energies up to 120 keV.

γ-rays measurements are one of the main diagnostic techniques used on JET for fast ions. They can provide information on the fast ion tail temperature and the relative densities of different energetic ions involved in the gamma emission, as well as provide the radial distribution of the fast ions. Table 2.1 shows a list of nuclear reactions identified at JET [11]. Reactions are classified by the types of fast ions interacting with different targets. The table also contains the value of the minimum energy of fast ions needed for gamma-rays observations with enough statistic at JET. The environment where these measurements are performed is a very challenging one, mainly due to the much more intense neutron flux background and the associated neutrons induced γ-rays [11]. The multitude of gamma-rays lines emitted in a given plasma volume requires dedicated spectrometers with good

Reaction	Q [MeV]	E_{min} [MeV]
Protons		
D(p,γ)^{3}He	5.5	0.05
T(p,γ)^{4}He	19.81	0.05
^{9}Be(p,p'γ)^{9}Be	-2.43	3
^{9}Be(p,γ)^{10}B	6.59	0.3
^{9}Be(p,$\alpha\gamma$)^{6}Li	2.125	2.5
^{12}C(p,p'γ)^{12}C	-4.44, -7.65	5, 8
Deuterons		
^{9}Be(d,pγ)^{10}Be	4.59	0.5
^{9}Be(d,nγ)^{10}B	4.36	0.5
^{12}C(d,pγ)^{13}C	2.72	0.9
Tritons		
D(t,γ)^{5}He	16.63	0.02
^{9}Be(t,nγ)^{11}B	9.56	0.5
^{3}He ions		
D(^{3}He,γ)^{5}Li	16.38	0.1
^{9}Be(^{3}He,nγ)^{11}C	7.56	0.9
^{9}Be(^{3}He,pγ)^{11}B	10.32	0.9
^{9}Be(^{3}He,dγ)^{10}B	1.09	0.9
^{12}C(^{3}He,pγ)^{14}N	4.78	1.3
Alphas		
^{9}Be(^{4}He,nγ)^{12}C	5.7	1.9

Table 2.1: List of nuclear reactions emitting γ-rays identified at JET [11].

energy resolution and high counting rates capability in order to resolve the peaks and to assess the occurring nuclear reactions. At JET, gamma-rays are recorded with collimated spectrometers by using semiconductor detectors (Germanium) and scintillator crystals (such as NaI, BGO, $LaBr_3$) located in well-shielded bunkers, while the spatial gamma-ray 2D emissivity measurements are performed with the JET neutron/gamma profile monitor. A description of the principal gamma-ray diagnostics used at JET is now given. Due to its superior energy resolution, a high purity germanium (HpGe) detector was installed at JET measuring the spectral broadening of characteristic γ-ray emission peaks from the reaction $^{12}C(^3He, p\gamma)^{14}N$, in $D(^3He)$ plasmas with ICRH tuned to the fundamental harmonic of ^3He [13]. However, limitations in terms of neutron resistance, high cost of large semiconductor detectors and the need to cooling systems make scintillator crystals the optimal choice for fusion gamma applications at present. For these reasons, a number of scintillators have been installed at JET. Sodium iodide (NaI) and bismute germanate (BGO) crystals have been used for years due to their high efficiency. NaI features a good energy resolution but it is not suitable for very high counting rate experiments because of one of its slow scintillation decay component (9% of total light yield). On the other hand, BGO crystals have fast decay time (300 ns) but its low light output leads to a poor energy resolution. Among new inorganic scintillator crystals which have become available, LYSO(Ce), lanthanum bromide ($LaBr_3$(Ce)) and $CeBr_3$ are the most attractive for fusion applications. Recently, JET has been equipped with two spectrometers based on LaBr3 and active Photo-Multiplier Tube, improving the existing detectors and enabling gamma ray spectroscopy at high counting rate with enhanced energy resolution in a broad energy range [14]. The JET gamma/neutron profile monitor (see figure 2.3) provides the spatial distribution of the gamma-ray emission sources. It consists of two cameras, the vertical one and horizontal one with 9 and 10 lines of sight (LOS), respectively. Each LOS is provided of three detectors addressed to neutron/x-ray/γ-rays measurement respectively. The detectors that have been used for years for the gamma-ray measurements were cesium iodide (CsI(Tl)) crystals coupled to photo-diodes. The CsI detectors can remotely be placed, together with the neutron attenuator modules, in front of the neutron detectors sharing the same line of sights. These CsI detectors feature a larger detection efficiency than the NaI, but they present limitations in term of counting rate due to the slow scintillation decay time constant ($\approx$1000 ns) as well as a poor energy resolution. For these reasons in the last years the JET Gamma Camera have been undergone upgrades with new detectors that have been custom developed.

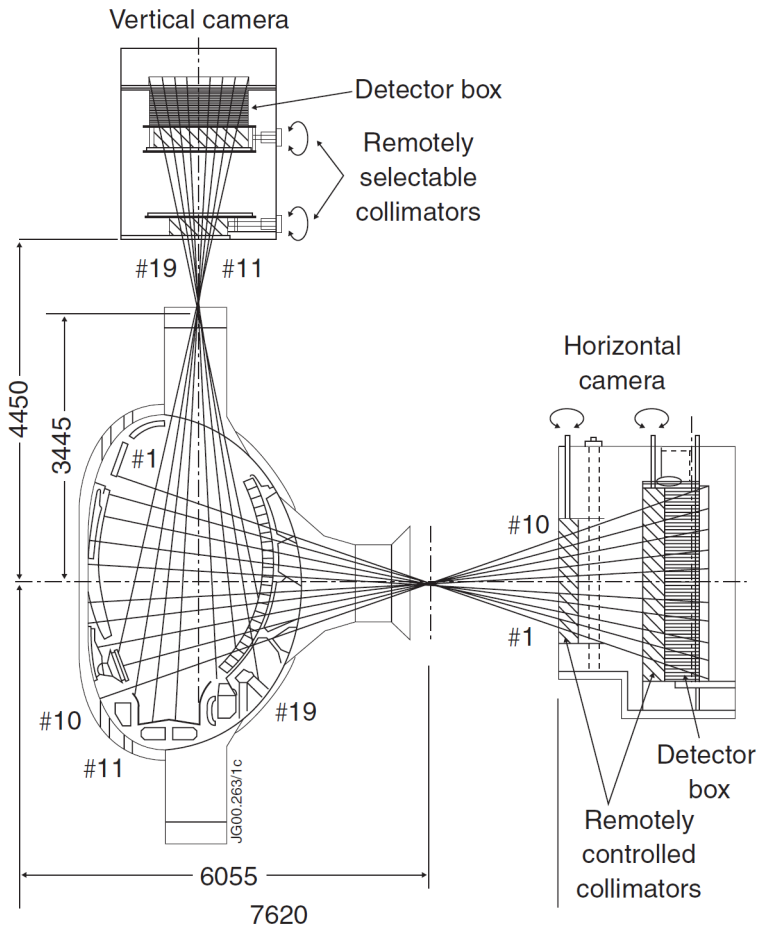

Figure 2.3: Schematic of the JET neutron/gamma emission profile monitor. Courtesy by [11]

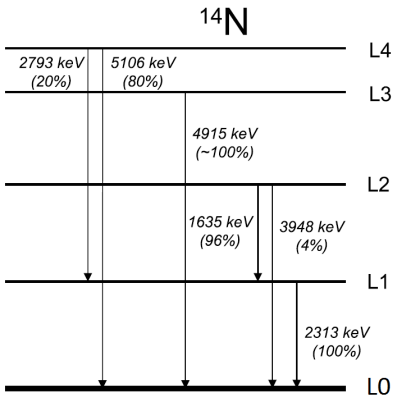

Figure 2.4: Level scheme of the first four ^{14}N excited states and their corresponding de-excitation γ-rays. Courtesy by [7].

2.2.1 Nuclear physics of fusion gamma-rays

In general γ-rays are emitted from reactions of the type A(a,bγ)B, where a indicates the light fast ion, A the impurity ion, b is the light product and B is the produced excited nucleus emitting γ-ray lines. An example of two body reaction occurring at JET is the reaction ^{12}C(^{3}He,pγ)^{14}N used for the observation of ^{3}He ions interacting with ^{12}C impurities. When the ^{14}N nucleus is produced in one of its excited states, γ-rays with different energies are emitted, depending on which excited state level is populated. Figure 2.4 shows the level scheme of the first four ^{14}N excited states and their corresponding de-excitation γ-rays.

From the kinetics point of view, the energy spectrum of the excited nucleus ^{14}N is still described by the equation 2.1. Since the ^{14}N nuclei are not produced at rest, the emitted γ-ray energy (E_γ) undergoes to a Doppler broadening. The equation relating E_γ to the ^{14}N velocity $\overrightarrow{v_{^{14}N}}$ is as follows:

$$E_\gamma = E_{\gamma 0} \cdot \left(1 + \frac{1}{c}\overrightarrow{v_{^{14}N}} \cdot \overrightarrow{u_\gamma}\right)$$

where $\overrightarrow{u_\gamma}$ is the versor indicating the gamma-ray emission direction and $E_{\gamma 0}$ is the energy when the γ-ray is emitted by a nucleus at rest, i.e. $E_{\gamma 0} = 2313$ keV for the emission from the first ^{14}N excited state. Since the product $\frac{1}{c}\overrightarrow{v_{^{14}N}} \cdot \overrightarrow{u_\gamma}$ is typically of the order of some percents, the resulting Doppler broadening for γ-ray peaks in the MeV energy range is usually of the order of few tenths of keV. In order to infer information on the reactant fast ions distribution from the measured Doppler broadening, high energy resolution spectrometers (such as HpGe or LaBr3 detectors) are required. A detailed peak shape analysis including the effects of the experimental line of observation needs to be performed. The Monte Carlo code GENESIS [7] has been developed in the past to cal-

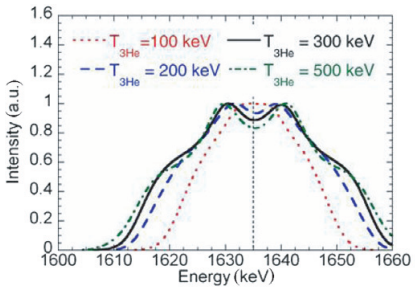

Figure 2.5: Simulated γ-ray peaks emitted by the reaction ^{12}C(^{3}He,pγ)^{14}N for fast ^{3}He distributions with different tail temperatures ($T_{^3He}$) [8].

culate the γ-ray peak shape for a selected reaction starting from a reactant distribution and the experimental line of sight. An example of simulated γ-ray peaks emitted by the reaction ^{12}C(^{3}He,pγ)^{14}N are shown in figure 2.5 for fast ^{3}He distributions with different tail temperatures ($T_{^3He}$).

2.2.2 Diagnosing of fusion alpha particles

For an economically feasible commercial thermonuclear power reactor fed with DT fuel, it is clear the importance of the α particles in keeping the DT plasma hot. The main requirement to achieve a so called burning plasma is that energy deposited by the slowing down of the α particles is high enough to compensate the energy losses described in section 1.2 - 1.3. This implies that the P_{self} has to be as close as possible to the full power released by the α particles P_α. In order to better highlight their key role, it is worth to write the fraction of total plasma heating power due only to the α particles (f_α). In this sense, we are assuming that the alpha power provides only a fraction of the total heating power and it is defined as:

$$f_\alpha = \frac{P_\alpha}{P_\alpha + P_{in}} = \frac{Q}{Q+5} \tag{2.2}$$

where P_{in} is the input power. The ignition condition is obtained when $Q = \infty$ and the external power heating can be set to 0 which implies $f_\alpha = 1$. The break-even condition in which $Q = 1$, instead, is achieved when $f_\alpha = \frac{1}{6}$. Finally, when the same fraction of power heating is delivered by the alphas and the external systems ($f_{in} = f_\alpha = \frac{1}{2}$), the burning plasma regime is reached ($Q = 5$). Since the slowing down of alpha particles occurs in the time scale of several hundred milliseconds [15], it is necessary that they remain confined sufficiently long to thermalize within the plasma. Unfortunately it is known that alpha particles, as well as any other suprathermal fast ion, drive magneto-hydrodynamic (MHD) plasma instabilities leading to their redistribution and losses, which can even be responsible for damages on the machines first wall. On a global scale, when the instabilities are not under control, it could be that $P_{self} \ll P_\alpha$ and the fusion reactions would burn

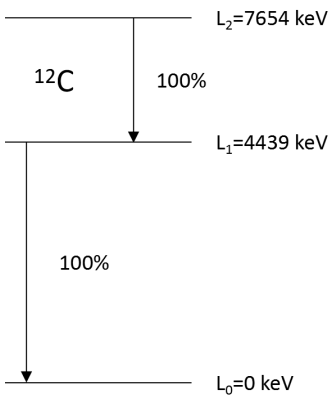

Figure 2.6: Level scheme of the ^{12}C nucleus produced in the ^{9}Be(^{4}He,nγ)^{12}C reaction.

out. On the other hand, an excessive confinement of thermalized alphas can dilute the mixture fuel preventing a steady state plasma condition. In addition, a number of new phenomena are expected in a burning plasma which so far has never been explored with today's experiments. For all these reasons, understanding the behavior of alpha particles (and the other fast ions) becomes crucial towards the goal of a reliable commercial reactor [16]. Since alpha particles are confined in the hot plasma, their diagnosis is difficult and requires special techniques, such as for instance gamma-ray spectroscopy.

The presence of beryllium impurities in the JET tokamak, due to the installation of the new beryllium ITER-like wall, offers the opportunity to exploit the reaction ^{9}Be(^{4}He,nγ)^{12}C. This reaction is the main candidate for the observation of the fusion α particles through gamma ray spectroscopy on JET in DT discharges and on ITER [17]. The reaction has positive Q-values for populating ^{12}C in the first (Q^1-value = 1.27 MeV) and second (Q^2-value = 3.4 MeV) excited state, respectively. A 4.44 MeV γ-ray (4.44 MeV $\rightarrow$0, transition) is emitted due to de-excitation of the first excited state whereas the de-excitations of the second one occurs by emission of 3.22 MeV and 4.44 MeV γ-rays in cascade (7.65 MeV $\rightarrow$4.44 MeV $\rightarrow$0, transition) (see figure 2.6). The total cross section for producing the 4.44 MeV γ-ray (see figure 2.7) is such that the process is negligible for $E_\alpha < 1$ MeV and it becomes important for $E_\alpha \geq 1.8$ MeV with resonances at $E_\alpha \approx 2.0$, 2.9, 4.3, 5.5 MeV. As shown in [17], where the considered α ions were accelerated by ICRH, the analysis of the Doppler broadened 4.44 MeV peak can provides qualitative and quantitative information on the energy distribution of α ions. Moreover, spatially resolved measurements (such as with a Gamma Camera) would provide the spatial distribution of the fusion α particles in a DT plasma and allow studying instabilities effects driven by fast ions.

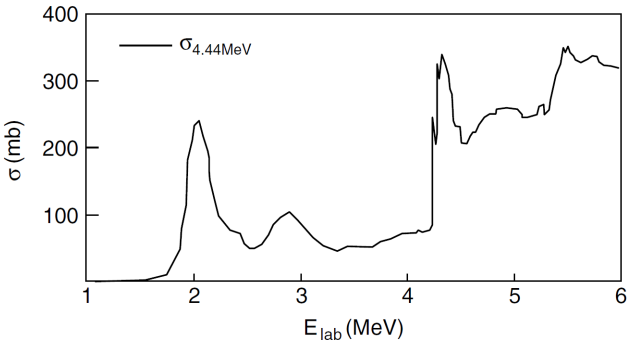

Figure 2.7: Cross section for producing 4.44 MeV γ-ray from ^{9}Be(^{4}He,nγ)^{12}C reaction. Courtesy by [17].

Chapter 3

Gamma Camera Upgrade

The first part of this thesis is related to the development and characterization of new compact gamma-ray spectrometers addressed to the upgrade of the JET gamma camera [papers I, II and III]. The enhancement is a breakthrough point enabling γ-ray spectroscopy in the forthcoming high power plasma campaigns with and without tritium. The upgrade aims to improve the spectroscopic properties of the gamma camera in terms of energy resolution and high counting rate capability. This requires significant efforts in improving the exiting CsI detectors to achieve the target values: energy resolution better than 5% at 1.1 MeV (En.Res. = FWHM / Energy) and count rate capability in excess of 500 - 1000 kCounts / s. No modification of the frame support, shielding and electronic cables is planned in the framework project. In addition, limitations in the available space makes the upgrade a challenging task. The new detectors have to fit a small cylindrical capsule of 35 mm x 35 mm (diameter x height) which prevents the use of standard PhotoMultiplier Tubes. Furthermore, the system requires the MHz counting rate capability due to the high neutron inducedγ-ray background and the insensitivity to magnetic field. Since all these requirements can not be achieved simultaneously by commercial spectrometers, a dedicated instrument has been developed in Milano. It is based on a $LaBr_3$(Ce) scintillator crystal coupled to a Silicon PhotoMultiplier (SiPM) manufactured by Saint Gobain and Hamamatsu, respectively. In this chapter the full detector and the route to achieve it, including laboratory tests and characterization measurements are presented. A comparison of different scintillator crystals is also exhibited, together with a study of the SiPM performances. The development of the detector has been mainly done at the Istituto di Fisica del Plasma "P. Caldirola" (IFP-CNR, Milano). The study of the behavior of the Silicon PhotoMultipliers was performed at the Radiation Detector Department at the National Centre for Nuclear Research (NCBJ, Swierk, Poland).

3.1 Silicon PhotoMultiplier (SiPM)

Silicon PhotoMultipliers, also referred to as Multi-Pixel Photon Cunters (MPPCs), are relative novel semiconductor devices able to convert a light signal coming from a scintillator crystal in a electronic signal. The sensor is made by a multitude of Avalanche Photo-Diode (APD) pixels connected in parallel and terminated by a quenching resistor (see figure 3.1). It operates in Geiger mode allowing a high internal gain, comparable to the one of the PhotoMultiplier Tubes (PMTs), depending on the bias voltage. The Geiger mode is on when the device is reversed biased with an operating voltage higher than the breakdown voltage (V_{bd}). This value corresponds to the minimum value needed to generate an electric field inside the depleted region of each pixel, able to accelerate the free carries enough to create secondary charge pairs in a self-sustainable avalanche mode. The avalanche, generated by a e-h pair produced by light absorption coming from the crystal, is stopped by a large resistor placed in series with the diode, called quenching resistor (R_q). When the avalanche induced current passes through the resistor, causes a drop voltage and the consequently turning off of the single pixel. The charge produced in a single avalanche is the difference between the V_{bd} and the operating voltage ($\Delta V = V_{op} - V_{bd}$), multiplied by the diode capacitance $Q = C_{diode} \cdot \Delta V$. Therefore, each APD pixel generates an identical signal when is fired by a photon. Therefore, the combined output of the SiPM is the sum of all the fired APD and its amplitude is proportional to the number of the detected photons. Finally, this number is linked to the energy of the incoming γ-ray interacting with the crystal. However, some cross-talk, dark noise and after-pulses phenomena can occur which are not directly related to the detected photons.

Silicon PhotoMultipliers offer low voltage operation (< 100 V), high internal gain (10^5 - 10^7), high photon detection efficiency, high-speed response, insensitivity to magnetic field and mechanical robustness. They feature very compact size and can be used when the space available is limited. On the other hand, they show a strong temperature dependence, a strong sensitivity to the bias voltage and a limited linearity due to a limited number of pixels. Silicon PhotoMultilpiers are usually arranged in cells/channels which can be read either individually or collectively. For the GCU spectrometer, a SiPM provided by 16 channels in parallel connected has been chosen.

The excellent photon-counting capability of the Silicon Photomultiplier and his compact size, led us to investigate more about this device in view of his implementation in the gamma camera at the Joint European Torus. In this thesis the characteristics of different SiPM arrays and scintillator detectors have been investigated and are shown in next subsections.

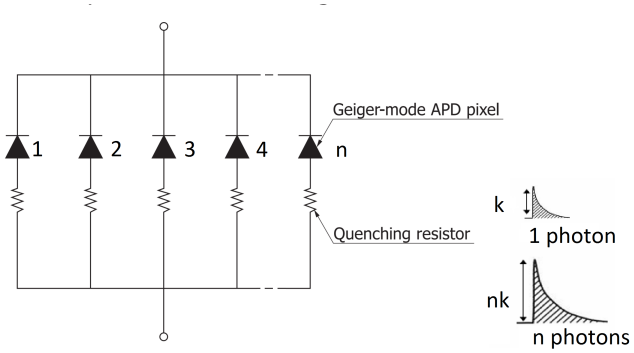

Figure 3.1: Schematic of SiPM.

SiPM properties

The Photon Detection Efficiency (PDE) is defined for a SiPM as the product of the Quantum Efficiency (QE), the Fill Factor (FF - ratio of photosensitive area to total area) and the avanlanche probability which depends on the operating voltage. The SiPM has a peak sensitivity around 400 to 500 nm. Pixel sizes affect both the non-linearity and the gain of the SiPM. Larger pixel size features a higher gain and a higher PDE. On the other hand, Silicon PhotoMultipliers with smaller pixel size are required for high-speed response applications and features a wide dinamic-range. The tipical dimension of a APD composing the Silicon PhotoMultipliers is of few tens of microns, depending by the manufacturer. Each APD has a proper internal recovery time in which it is unavailable to detect new photons. The recovery time is usually of few tens of nanoseconds depending by the APD size. Non-linearity effects are mainly due to a limited number of available pixels per area and to the pixel recovery time. For an ideal SiPM, the number of fired pixels is theoretically linear with the number of the incoming photons multiplied by the Photon Detection Efficiency as follows:

$$N_{fired} = N_{photons} \times PDE$$

For a real SiPM, instead, the response can be accurately predicted by:

$$N_{fired} = N_{pixel} \cdot \left(1 - \exp(-\frac{N_{photons} \times PDE}{N_{pixel}})\right) \quad | \quad PW < T_{recovery} \tag{3.1}$$

$$N_{fired} = \frac{N_{pixel} \times PW}{T_{recovery}} \cdot \left(1 - \exp(-\frac{N_{photons} \times PDE}{\frac{N_{pixel} \times PW}{T_{recovery}}})\right) \quad | \quad PW > T_{recovery} \tag{3.2}$$

where PW is the width of the incident light pulse, $T_{recovery}$ is the recovery time of the pixels, N_{fired} is the number of fired pixels by the incident photons and N_{pixel} is the number of SiPM's pixel [18].

Temperature changes affect the main operational parameters of the Silicon PhotoMultipliers, such as the QE, the PDE, the gain, the breakdown voltage, the dark count rate, the resistivity of R_q , the band-gap energy and the recovery time. For a given ΔV, temperature affects the width of the depletion region of the APD n-p junction, changing its intrinsics capacitance C_{diode}. The latter is linked to the characteristic recovery time which is determined by time constant $R_q C_{diode}$. When the temperature is higher, the quantum efficiency of the silicon increases due to increased phonon vibration. Those vibrations, in fact, facilitate the transition of electrons to the conduction band, resulting in a higher PDE. On the other hand, also thermal carries which are responsible for the SiPM's dark current, are facilitated to be generated. For all these reasons, in absence of temperature control, the Silicon PhotoMultiplier requires a temperature-compensation feedback circuit able to adjust the bias voltage as function of temperature to prevent gain changes. Examples of temperature changes effects are shown in next sections.

SiPM characterization

The measurements presented in this section were done with two different type of Hamamatsu Silicon PhotoMultipliers: i) a 6 x 6 mm^2 array made by 4 channels with 14400 pixels each (S10985-025C), ii) a 12x12 mm^2 SiPM arrays with 16 channels each. The first part of the measurements were done in laboratory at room temperature, whereas a climate chamber with constant and monitored temperature was used for the study of the temperature dependence. For all experiments an ORTEC Bias Supply (model 4001C) has been used. The SiPM output signal was connected to a charge sensitive preamplifier (CREMAT CR-112 or CR-113) and then amplified by a spectroscopy amplifier (ORTEC 672) which operated with different unipolar shaping time constants, depending by the applications. Finally, a multichannel analyzer TUKAN 8k [19] was used to record and analyse the spectra. An example of a basic schematic of the electronic setup is presented in figure 3.2. For the I-V characteristic curve measurement (see figure 3.3), instead, a multimeter and a picoamperometer were used to monitor the voltage and the current passing through the device. The slope change point exhibited in figure 3.3 represents the breakdown voltage of the SiPM which in this case is about 71 V.

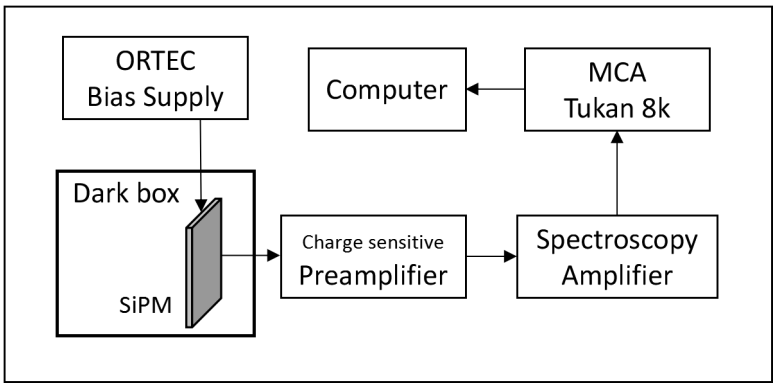

Figure 3.2: Schematic of the experimental setup.

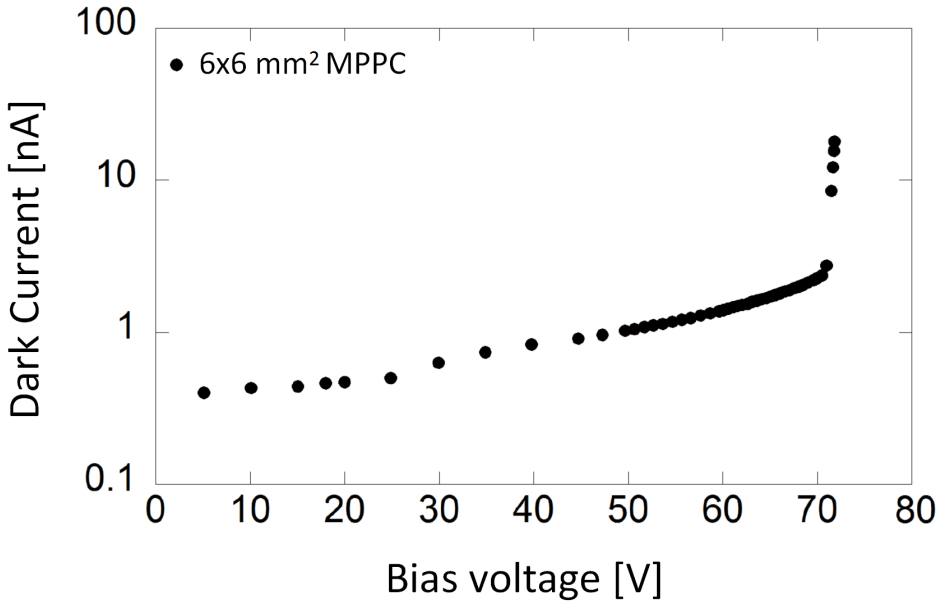

Figure 3.3: I-V curve for the 6x6 mm^2 SiPM model S10985-025C.

Breakdown voltage, gain and single photoelectron

A way to assess the value of the breakdown voltage of the SiPM is to measure the single photoelectron (phe) charge at different bias voltages by illuminating the device with low-level light pulses, as shown in figure 3.5-A. When a low photon flux arrives with a time interval longer than the recovery time of the APD, a single pixel (conventionally named photoelectron) can be fired at the time and recorded in the Pulse Height Spetrum (PHS). When a higher photon flux is applied, more then 1 pixel can be fired and the pixel output will add up resulting in a 2-photoelectron or 3-photoelectron pulses. The multi-photoelectron (multi-phe) spectrum of a 6 x 6 mm^2 SiPM is shown in figure 3.5 when illuminated by a LED type HL 6501MG of 658 nm wavelength. A Pulse generator was used to drive the LED and to send a trigger signal to the MCA. The distance in channels of two consecutive photoelectron peaks represents the charge of 1-photoelectron which strongly depends on the bias supply. A scan in voltage has been accomplished evaluating the single-photoelectron amplitude and the results are shown in figure 3.4. The breakdown voltage is the value assumed when the linear fitting curve crosses the x-axis, so when there is no gain (amplitude photoelectron = 0). In this case the V_{bd} was 70.68 V.

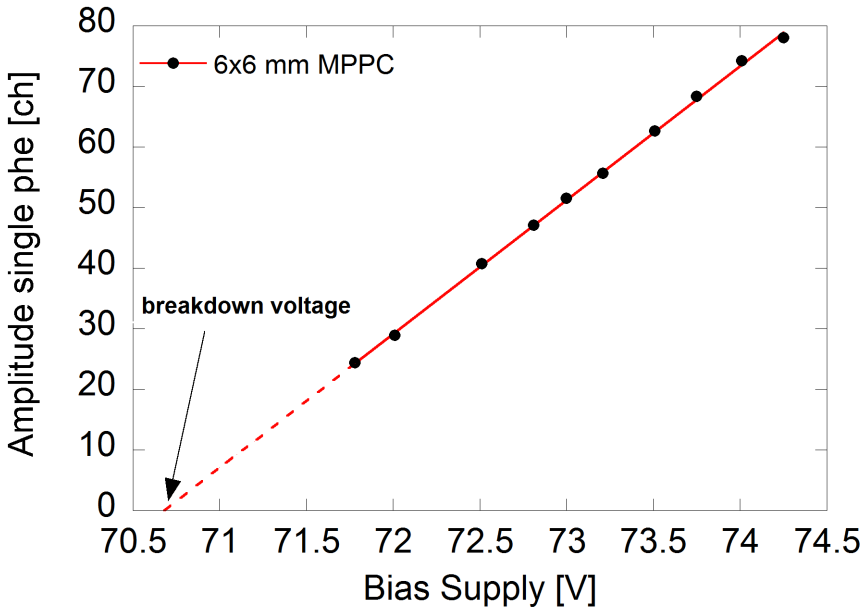

Figure 3.4: Relative gain characteristic for 6x6 mm^2 SiPM.

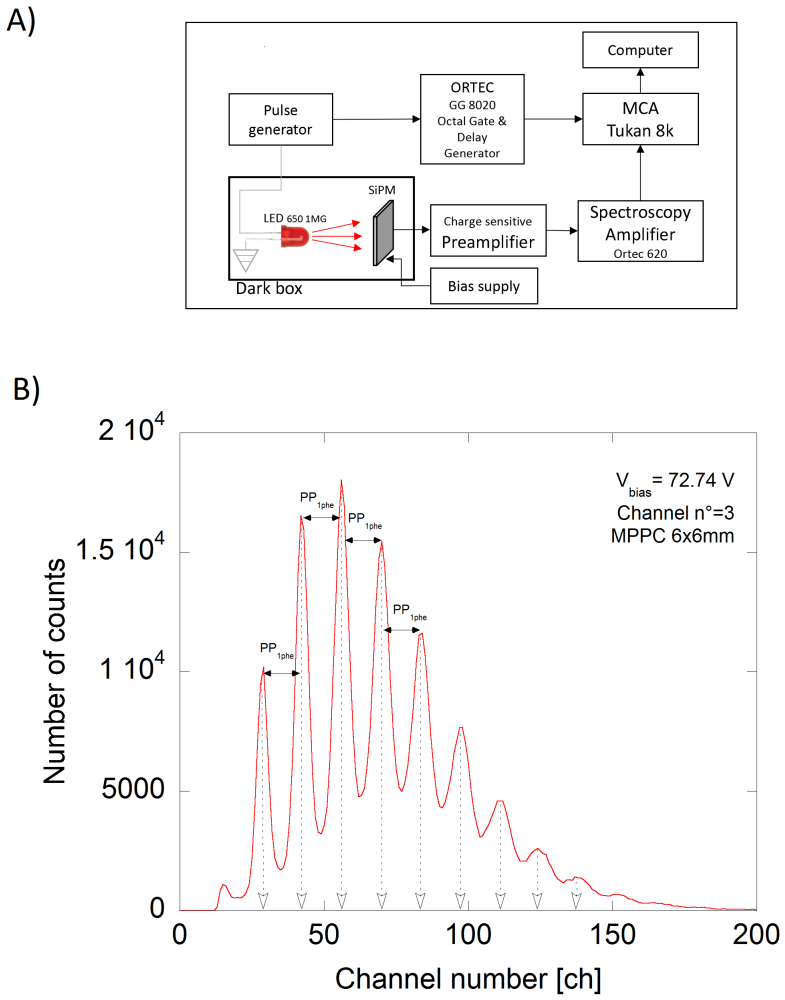

Figure 3.5: A) Schematic of the experimental setup for measuring the photoelectron spectrum. B) Multi-Photoelectron spectrum of the SiPM, achieved using low-level light pulses througth LED illumination is shown. Since the noise of a Silicon PhotoMultiplier depends by the active area of the device, at room temperature it was not possible to accomplish the experiment for the whole SiPM. Only signals coming from one 3 x 3 mm^2 channel were recorded (channel number 3).

Temperature sensitivity

Same measurements as above have been performed in a climate chamber with controlled temperatures: -20°C, -10°C, -0°C and in the temperature range 22 °C - 28 °C with 2°C step. The amplitude of the single-phe, together with the breakdown voltages, have been assessed for the explored temperatures (see figure 3.6). As expected we found that the breakdown voltage is strongly proportional to the temperature.

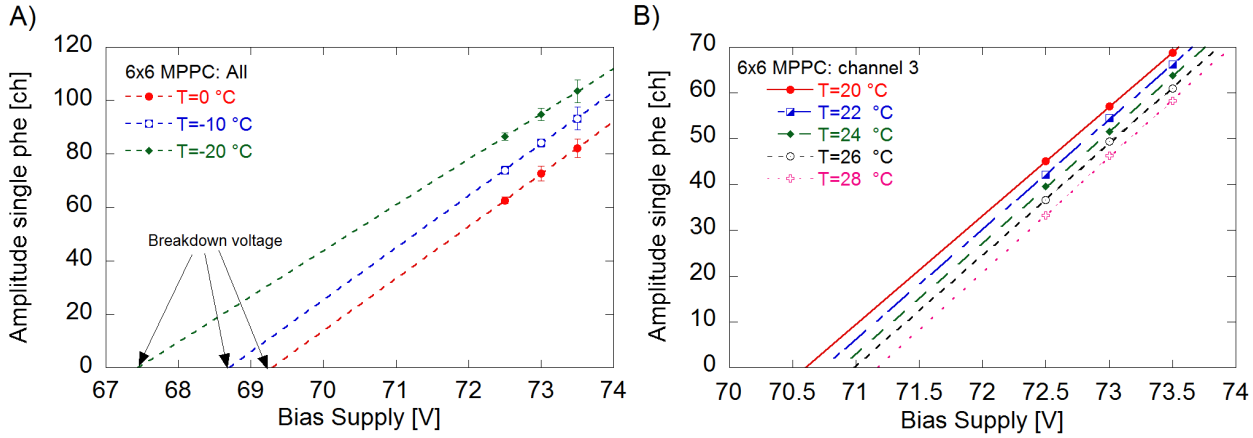

Figure 3.6: Relative gain characteristic at different temperatures. A) Signals coming from the whole SiPM were recorded. B) Only signals coming from channel 3 were recorded.

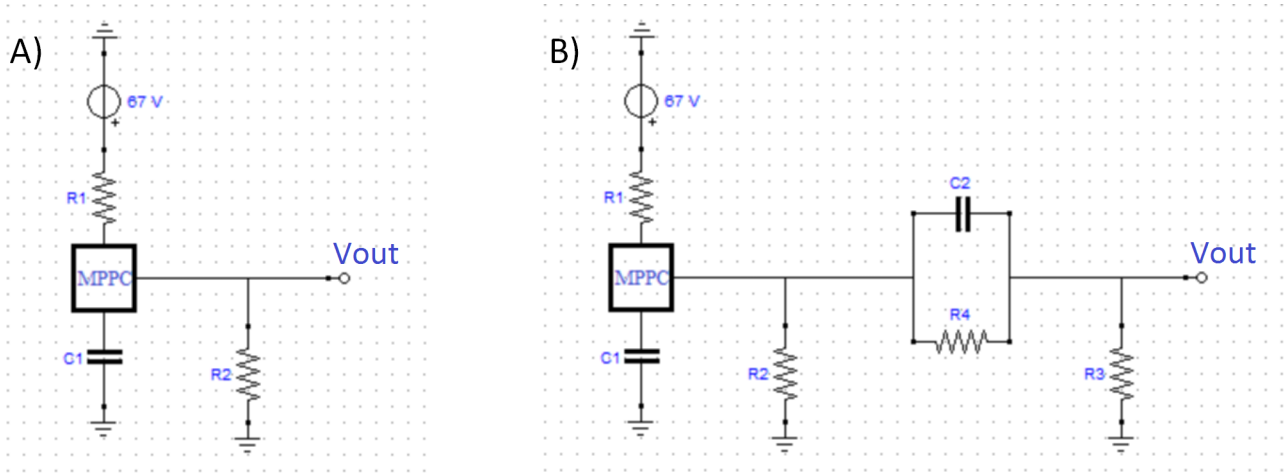

Figure 3.7: A) Sketch of the basic SIPM electronic readout circuit board. B) Sketch of the SIPM electronic readout circuit board with CR differentiator.

3.2 Development of a fast readout circuit enabling MHz counting rates with SiPMs

The selected SiPMs for the upgrade of the gamma camera, are 12 x 12 mm^2 in size, manufactured by Hamamatsu (model S13361-3050NE-04). They are composed by 16 channels connected in parallel. Each channel is made by 3584 pixels of 50 μm size with corresponding recovery time of 50 ns [20]. The standard electronic circuit board based on passive components allowing the SiPM power on and the signal reading is shown in figure 3.7-A. Resistor R1 and capacitance C1 allow stabilizing and filtering the input voltage preventing ringing effects. The shunt resistor R2, instead, converts the signal current to a voltage. Its value affects the amplitude of the generated signal as well as its temporal

length. When a too small resistance is used, the generated signal voltage across R2 is small and undershoot effects can occur. As shown in [paper I and II], a dedicated CR differentiator circuit has been implemented on the electronic readout board (see figure 3.7-B) allowing pole zero cancellation and reducing the signal length up to 120 ns. A comparison between the output signal with and without the CR differentiator is shown in figure 3.8 when the SiPM is coupled to a $LaBr_3$ crystal. The significant reduction in signal length from 300 ns (FWHM) to 55 ns (FWHM) allows minimizing the fraction of pile-up events enabling gamma-ray spectroscopy at MHz counting rate. On the other hand, a significant loss of the amplitude occurs which however does not prevent the measurements. The choice of the value of R4 and C2 was based on the analysis of the circuit transfer function which is described later. R3, instead, represents the load resistor and its value is fixed to 75 ohm.

The SiPM can be represented by an equivalent electrical model in which a current generator (I_m) is connected in parallel to an equivalent capacitance (C_m) and in series to an equivalent resistor (R_m) (see figure 3.9). R3 represents the load resistor and the value of R_m and C_m are provided by the device datasheet. The transfer function of the equivalent electrical circuit, based on the application of the Kirchhoff's laws is as follows:

$$V_{out}(s) = k \cdot \frac{I_m}{1 + s\tau_{pole1}} \tag{3.3}$$

where V_{out} is the output voltage read at R3 node, k is a constant, s is the complex variable in the Laplace domain and τ_{pole1} is the time constant of the circuit. I_m depends by the scintillation light emitted by the crystal (i.e. $LaBr_3$) and it can be written as follows:

$$I_m = \frac{I_0}{1 + s\tau_{scint}} \tag{3.4}$$

where I_0 is a constant, τ_{scint} is the characteristic scintillation time of the crystal and I_m assumes the shape of a simple decreasing exponential in the Laplace space. By combining equations 3.3 and 3.4, V_{out} can be written as:

$$V_{out}(s) = k \cdot \frac{I_0}{(1 + s\tau_{scint}) \cdot (1 + s\tau_{pole1})} \tag{3.5}$$

which, after applying the inverse Laplace transform, assumes the following form in the time domain:

$$V_{out}(t) = k' \cdot (e^{-t/\tau_{scint}} - e^{-t/\tau_{pole1}}) \tag{3.6}$$

which, as expected, it is an increasing exponential with time constant τ_{scint} followed by a decreasing exponential with time constant τ_{pole1}.

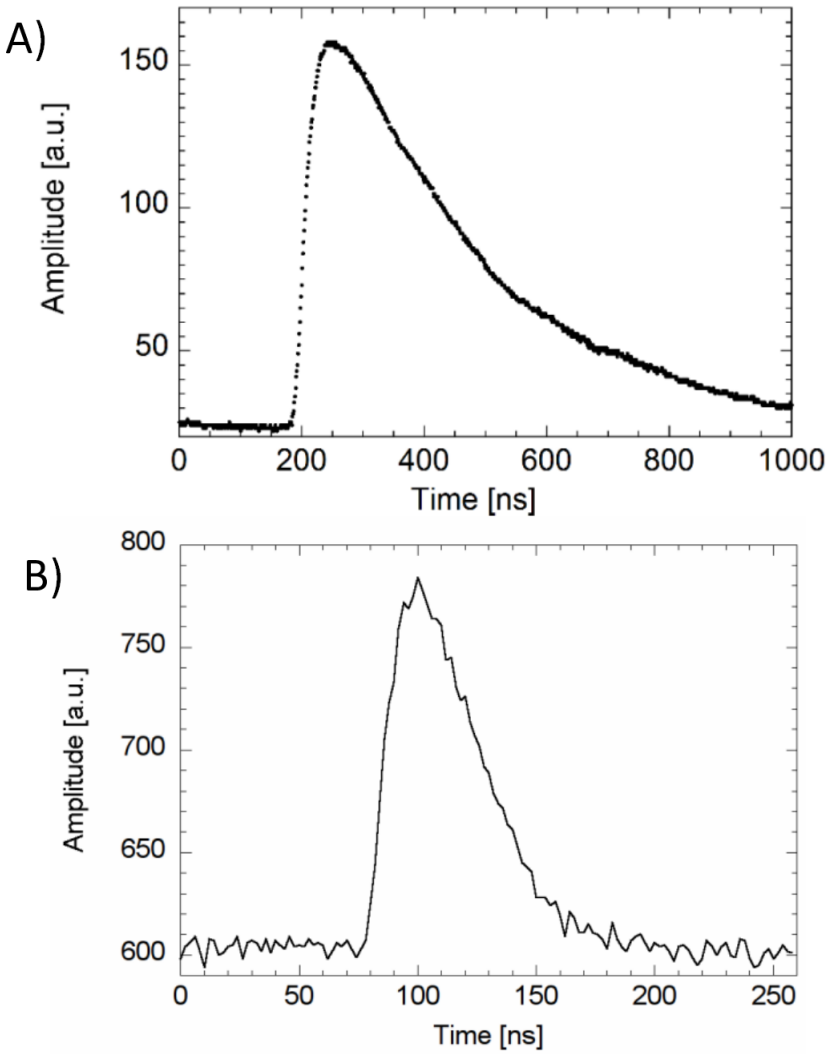

Figure 3.8: A) Original output signal coming from the SiPM without pole zero cancellation network. B) Output signal coming from the SiPM when the pole zero cancellation is applied. The signal exhibits significant reduction in the signal length [paper I].

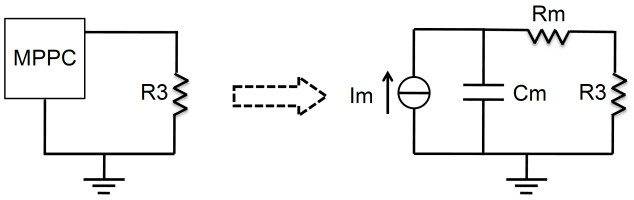

Figure 3.9: Sketch of the equivalent electrical model of a SiPM. Courtesy by [21].

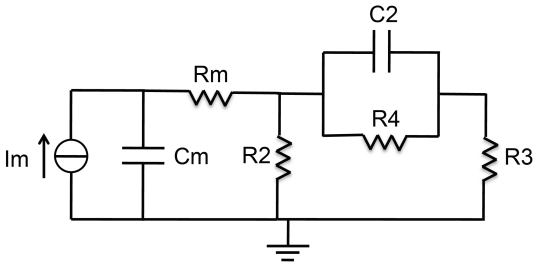

Figure 3.10: Sketch of the equivalent electrical model of a SiPM with the CR differentiator circuit. Courtesy by [21].

The equivalent electronic circuit model representing the SiPM with the CR differentiator is shown in figure 3.10. As above, the biasing circuit has not been implemented in the model because it does not affect the output signal shape. Now the transfer function assumes the form as follows:

$$V_{out}(s) = k \cdot I_m \cdot \frac{1 + s\tau_{zero}}{1 + s\tau_{pole1}} \tag{3.7}$$

where τ_{zero} represents the characteristic time constant introduced by the new components of the CR circuit. When equation 3.7 is combined with 3.4, the V_{out} becomes:

$$V_{out}(s) = k \cdot I_0 \cdot \frac{1 + s\tau_{zero}}{(1 + s\tau_{scint}) \cdot (1 + s\tau_{pole1})} \tag{3.8}$$

Once defined the decay time τ_{decay} of the output signal, the appropriate choice of R2, R4 and C2 values, verifying the condition $\begin{cases} \tau_{zero} = \tau_{scint} \\ \tau_{pole1} = \tau_{decay} \end{cases}$, allows the pole-zero cancellation removing the undertshoot in the signal. Finally, the resulting transfer function in the time domain assumes the form:

$$V_{out}(t) \propto e^{-t/\tau_{pole1}} = e^{-t/\tau_{decay}} \tag{3.9}$$

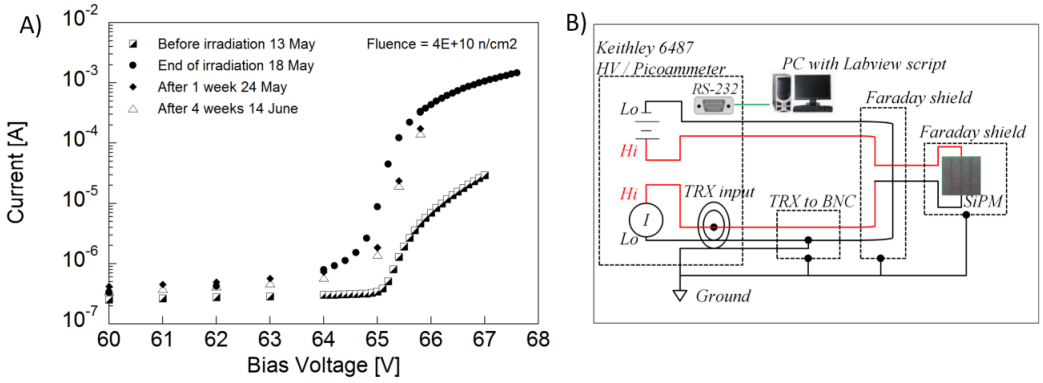

Figure 3.11: (A) Characteristic current-voltage curve before and after the neutron irradiation. (B) Schematic of the experimental setup [paper III].

3.3 Neutron resistance of the SiPM

It is well known that silicon devices can be damaged by neutrons. The high neutron/γ-ray admixed field expected in the gamma camera environment, motivated the investigation of the neutron resistance of our Silicon PhotoMultipliers and the main results are described in [paper III]. The experiment was performed at the Frascati Neutron Generator (FNG) where a Silicon PhotoMultiplier has been irradiated with high 14 MeV neutron fluxes. Neutrons were emitted by DT reactions occurred by accelerated deuterium ions impinging on a tritiated-titanium target. The neutron yield from the target was monitored as a function of time by the standard diagnostics of FNG based on an alpha counters of the α's produced by DT reactions in the target. The SiPM was placed at a distance of 18 cm from the target and irradiated at increased fluxes, up to a total fluence of $4 \cdot 10^{10}$ n/cm^2. The effects due to the neutron irradiation were monitored in term of increase dark current and degraded of the pulse height spectrum. The SiPM was connected to a Keithley picoammeter Model 6487 able to measure simultaneously in real time the dark current and the bias voltage with a high degree of accuracy. To prevent electromagnetic pick up noise, the SiPM was wrapped in an aluminum foil working as Faraday shield. A sketch of the experimental setup is shown in figure 3.11-B. As described in [paper III] and exhibited in figure 3.12-A, we find that the dark current increase as a function of the neutron fluence F and the experimental data are well fitted by the curve $f(F) = a - b \cdot \log(F + c)$, where a, b and c are free parameters. A self-recovery process was observed in which the SiPM dark current partially decreases exponentially on a time scale of few days (see figure 3.12-B). Beside the dark current, the characteristic current-voltage (I-V) curve of the device was periodically measured after the neutron irradiation and compared to the one before the irradiation (see figure 3.11-A). As expected, higher values of the current occurred which have decreased partially on a time scale of a few days in a way consistent with the behavior

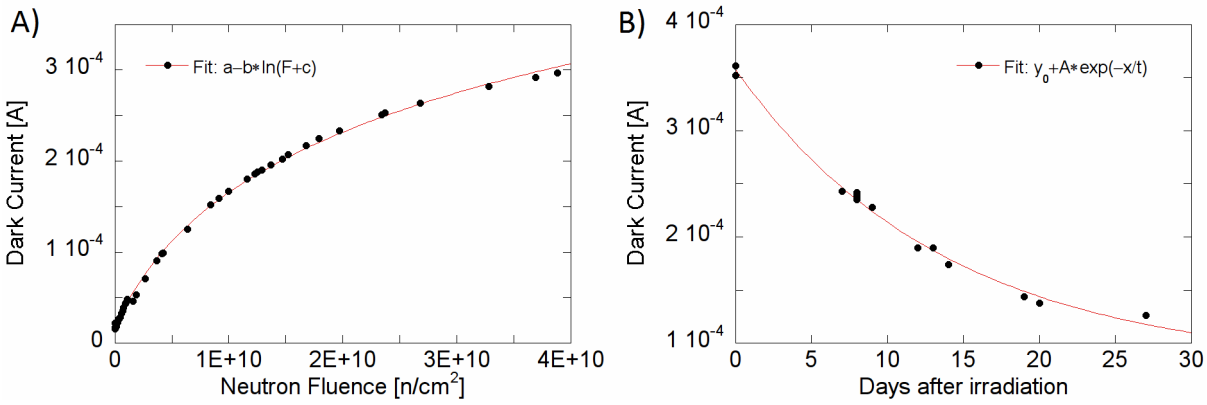

Figure 3.12: A) Measured dark current as a function of the neutron fluence at the detector. B) Measured dark current after the neutron irradiation experiment partially decreases after few days [paper III].

found for the dark current. No significant changes have been noticed for the value of the SiPM breakdown voltage up to the maximum fluence we tested, i. e. $4 \cdot 10^{10}$ n/cm^2.

In order to evaluate the neutron effects on the SiPM spectroscopic capability, a measurement of the pulse height spectrum from a ^{60}Co source has been recorded by a $LaBr_3$ crystal coupled to a SiPM which experienced a neutron irradiation of $1.5 \cdot 10^{10}$ n/cm^2. A higher background contribution in the spectrum was observed and is ascribed to the activation of the FNG experimental hall and materials near the spectrometer (see figure 3.13). The two full energy peaks at 1173 keV and 1333 keV from the cobalt source are clearly visible with an energy resolution of 5.1 % and 5.2 %, respectively, which is comparable to the values measured before irradiation.

The extrapolation of the neutron irradiation to measurements at JET is very favorable. The expected neutron fluxes for a full power JET DT plasma are about 10^7 n/cm^2/s and 10^8 n/cm^2/s in the central channel of the vertical and horizontal camera, respectively. This corresponds to a total neutron yield of 2×10^{18} n/s which have been achieved for less than 1 s at JET during the record discharge in 1997. The maximum neutron fluence experienced at FNG corresponds to about 4000 s and 400 s of a full power DT plasma for the vertical and horizontal camera, respectively. These results indicate that the possible neutron damage does not concern our application and, therefore, a gamma-ray spectrometer based on a SiPM can be used in the JET gamma camera.

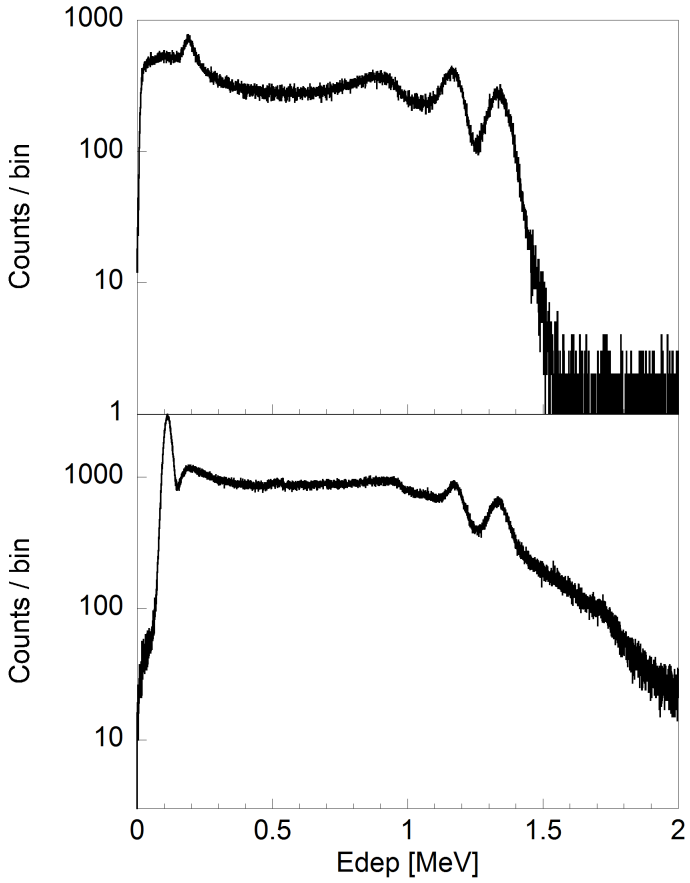

Figure 3.13: Pulse height spectrum recorded before (top) and after (bottom) a neutron irradiation of 1.5×10^{10} n/cm^2 [paper III].

Crystal	Density [gr/cm^3]	Z_{eff}	Decay time [ns]	Brightness [photons/MeV]	λemission [nm]
$LaBr_3$	5.07	45.3	26	63000	380
$CeBr_3$	5.18	45.9	20	68000	390
LYSO	7.1	66	45 / 35	30000 / 35000	420
YAP	5.55	32 / 36	27	18000	350
CsI	4.51	54	1000	54000	550

Table 3.1: Summary of crystals properties.

3.4 Scintillator crystals and $LaBr_3$ response to γ-rays and 14 MeV neutrons

In order to choose the suitable detector for the gamma camera, the evaluation on different scintillator crystals has been done. The very limited space (diameter 35 mm x height 35 mm) at the detectors position and the unavailability of nitrogen cooling system prevent the use of high resolution HpGe detectors and make scintillator crystals the only choice. At present, the use of fast, high light yield inorganic scintillators i. e. $LaBr_3$, $CeBr_3$, LYSO and YAP would in principle allow significant improvements in terms of energy resolution and/or counting rate compared to the existing CsI crystals (see table 3.1). Their performances have been compared and studied in laboratory when coupled to a Silicon PhotoMultiplier. Measurements have been carried out with ^{137}Cs and ^{60}Co radioactive sources in same operational conditions. $LaBr_3$ crystal features the best energy resolution due to its high light yield (i.e. 63000 photons/MeV) but it is hygroscopic and needs to be encapsulated. CeBr3 has comparable high effective atomic number Z ($Z_{eff} \approx 45.9$) and density but was found to have a slightly worse energy resolution. Furthermore it is hygroscopic that implicates difficulties in growing crystal production for both $LaBr_3$ and $CeBr_3$ scintillators. The LYSO is very promising one in term of high density and high detection efficiency. In contrast, however has lower light yield and thus worse energy resolution. All the three scintillators suffer of intrinsic radioactivity which would not affect the measurements due to the small size of the crystal. The main contribution to the activity of the $CeBr_3$ is due to the presence of impurities, such as the ^{227}Ac which decays producing a broad structure in the spectrum. The $LaBr_3$ crystals, instead, in addition to the structure induced by the ^{227}Ac, feature a visible Gaussian peak at 1435.8 keV due to the decay of the ^{138}La isotope which can be exploited for a rough energy calibration. Thanks to its good energy resolution, which is in between the one of the $LaBr_3$ and of the LYSO, the YAP crystal has a wide range of applications. It features mechanically robust characteristics and can be easily machined into various shapes and geometries. Despite, it has a lower detection efficiency.

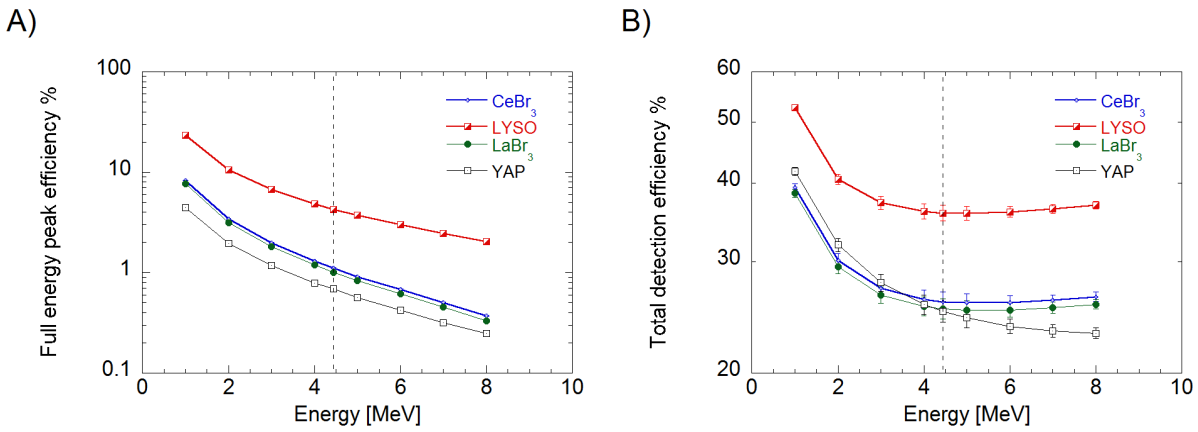

Figure 3.14: A) Calculated detection efficiency of different scintillator crystals as a function of the incoming gamma-ray energy. A) Full energy peak efficiency. B) Total detection efficiency.

In order to evaluate the gamma-rays detection efficiency of the crystals, Monte Carlo simulations have been run by using MCNP code [22]. A mono-directional and monochromatic gamma-ray disk source impinging the flat surface of the crystals was simulated and repeated with different energies from 1 MeV to 8 MeV. Concerning the scintillator crystals dimensions, the maximum size allowed to fit in the capsule was used in the simulations (which is 16.9 mm height and 25.4 mm of diamater). The total detection efficiency and the full energy peak efficiency calculated for the four crystals are shown in figure 3.14. $LaBr_3$ crystal is preferred to the LYSO for its enhanced energy resolution which allows to better resolve the gamma-ray peaks in the measured spectrum and, consequently, to better infer plasma information. However, the LYSO features a higher detection efficiency which, in the other hand, imposes enormous efforts to cope the extremely high counting rate expected in the JET GC.

For these reason the detector chosen for the GCU is a $LaBr_3$ crystal coupled to the SiPM since it features the best performances combining the fast response with the best energy resolution and an acceptable detection efficiency. From calculations reported in [23], we could expect for a $LaBr_3$ crystal in the central channel of the two cameras a counting rate between 0.9 and 3.5 kHz in the 4.44 MeV full energy peak. In order to evaluate the expected spectrum measured by the detector, a MCNP calculation of the response function of a $LaBr_3$ crystal to 4.44 MeV γ-rays was performed (see figure 3.15). Despite the small crystal size, the full energy peak is clearly visible as with the single escape and double escape peaks.

From a diagnostic point of view, the expected counting rate for the $LaBr_3$ crystal is acceptable for the application but the breakthrough point is its enhanced energy resolution.

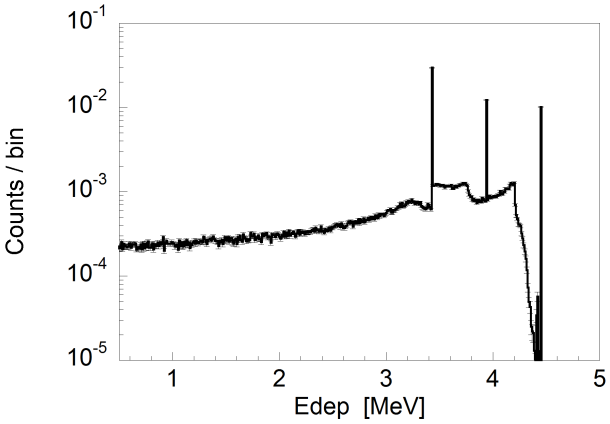

Figure 3.15: Calculated response function of a 16.9 mm x 25.4 mm LaBr3 crystal to 4.44 MeV gamma-rays from the ^{9}Be(α, n)^{12}C reaction.

This would allow avoiding possible artifacts in the reconstructed fast ion profile.

As shown in [paper III], the response of the $LaBr_3$ crystal to 14 MeV neutrons has been studied at FNG. For this purpose, the 25.4mm $\times$ 16.9mm (diameter height) $LaBr_3$ has been coupled to a standard Hamamatsu PhotoMultiplier Tube and irradiated with 14 MeV neutrons at FNG. More details on the neutron production and FNG are given in section 3.3. The crystal was placed at the distance of 33 cm from the target and at an angle of zero degrees with respect to the beam. The corresponding neutron flux at the detector position was $3.5 \cdot 10^4$ n/cm^2/s resulting in a counting rate of 57 kCounts/s. Since the detector output signal is 80 ns long at full width at half maximum (FWHM), the estimated pile-up probability occurring at this counting rate is less than 1 % and the distortion structures of the pulse height spectrum due to unresolved pile-up events are negligible. The output signal was fed into a CAEN DT5730 digitizer (500 Msps - 14 bit) [24] able to perform online data analysis and/or to store each single waveform for a later processing. Before starting the neutron irradiation, the detector was calibrated with ^{137}Cs and ^{60}Co radioactive sources. Figure 3.16 shows the recorded pulse height spectra after 1200 seconds integration time both in linear and logarithmic scale. The spectra features few characteristic peaks and an exponential decay. The most of the events occurs in the low energy region. Less than 4% of the events occurs in the energy region above 3 MeV which is the region of interest for gamma-ray plasma diagnostics. We found that inelastic neutron scattering is one of the most important interaction at low energies. Instead, at higher energies, the main contribution is due to secondary particles (protons, deuterons, alphas, neutrons) produced by nuclear reactions in the crystal materials. The measured pulse height spectra have been successfully interpreted by MCNP simulations (see figure 3.17) which also allowed calculating the neutron detection efficiency of the crystal (about % 8). First the energy spectra of the direct neutrons, scattered neutrons and background

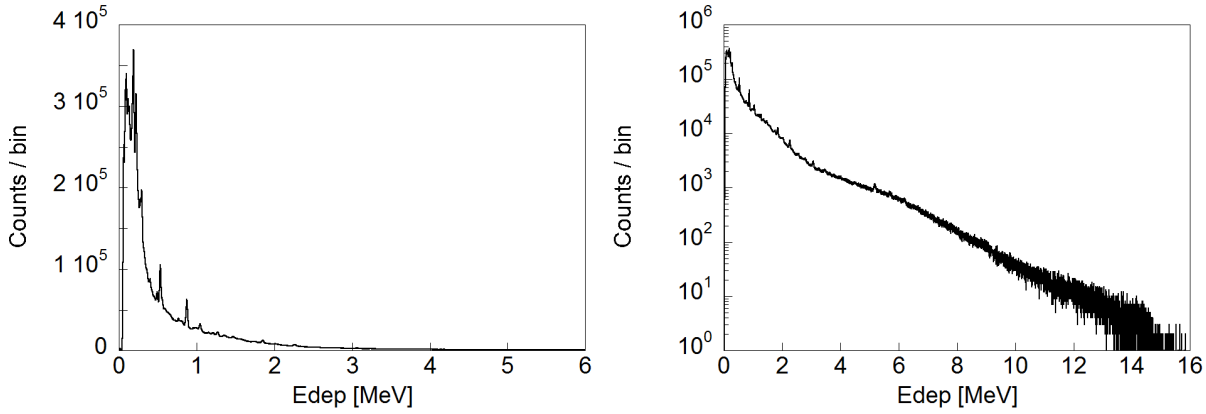

Figure 3.16: Energy spectra both in linear (left) and logarithmic (right) scale measured at FNG with a LaBr3 crystal in 14 MeV neutron irradiation experiments [paper III].

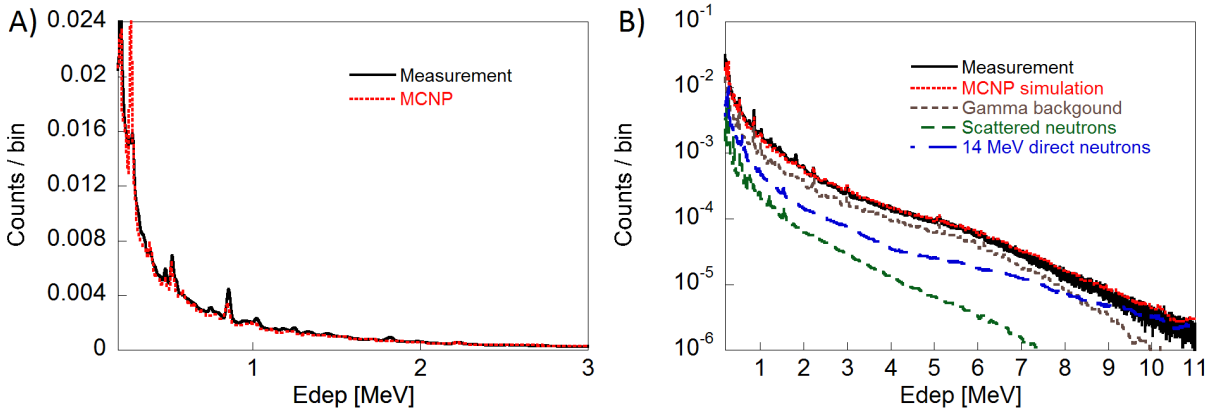

Figure 3.17: Comparison between the measurement (normalized) and the MCNP simulation both in linear (A) and in logarithmic (B) scale. In the figure on the right, the contributions due to the 14 MeV direct neutrons the scattered neutrons and the gamma background are individually shown [paper III].

gamma-rays impinging the detector have been calculated by using a MCNP model of FNG, then their contribution inside the crystal has been obtained with dedicated MCNP scripts. By fitting the spectral shape of these three components to the data of figure 3.17, we find that the 50% of the recorded events is due to direct 14 MeV neutrons (efficiency detection of about 8.2%), 31% is due to environmental γ and 19% are scattered neutrons.

The extrapolation of these results to JET measurements is favorable. The effects of 14 MeV neutron irradiation on the $LaBr_3$ crystal does not prevent gamma-ray spectroscopy measurements. The neutron contribution in the region of interest for gamma-ray diagnostic is suppressed by a factor about 300 compared to deposited energy values below 1 MeV. Furthermore no evidence of neutron damage have been experienced with a neutron fluence up to $3 \cdot 10^9$ n/s.

3.5 The new compact gamma-ray spectrometer for the gamma camera upgrade

A dedicated compact gamma-ray spectrometer has been developed in Milan improving the spectroscopic capabilities of the JET gamma camera. Silicon PhotoMultipliers have demonstrated resistance to high neutron fluxes [paper III] and can be a feasible solution for the JET gamma camera. The selected $LaBr_3$ crystal features an acceptable detection efficiency for 4.44 MeV gamma-rays and an enhanced energy resolution [paper I] which allows avoiding possible artifacts in the reconstructed fast ion profile. On the other hand, it is not insensible to neutrons (detection efficiency $\approx$ 8 % @ 14 MeV neutrons) but the neutron contribution in the energy region interesting for γ-ray diagnostics does not prevent the measurements [paper III].

The full detector (see figure 3.18) has been tested and characterized with low activity radiation sources and with high γ-ray fluxes, as described in [paper I and II]. A study of the behavior at high counting rate has been also assessed with LED pulses and its extrapolation to JET measurements is given.

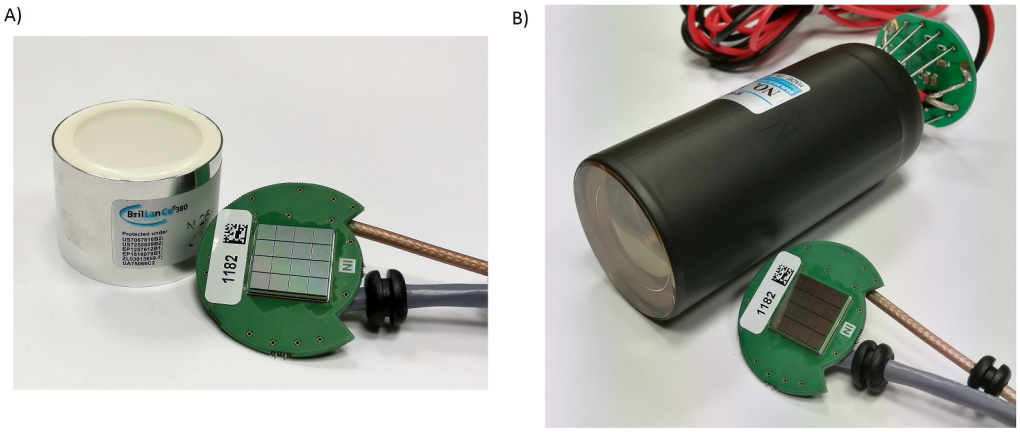

Figure 3.18: A) Picture of the selected LaBr3 crystal and the SiPM mounted on the fast readout circuit. B) Comparison between the SiPM including its electronic circuit and a standard PMT.

3.6 Detector characterization

In order to characterize the detector response in terms of energy resolution and linearity, laboratory measurements have been performed in Milan (Italy) and at the National Centre for Nuclear Research (Poland). The SiPM was powered by a TTi EX752M voltage supply and the detector was placed in a light-proof box. Both the bias voltage and the current passing through the circuit were monitored by two multimeters. Signal from the detector

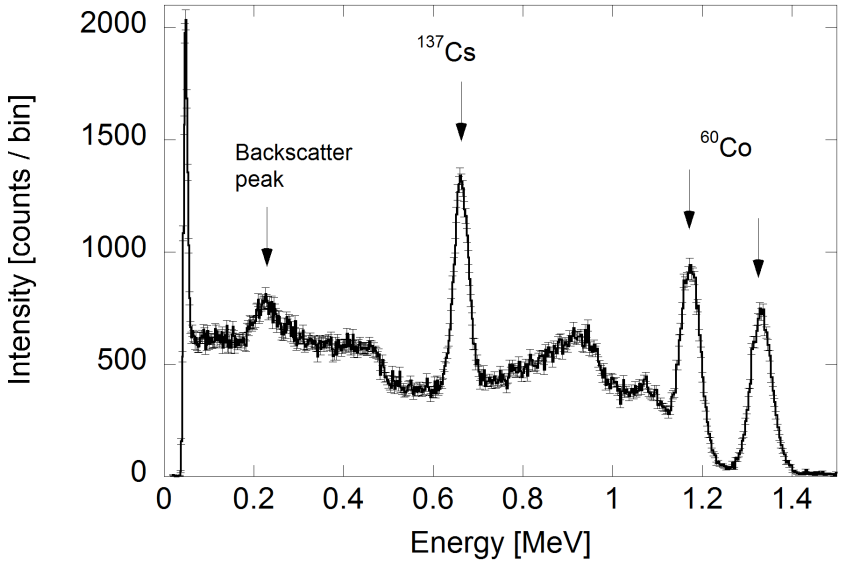

Figure 3.19: Pulse height spectrum recorded by the GCU spectrometer with ^{137}Cs and ^{60}Co radioactive sources [paper I].

was fed into a CAEN DT5730 digitizer (500 Msps - 14 bit) [24] able to perform online data analysis by integrating each pulse area. An example of pulse height spectrum recorded with ^{137}Cs (E_γ =0.662 MeV) and ^{60}Co (E_γ =1.173 MeV and E_γ =1.333 MeV) radioactive sources is shown in figure 3.19. A scan in voltage has been performed evaluating the optimum operational point of the Silicon PhotoMultiplier (see figure 3.20-A). The peaks of the spectra were fitted by a Gaussian function on a background described by polynomials. An energy resolution (Energy Resolution = FWHM/Energy) of about 5 % was obtained at 662 keV which improves to about 3.3 % for 1333 keV gamma rays when the optimum operational voltage is used. The trend of the energy resolution as a function of the gamma-ray energy is well fitted by the curve [25] $f(E) = \frac{(\alpha+\beta E)^{1/2}}{E}$ where α and β are two free parameters (see figure 3.20-B). This extrapolates favorable scenarios for the detection of 4.44 MeV γ-rays from the ^{9}Be(α, n)^{12}C reaction, allowing accurate measurements with an energy resolution (EnRes) better than 3 % at 4.44 MeV. At the National Centre for Nuclear Research (NCBJ, Poland) the limited linearity of the detector has been investigated by recording gamma lines from ^{137}Cs, ^{65}Zn (E_γ =1.116 MeV) and PuBe sources (see figure 3.21-A) [see paper I]. The latter, which emits a gamma-ray at 4.44 MeV, results in three peaks in the pulse height spectrum: the full energy peak, the single escape peak and the double escape peak. Measurements were performed in a climate chamber at stable temperature in order to prevent drifts due to temperature changes. When assuming the 511 keV and 662 KeV relative points to be in the linear region, we find a non-linearity of about 20 % at 4.44 MeV (see figure 3.21-B) which can be corrected off-line. When we

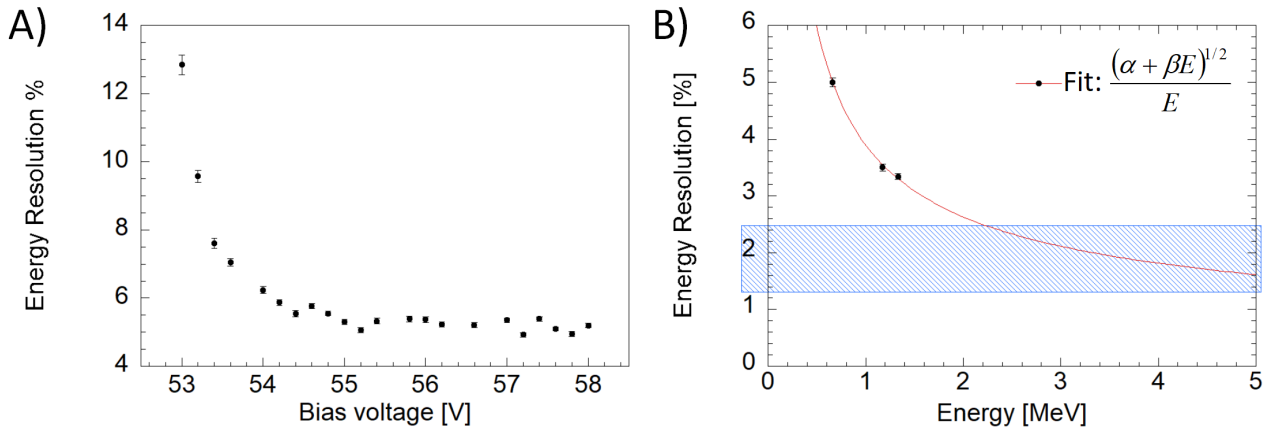

Figure 3.20: A) Measured energy resolution asa function of the bias voltage. B) Measured energy resolution as a function of the energy [paper I]. Error bars are of the same magnitude of the black dots. The dashed region indicates the expected energy resolution in the region of interest for plasma diagnostics with gamma-ray spectroscopy.

include the zero point in the linear fit, instead, a nonlinearity of about 28% at 4.44 MeV occurs.

3.7 High counting rate measurements

At JET, the main contribution to the γ-ray background in the gamma camera is due to neutrons interacting with the shielding. Neutrons undergo multiple scattering and when they are capture in the shielding a gamma-ray is emitted. The corresponding γ-ray background fluxes are expected to be tremendously high at the detectors positions producing in the detectors counting rates in the MHz range for DT plasmas. These predictions have been provided by MCNP simulations [26] for both DD and DT scenario and confirmed by benchmark background measurements in JET DD plasmas. The simulations in [26] providing the expected energy spectra for γ-ray background for both DD and DT plasmas (see figure 3.22 A - B) have been used as input for calculating the expected deposited energy in the crystal (see figure 3.23) and its detection efficiency. Since gamma-ray background is produced by neutron capture occurring in the shielding, gamma-rays have no preferential directions. For this reason, the simulated geometry consists by the crystal inside a hollow spherical isotropic source in which the γ-rays impinge the detector from every directions. It was found that about the 46 % of the incoming γ-ray background provides an event in the spectrum which energy distribution is shown in figure 3.23. The estimated equivalent energy deposited ($< E_\gamma >$) in the spectrum corresponds to about 550 keV. The latter is an important parameter to takes into account in high rate experi-

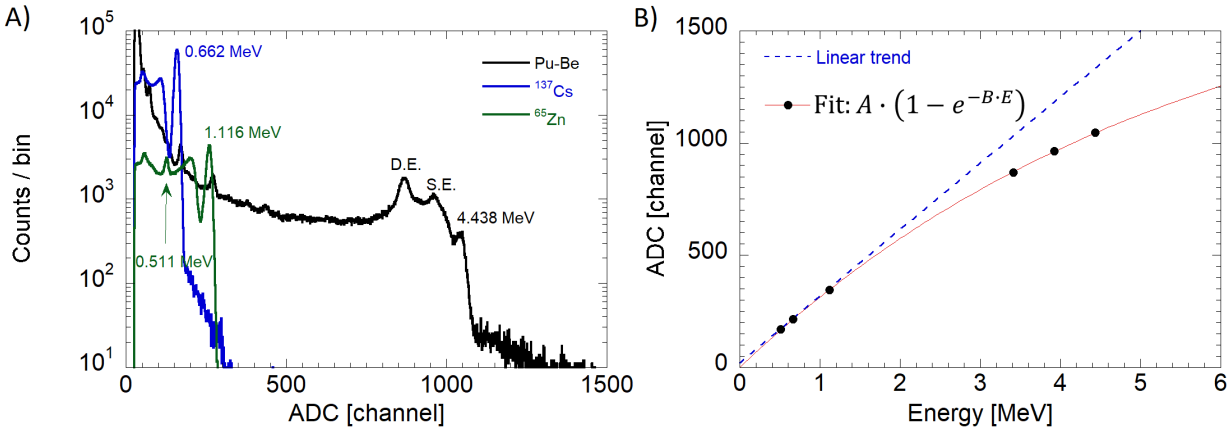

Figure 3.21: A) Pulse height spectra recorded with ^{137}Cs, ^{65}Zn and Pu-Be souces. B) SiPM non-linearity. Linear trend has been extrapolated by fitting first two points corresponding to energies 0.511 MeV and 0.662 MeV, respectively. Error bars are of the same magnitude of the black dots [paper I].

ments since it affects the average current flowing in the SiPM. The behavior of the GCU spectrometer has been studied in Legnaro with high gamma-ray fluxes and in laboratory with LED pulses. Results are described in [paper I and II] and presented in following sections.

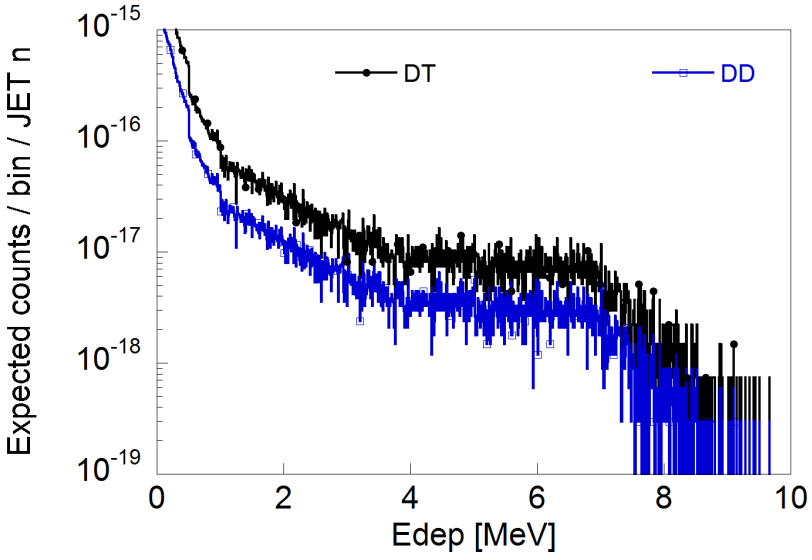

Figure 3.23: Expected deposited energy distribution in the detector due to gamma-ray background for both DD and DT plasmas. For the DD case, only a correction factor from the DT spectrum has been applied.

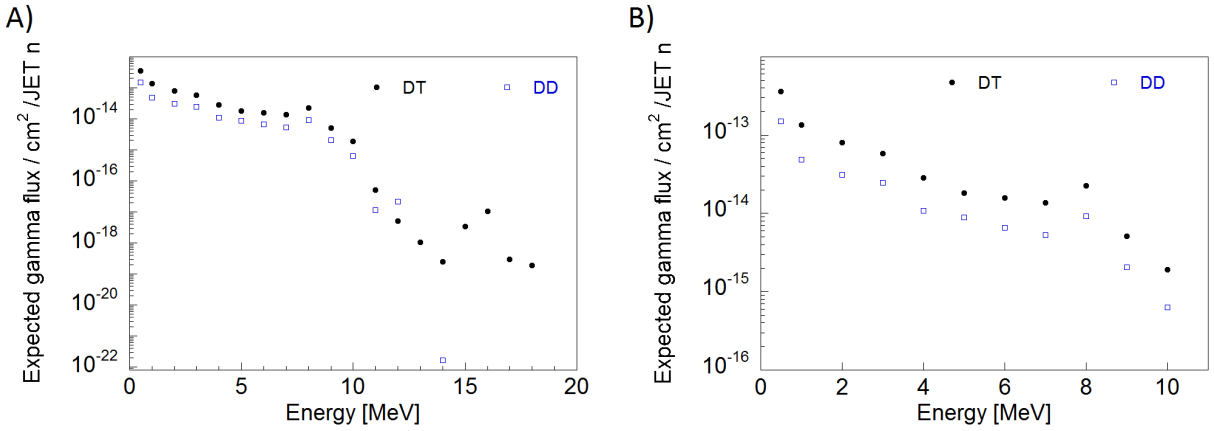

Figure 3.22: A) Expected gamma-ray background fluxes inside the detector box for both DD and DT JET plasmas. B) Zoom of the expected gamma background fluxes.

Energy [keV]	Emitting nucleus
511	pair production
781	^{27}Si
843	^{27}Al
1014	^{27}Al
1386	^{24}Mg
1720	^{27}Al
2210	^{27}Al
2754	^{24}Mg
2981	^{27}Al

Table 3.2: Characteristic γ-rays from interaction between 10 MeV protons and ^{27}Al, through the reactions ^{27}Al(p, nγ)^{27}Si and ^{27}Al(p, $\alpha\gamma$)^{24}Mg [27] .

High rate measurements with p-Al reactions

The experiment was performed at the TANDEM-ALPI accelerator of the Legnaro National Laboratories (LNL) - Italy demonstrating the feasibility of gamma-ray spectroscopy measurements at MHz counting rates with the GCU detector. A beam of 10 MeV protons was accelerated onto a target of ^{27}Al placed in a cylindrical vacuum chamber. The multi gamma lines emission from reactions between protons and ^{27}Al nuclei (see table 3.2) were recorded by the spectrometer at a distance of less than 1 cm from the target (see figure 3.24-left). The target thickness was chosen to fully stop the proton beam maximizing the gamma-ray emission. A LaBr3 crystal coupled to a standard PMT was placed outside the vacuum chamber detecting gamma-rays at counting rates never exceeding 270 kHz. These measurements were used to benchmark the determination of the counting rate on the SiPM detector and the pulse height spectra.

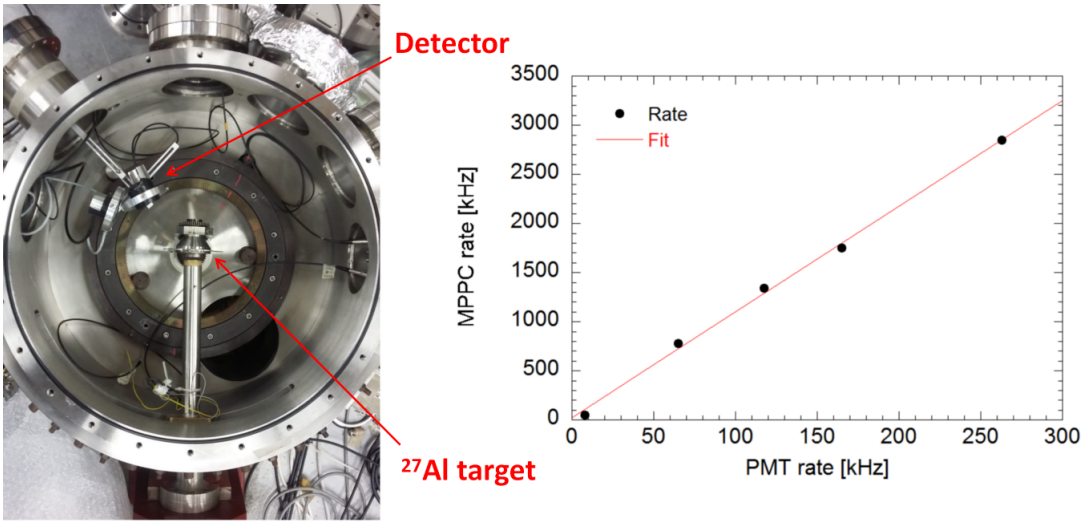

Figure 3.24: (Left) Experimental setup in Legnaro. (Right) Correlation between the MPPC rate and the PMT rate operated at lower counting rates.

The output signal of the detectors were fed into a CAEN digitizer DT5730 (500 MSamples/s, 14 bit) [24] able to samples each single waveform within a 300 ns acquisition window. A post processing based on the interpolation procedure described in [14] has been performed for reconstructing the energy spectra. Each waveform was fitted with the expected pulse shape $y(t)$ from a silicon photomultiplier

$$y(t) = \begin{cases} A & if\ t < t_0 \\ A + N \cdot \left\{1 - exp\left[-\frac{(t-t_0)}{\tau_1}\right]\right\} \cdot exp\left[-\left(\frac{t-t_0}{\tau_2}\right)\right] & if\ t > t_0 \end{cases} \tag{3.10}$$

where τ_1 and τ_2 are constant values for all the waveforms and equal to 30.4 ns and 22.6 ns, respectively. A, N and t_0 are free parameters derived by the fitting procedure. A dedicated algorithm was used to recognition and reject the pile-up events. Figure 3.25 shows the energy spectra recorded simultaneously by the SiPM detector and the PMT detector both at low counting rate. From these graph we find that the two spectrometers have observed the same gamma-ray lines. The counting rates r have been estimated by averaging the number of pulses recorded in several acquisition windows lasting 1 μs and launched before each measurement of the spectrum without any energy threshold. The rates increased as a function of the proton beam current and r remained proportional to the rate of the external detector equipped with PMT (see figure 3.24-right). During the experiments, counting rates from 52 kHz up to 2.9 MHz have been explored. From figure 3.26-A-B we find that even at counting rates approaching 2 MHz it has been possible to resolve all the peaks in the spectra. In these measurements we operated the device at 0.6 V above the break down voltage. A broadening of the peaks has been observed for higher

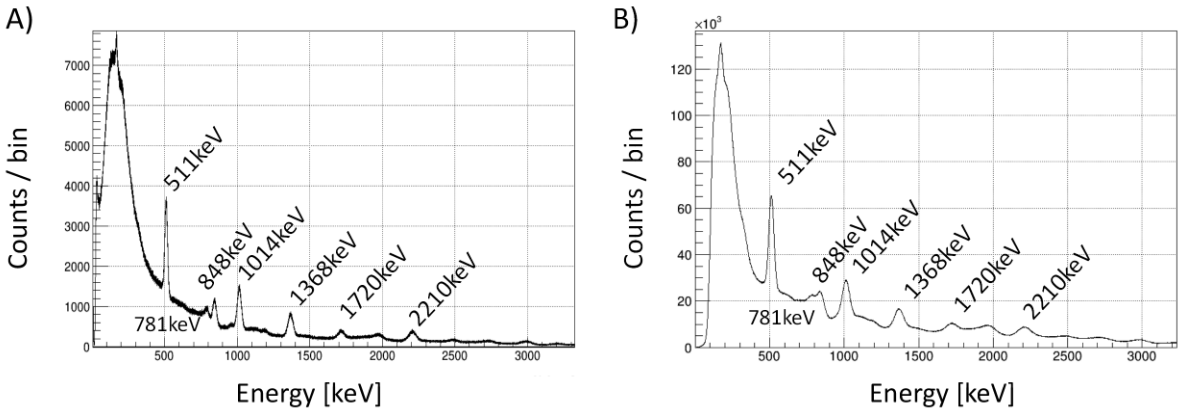

Figure 3.25: Gamma-ray emission spectrum from p+^{27}Al reactions recorded by the detectors equipped with PMT (A) and SiPM (B) both at low counting rate.

counting rates, indicating a worse energy resolution. The latter has been quantified as a function of the rate and it is shown in figure 3.26-D. As expected for a given counting rate it scales as $1/\sqrt{E_\gamma}$ and a value between 3 % - 4 % can be extrapolated at 4.44 MeV at 1.75 MHz counting rate. By decreasing the operational voltage of the Silicon PhotoMultiplier i.e. only about 0.3 V above the break down we managed to use the detector at a counting rate of 2.9 MHz, corresponding to a proton beam current of 30 nA which is the highest value allowed by radiation protection limits.

Of particular interest is the downward shift of the mean peaks position observed as a function of the counting rate and illustrated in figure 3.27. This effects is mainly due to the increasing average current $< I_s >$ flowing in the device. It is linearly proportional to the counting rate and to the equivalent energy deposited which, in this case, was about 660 keV ($< I_s > \propto < E_\gamma > \cdot r$). The increasing of $< I_s >$ results in voltage drop along the resistor R1 in figure 3.7 and the SiPM itself. Another contribution comes from the increase of the local temperature of the device due to Joule effect induced by the $< I_s >$ which further reduces the gain of the Silicon PhotoMultiplier. By analysing time resolve measurements, we could separate these two contribution: the voltage drop appears immediately, instead the local heating occurs until thermal equilibrium is reached on a time scale of a few seconds. In figure 3.27 we only show the first unavoidable contribution. The latter, instead, could be compensated by adjusting the gain of the Silicon PhotoMultiplier with a temperature feedback sensor.

High rate measurements with LED pulses

In order to study the behavior of the detector at higher counting rates, several tests with blue LED pulses were performed in laboratory. Two LEDs were powered by Keysight

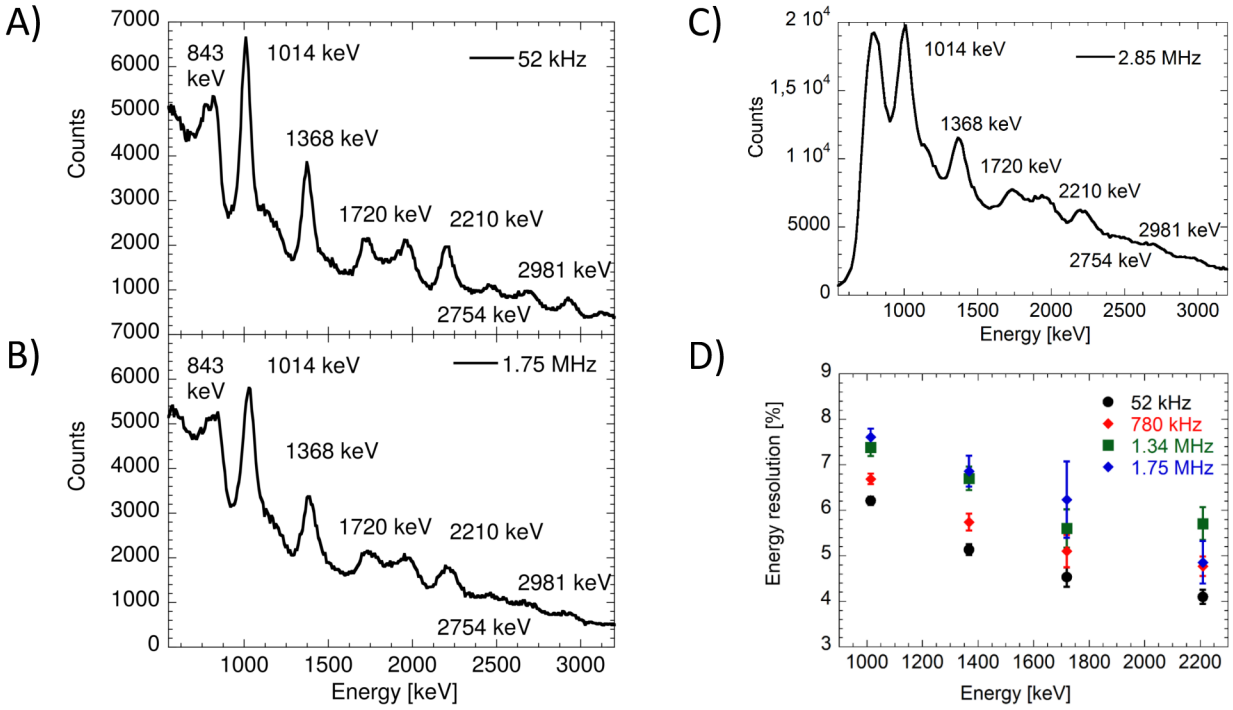

Figure 3.26: Recorded PHS at 52 kHz (A), 1.75 MHz (B) and 2.85 MHz (C). Panel (D) shows the energy resolution as a function of the counting rate [paper II].

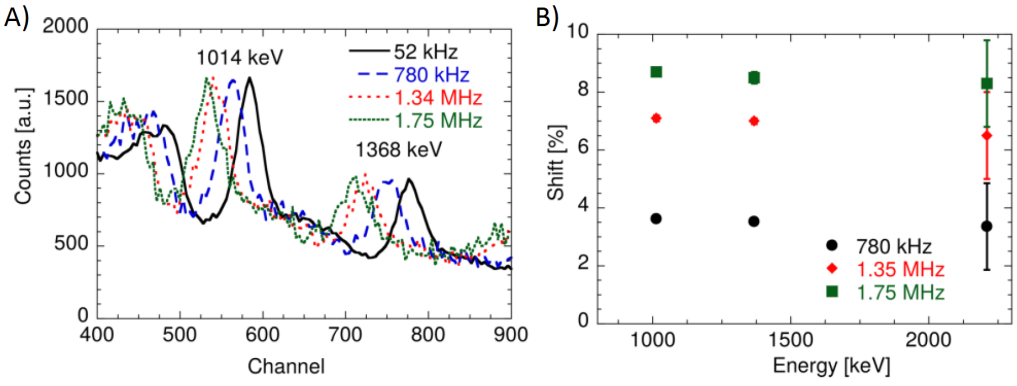

Figure 3.27: (A) Downward shift of the mean peaks position due to the increase of the average current flowing in the device. Spectra were normalized to the amplitude of the spectrum at 52 kHz. (B) Relative shift of the mean peaks position as a function of the counting rate and with respect to values at 52 kHz. [II]

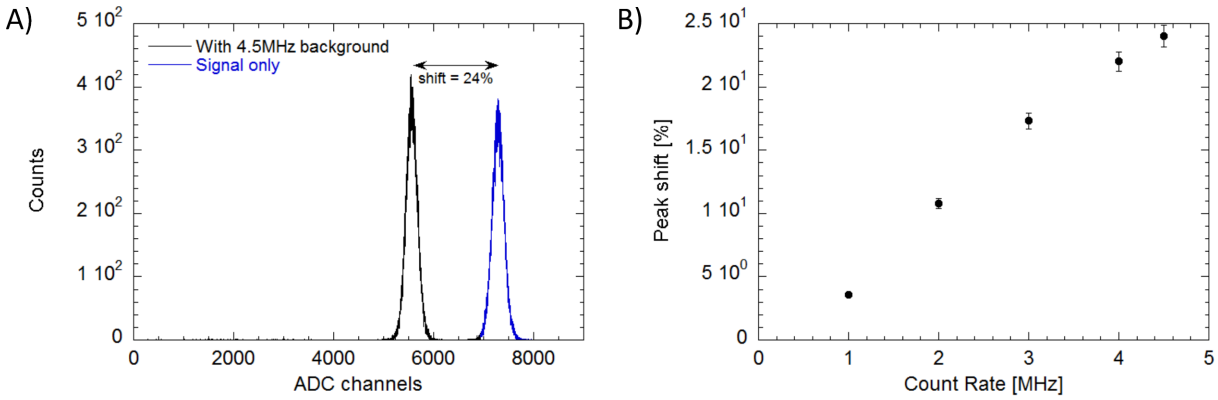

Figure 3.28: (A) Example of downward shift of the mean reference peak position observed for a perturbation rate of 4.5 MHz and $< E_\gamma > \simeq 550$ keV. (B) Shift of the mean reference peak position as a function of the counting rate from 1 MHz up to 4.5 MHz. The $< E_\gamma >$ of the perturbation LED was kept equal to 550 keV, as expected for the high flux background at JET.

(model 81150A) pulse generator and sent it to the detector illuminating the Silicon PhotoMultiplier. A ^{137}Cs source was placed in the vicinity of the detector providing a reference signal. One LED was used as perturbation, providing high fluxes at a defined equivalent energy. The other LED, instead, was used as reference with fixed rate (10 kHz) and equivalent energy of about 4.4 MeV. First, in order to benchmark our measurements with LED pulses, we reproduced in laboratory the experimental conditions in Legnaro in terms of counting rate and equivalent energy $< E_\gamma >= 660$ keV, confirming the reliability of the experiment. In fact, same results were obtained in terms of peak shift.

Second step was done by roughly simulating the high rate environment expected at JET in which the high rate is supposed to be only in a short time windows, i.e. 10 s. Now a sequence of LED pulses with $< E_\gamma > \simeq 550$ keV was delivered at high rate in a 10 seconds time window providing the perturbation signals. As before, a peak shift in the reference signal has been observed (figure 3.28-A) and assessed (see figure 3.28-B) as a function of the counting rate from 1 MHz up to 4.5 MHz. A downward shift of the mean reference peak position was estimated to be of about 2%, 4% and 24% at 500 kHz, 1 MHz and 4.5 MHz, respectively. We found that the peak shift was observed to increase at higher SiPM bias voltages and at larger intensities of LED perturbation source which corresponds to higher $< E_\gamma >$.

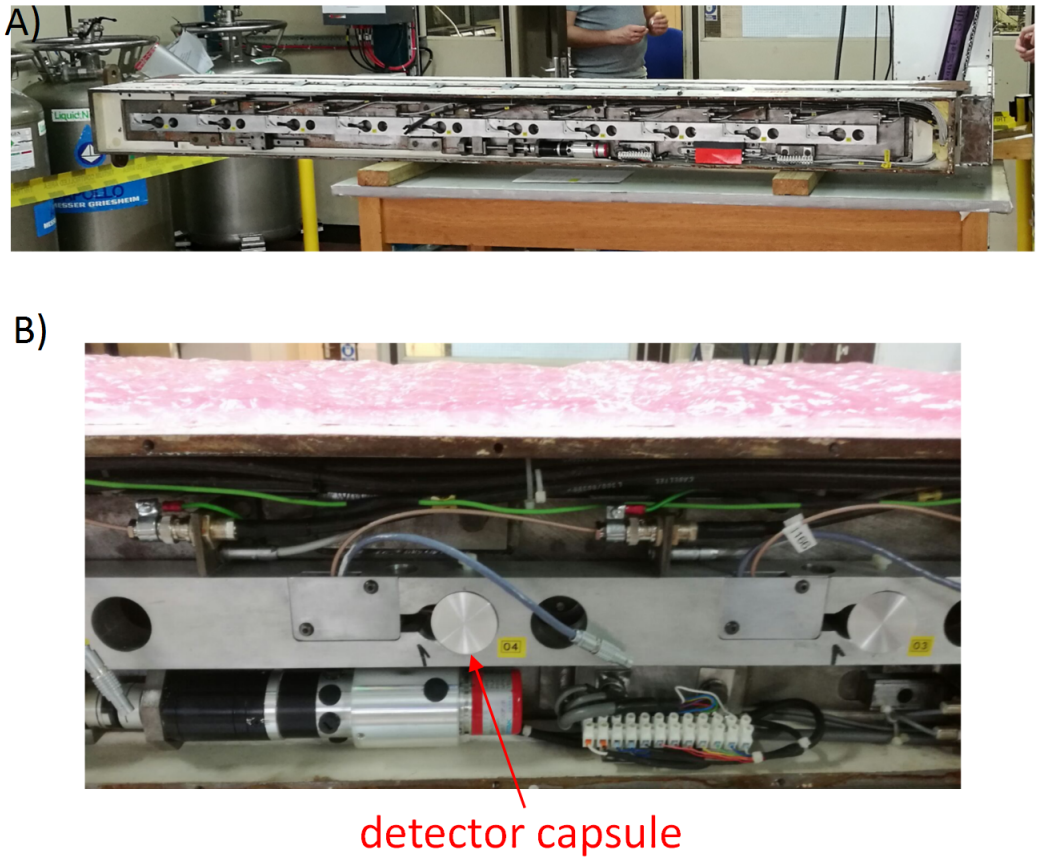

Figure 3.29: A) Picture of the horizontal camera during the detector installation. B) Picture of the horizontal with a detector capsule already installed.

3.8 Detectors installation at JET and expected capabilities of the GCU

All the 19 GCU detectors have been produced and installed on both the vertical and the horizontal cameras of JET (see figure 3.29). The crystals have been coupled to SiPMs by using a Thermal Plastic Material (Cargille Meltmount Code 53 Cat.#24140) which works as glue. Its melting point is between 60 – 70 °C and at these temperatures the crystals and the SiPMs can be uncoupled. The Silicon PhotoMultiplier is placed on a Printed Circuit Board (PCB) which combines the read-out circuit and the temperature sensor. The temperature monitoring is used to adjust the bias voltage as a function of the temperature variations and it was provided, together with the bias voltage supplies, by our Polish colleagues who were partners in the project. Due to space and cabling limitations, no gain monitor systems based on LED pulses can be installed on each detector of the gamma camera. However, as described in [paper I], the intrinsic radioactivity of the $LaBr_3(Ce)$ can be used in between two JET discharges (which is about 20 minutes) to evaluate gain drifts of few % by monitoring the position of the peak at 1.436 MeV (see

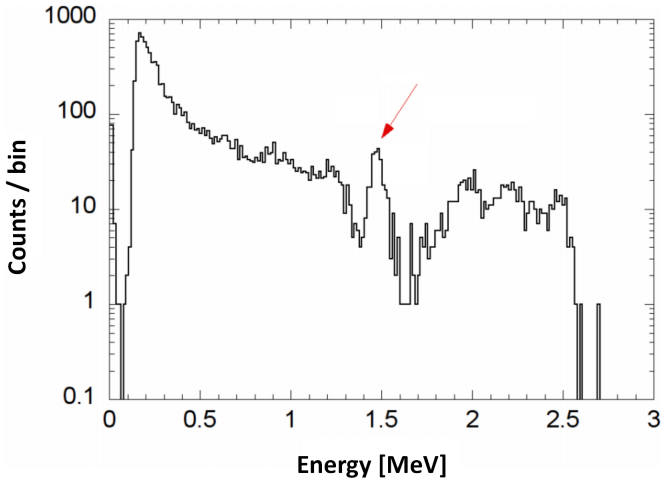

Figure 3.30: Pulse height spectrum of the intrinsic radioactivity of a 25.9 mm x 16.9 mm $LaBr_3(Ce)$ crystal over 20 minutes of measurements [paper I].

figure 3.30). In order to increase the light collected by the SiPM, an aluminum ring followed by an isolator ring, have been placed in between the crystal and the PCB. The detector is placed inside an aluminum capsule with outer dimension at diameter 35.0 mm x 35.0 mm. Two cables come out from the capsule. One is terminated with a BNC connector providing the output signal from the detector and it match the standard JET cable impedance of 75 ohm. The other one is equipped with a 4-pin LEMO connector (type FGG.0B.304.CLAD52) which provides the following connections: temperature output signal from the temperature sensor, the bias voltage for the temperature sensor, the ground and the SiPM bias voltage. The detectors have been successfully installed in the JET Torus Hall with 80 m long cables and characterized with 1 hour measurement with ^{137}Cs, ^{133}Ba and ^{22}Na sources (see figure 3.31 A) present in the collimators. For the first time the gamma camera detectors were able to resolve the three γ-ray lines from ^{133}Ba (see figure 3.31 B) highlighting the clear improvement in terms of energy resolution. Finally, figure 3.32 shows the energy resolution of the 19 detectors for the ^{137}Cs full energy peak and an example of pulse signal recorded with 80 m long cable after the installation in the JET Torus Hall. The upgraded GC is therefore ready to collect data in the next high power D and DT campaigns.

The results achieved so far with the GCU detectors [see papers I, II and III] are quite promising in view of the next JET campaigns. Laboratory measurements with radioactive sources have shown an excellent energy resolution which depends on the bias voltage of the device. Its optimum is at about 2.5 V above the break-down voltage corresponding to an energy resolution of about 5 %. Although the Silicon PhotoMultiplier presents a non-linear behavior at high gamma-ray energies, this does not prevent the measurement

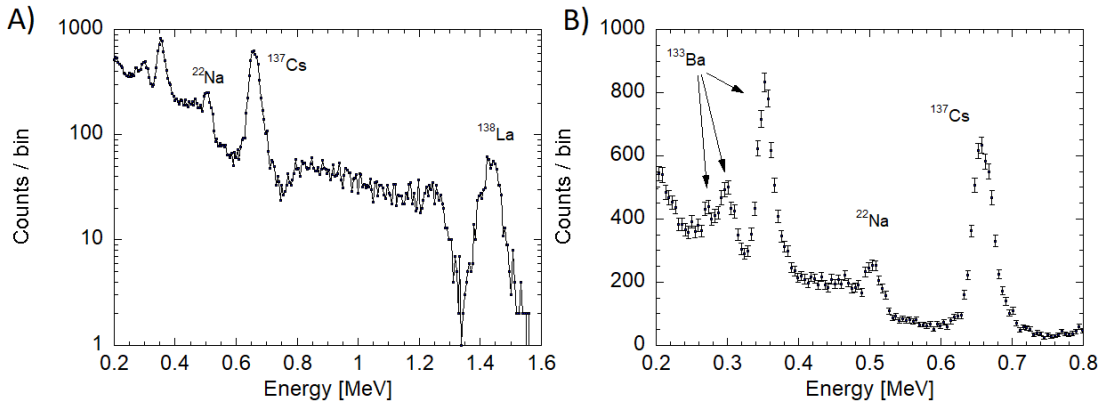

Figure 3.31: A) Example of pulse height spectrum recorded by channel 7 of the gamma camera after the installation in the JET Torus Hall. During 1 hour measurement, gamma-rays from ^{137}Cs, ^{133}Ba and ^{22}Na γ-ray sources were recorded together with the intrinsic activity of the ^{138}La. Figure B) shows in detail the three γ lines of the ^{133}Ba, together with the 0.511 MeV and 0.662 MeV peaks from ^{22}Na and ^{137}Cs, respectively.

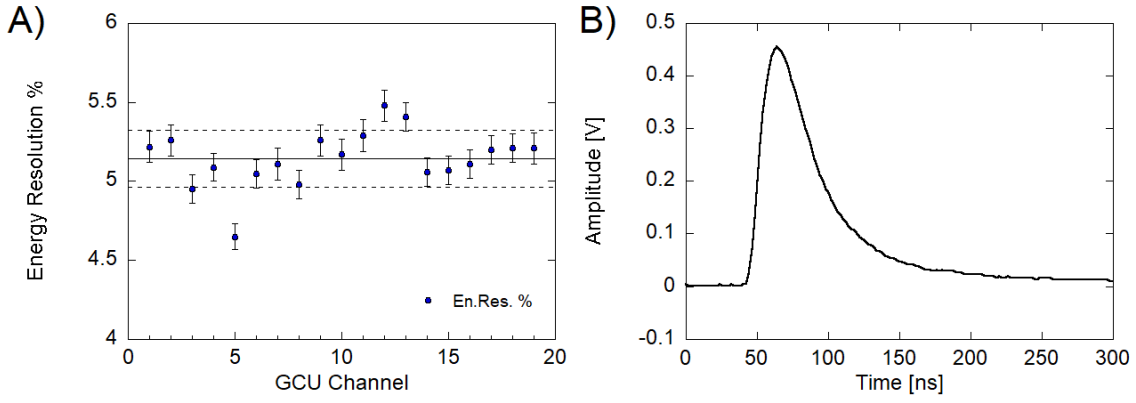

Figure 3.32: A) Energy resolution of the 19 detectors evaluated for the ^{137}Cs full energy peak after their installation in the JET Torus Hall. B) Example of pulse signal from channel 7 of the JET gamma camera.

of 4.44 MeV γ-rays provided that an off-line correction is done. We tested the feasibility to operate the GCU detector up to about 3 MCounts/s in a nuclear facility and up to 4.5 MCounts/s with LED pulses. As expected we found a dependence between the shift of the mean peaks position and the equivalent energy deposited as well as the counting rate. We also noticed that the peak shift decreases for lower bias voltage of the Silicon PhotoMultiplier. Consequently, a trade-off between energy resolution and performances at high rate needs to be achieved depending on the plasma scenario. No limitations are expected for the next full power JET DD campaigns. Concerning the operation in DT plasma, instead, the MCNP simulations of the γ-ray background together with the benchmark measurements of the background in DD JET plasma, revealed that the neutron induced γ-rays background fluxes are high. This is due to a poor γ-ray shielding and neutron attenuator provided by the gamma camera. On the basis of the calculations, we can assert that the upgraded gamma camera would correctly operate up to 10^{17} n/s.

The upgrade of the gamma camera brings favorable expectations for the study of the fast ions in the MeV energy range. From calculations reported in [23], we could expect a counting rate of the order of a few kHz in the 4.44 MeV full energy peak allowing to track fast alpha particles profile changes during their slowing down time, as well as of other energetic ions. Improved counting rate capability opens up to measurements on time scales shorter than the fast ion slowing down time (which is of the order of the second). The obtained good energy resolution allows better resolving the peaks standing the spectrum and avoiding possible artifacts in the reconstructed fast ion profile. A further study that can be done is the measurement of the MeV range spectrum from bremsstrahlung emission produced by runaway electrons (REs). Nowadays, the study and the control of the REs is an high priority issues since they can significantly damage the first wall of the reactors. Runaway electrons are generated during plasma disruptions occurring in the time scale of milliseconds. When they interact with the tokamak structures, an intense burst of hard x-ray in the MeV range can be created from bremsstrahlung emission. The expected counting rate in the GC detectors can be as high a a few MHz. The gamma camera upgrade can provide the spatially resolved measurements of the runaway electrons energy distribution with a time resolution better than 10 ms. All these measurements are not compatible with the old CsI detectors of the gamma camera, due to their poor energy resolution and slow time signal. Gamma-ray images, in fact, were often not available in high power DD plasma and have never obtained in trace tritium and DT discharges.

Chapter 4

Single crystal diamond neutron spectrometers

4.1 Diamond detectors

In last years artificial single crystal diamond detectors (SCD) have shown excellent performances as neutron detectors. Their spectroscopic capabilities have been demonstrated at nuclear accelerators [papers IV, V and VI] and have been exploited for measurements of 2.5 MeV neutron spectrum in deuterium plasmas at JET [28]. Single crystal diamond detectors feature high radiation hardness, fast response time, insensitivity to magnetic fields, compact size and low sensitivity to gamma-rays. These makes diamond detectors interesting candidate for neutron measurements in the harsh environment of a high power tokamak. Neutron detection is based on the collection of the e^--h pairs produced by charge particles generated by the neutron interaction with ^{12}C carbon nuclei. The main nuclear reaction channels between ^{12}C and neutrons in the energy range of interest for plasma diagnostics are the follows (see figure 4.1):

- elastic and inelastic scattering reactions $^{12}C(n,n')^{12}C$;
- n-3α reaction (carbon breakup) $^{12}C(n,n')3\alpha$ with negative Q_{value}=-7.23 MeV;
- n-α reaction $^{12}C(n,\alpha)^{9}Be$ with negative Q_{value}=-5.702 MeV;

The latter reaction is the main candidate for the spectroscopy of 14 MeV neutrons, since it leads to a well defined peak centered at $E_{dep} = E_n - 5.702$ MeV. It provides a univocal one to one relation between the incoming neutron energy and the measured deposited energy. The shape of this peak is due to two contributions: the intrinsic broadening of the detector itself which depends on its energy resolution and an additional kinematic broadening due to the energy distribution of the incoming neutrons. The analysis of this

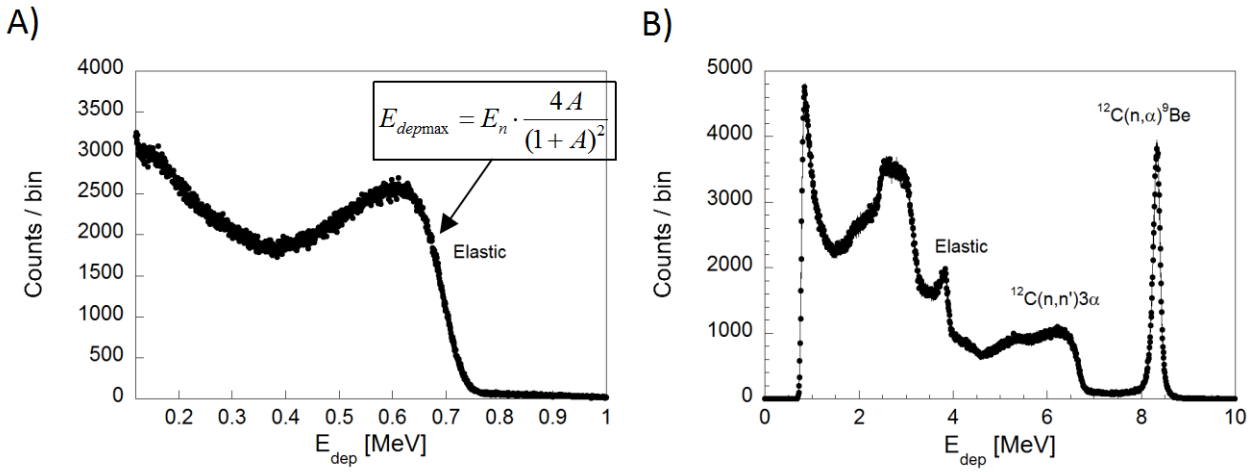

Figure 4.1: A) Pulse height spectrum produced by irradiating a diamond detector with 2.5 MeV neutrons. B) Pulse height spectrum produced by irradiating a diamond detector with 14 MeV neutrons. The possible channel reactions are listed in the graphs (A and B), together with the formula which links the maximum energy deposited by elastic scattering and the incoming neutron energy.

peak can retrieve information on the incoming neutrons and consequently can be used as plasma diagnostics. As shown in [28], similar considerations can be applied to the shape of the elastic edge produced by elastic scattering reaction, whose maximum deposited energy is determined by the formula:

$$E_{dep-max} = E_n \cdot \frac{4A}{(1+A)^2}$$

where A is carbon mass number, namely 12. Due to the cross-section of the reactions, 2.5 MeV neutrons can interact with ^{12}C only through elastic scattering reactions.

In view of the forthcoming JET deuterium-tritium campaign, it has become necessary the installation of new neutron detectors on the torus vertical radial line of sight (LOS). This LOS, in fact, had not yet provided by 14 MeV neutron spectrometers suitable for DT plasmas. For this reason two neutron detectors have been installed. They consist in a NE213 liquid scintillator and a diamond base spectrometer. This second part of the thesis is focused on the diamond based one which has been developed for high resolution neutron spectroscopy measurements of 14 MeV coming from DT plasmas. The VNS diamond offers also the possibility to perform 2.5 MeV neutron spectroscopy with moderate energy resolution on D plasmas.

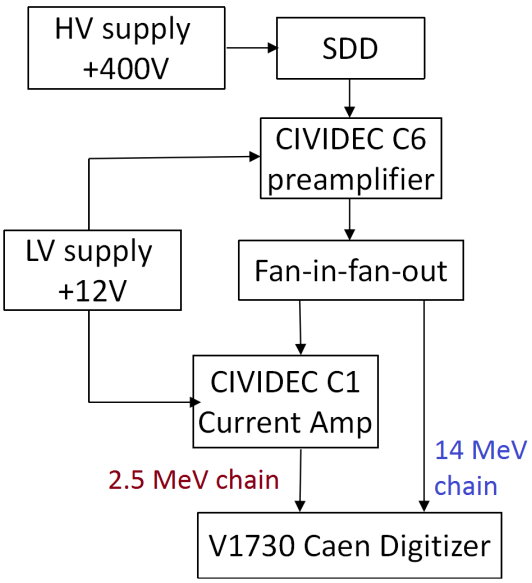

Figure 4.2: Schematic of the electronic chain used for the diamond VNS.

4.2 Vertical Neutron Spectrometer - diamond matrix

The vertical neutron spectrometer based on diamonds (DVNS) is a 12-pixels single crystal diamond matrix built at the CNR-ISM institute in Rome (see figure 4.4 B and C). Each pixel consists in an synthetic single crystal "electronic grade" sample (4.5 mm x 4.5 mm, 500 μm thick) grown by the Element Six Ltd [29] by chemical vapour deposition (CVD) process. Ohmic contacts were obtained on top and bottom surfaces by sputtering deposition of a multi-layer metal structure and finished with a thin gold layer to improve the weldability. The 12 pixels are placed on a alumina Printing Circuit Board (PCB) which in turn is housed in a properly designed aluminum metal case in order to shield it from electromagnetic interferences and to give the detector mechanical resistance. The case is equipped with 12 SMA connectors for pixel biasing and signal collection. Each pixel is equipped by independent electronic chains which allow achieving excellent energy resolution and MHz counting rate capabilities. These two requirements are essential conditions for neutron spectroscopy measurements on high power tokamaks, such as JET and ITER. The spectrometer has been recently installed at JET in 2015 (see figure 4.4 D) sharing the same line of sight of a non-compact advance 2.5 MeV neutron spectrometer namely, TOFOR (Time-Of-Flight neutron spectrometer Optimized for high count Rate measurements) at about 20 m from the plasma and 25 cm above the TOFOR (see figure 4.4 A). Each pixel is provided by two simultaneous electronic chains optimized for the spectroscopy of 2.5 MeV and 14 MeV neutrons namely for D and DT plasmas, respectively (see figure 4.2). The output signal from a pixel is fed into a CIVIDEC C6 fast charge preamplifier [30] for a first stage of amplification and then sent into a CAEN

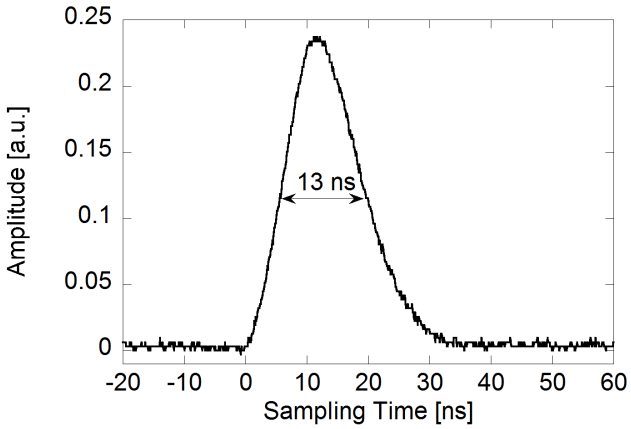

Figure 4.3: Output signal from the DT electronic chain.

FIFO (Fan In Fan Out) module able to split the signal. The signal corresponding to the DT electronic chain is directly connected to the digitizer whereas the D signal is further amplified by a fast current amplifier CIVIDEC C1 [30] and then sent to the digitizer. This second stage of amplification is due to the fact that the energy deposited through elastic scattering by 2.5 MeV is at least 10 times lower than the one deposited by 14 MeV neutrons through n-α reaction. The signals are acquired by two 500 MHz, 14 bit CAEN V1730B VME modules equipped with DPP-PSD firmware able to perform online analysis by calculating the pulse area. The use of online processing has become necessary due to the high counting rates expected in DT plasma operation which would results in a large amount of recorded data. The electronic chain has been optimized in order to achieve a signal length of about 13 ns FWHM (see figure 4.3) reducing the pile-up event probability which can affect the diagnostic capabilities of the instrument. My activity concerning the diamond neutron spectrometers was focused on the calibration and characterization of the DVNS which are reported in manuscripts [papers IV and V], as well as on the data validation analysis of the instrument during the D plasma operations. Furthermore in view of the next DT campaign, the capabilities of the diamond detectors by measuring 14 MeV neutrons have been exploited by characterizing the 14 MeV neutron generator used for the calibration of the JET neutron diagnostics. The measurements and the analysis reported in [manuscript VI], allowed demonstrating the capability to accurately determine the detailed ion composition of the mixed D/T beam.

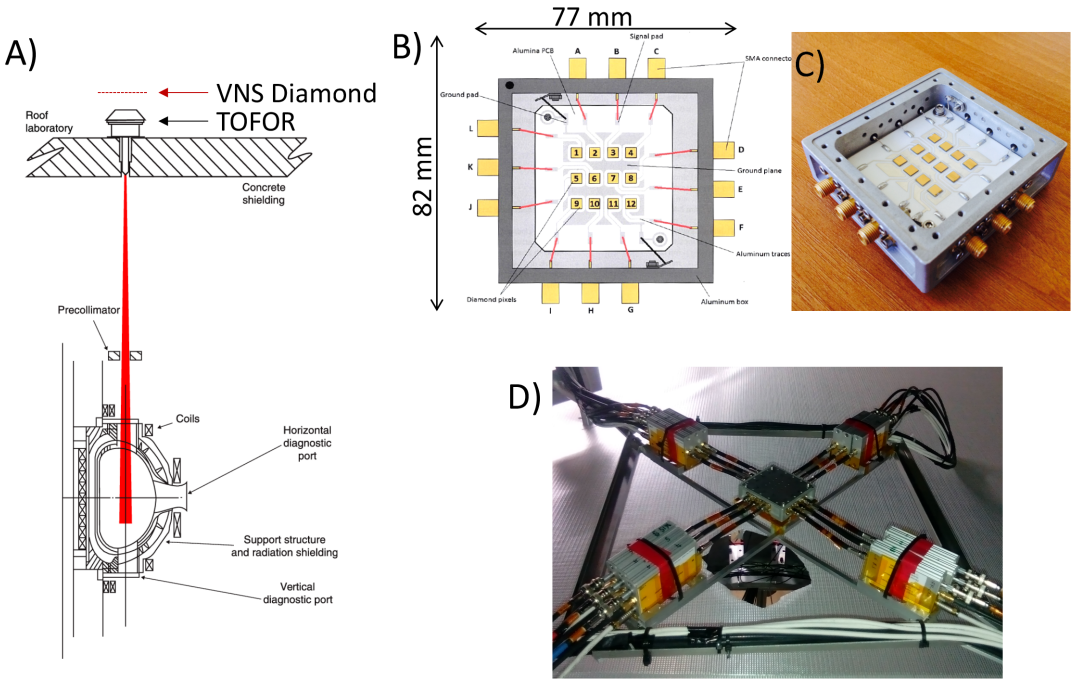

Figure 4.4: A) Position and line of sight of the VNS diamond matrix at JET. Courtesy by [31]. Figure B and C show the schematic and the picture of the VNS diamond matrix, respectively. In figure D the VNS diamond matrix, together with the 12 CIVIDEC C6 fast charge preamplifiers are shown after the installation at JET.

4.3 Calibration and characterization measurements of the diamond matrix

The diamond matrix has been successfully characterized with alpha particles and neutrons. Alpha particle measurements have been performed both in air at atmospheric pressure and in vacuum at the Istituto di Fisica del Plasma in Milano, Italy. A vacuum chamber was used to place the diamond matrix together with the preamplifiers and ^{241}Am α source, allowing minimizing the alpha particle energy straggling. The top surface of the matrix casing was equipped by 12 holes working as pinhole collimators for the α particles. Measurements were performed pixel by pixel acquiring the signals with 15 m long cables which are currently used at JET.

As referred in [papers IV-V] the diamond matrix has been calibrated and characterized at the Frascati Neutron Generator and at the Institute of Heavy Ion Physics of the Peking University (China) providing the measured response function of the detector in the neutron energy range from 1 - 20 MeV (see figure 4.6 A - B). In particular, figure 4.6 A shows the detector response to quasi monoenergetic neutrons with energy of 1 MeV, 2 MeV and 2.5 MeV, respectively. The recorded spectra feature a continuous shape produced by the only reaction channel occurring for these energies, namely the elastic

scattering reactions which ends with the characteristic elastic edge placed in the spectra at $E_{dep-max} = E_n \cdot 0.284$. Figure 4.6 B, instead, exhibits the detector response to quasi monoenergetic neutrons with energy of 14 MeV, 17 MeV and 20 MeV, respectively. Here the spectra feature a more complex structure due to different nuclear reactions which open up. In addition to the main nuclear reaction channels described in section 4.1, for 20 MeV neutrons, further reaction channels occur among which the ^{12}C(n,d)^{11}B and ^{12}C(n,p)^{12}B reactions with Q_{value} of -13.732 MeV and -12.587 MeV, respectively [32]. As shown in figure 4.5 we find a uniform response of the 12 pixels and we observe a small shift between the n-α peaks due to the different solid angle subtended by the diamond pixels during the measurements. The intrinsic broadening of the neutron beam has been calculated by modeling the target in terms of geometry and materials and the target-beam reactions with the code TARGET [33]. This allowed estimating an intrinsic energy resolution for 14 MeV neutrons of about 120 - 130 keV at FWHM in the n-α peak which does not improve as $1/\sqrt{E_n}$ indicating that the electronic noise is the main contribution to the energy resolution. The enhanced energy resolution of the single crystal diamond detectors opens up new prospects for diagnosing DT plasmas. An example is shown in [papers V and VI] in which we explored the possibility to perform beam ions studies on both JET and ITER machines. Here we demonstrated the feasibility to observe the non-classical slowing down of the beam ions thorough high resolution neutron spectroscopy with diamond detectors. As shown in [papers VI] the diagnostic capabilities of the diamond detectors have been confirmed during the characterization measurements of a compact 14 MeV neutron generator based on DT reactions. The energy resolution of the single crystal diamond detector allowed the complex features of the neutron energy spectra resulting from the mixed D/T beam ions interacting with the T/D target nuclei to be resolved for the first time.

Neutron spectroscopy with moderate energy resolution is also possible on D plasmas. During the C35 JET campaign, first diagnostic capabilities of the VNS diamond matrix have been demonstrated on D plasmas and the results are shown in next section.

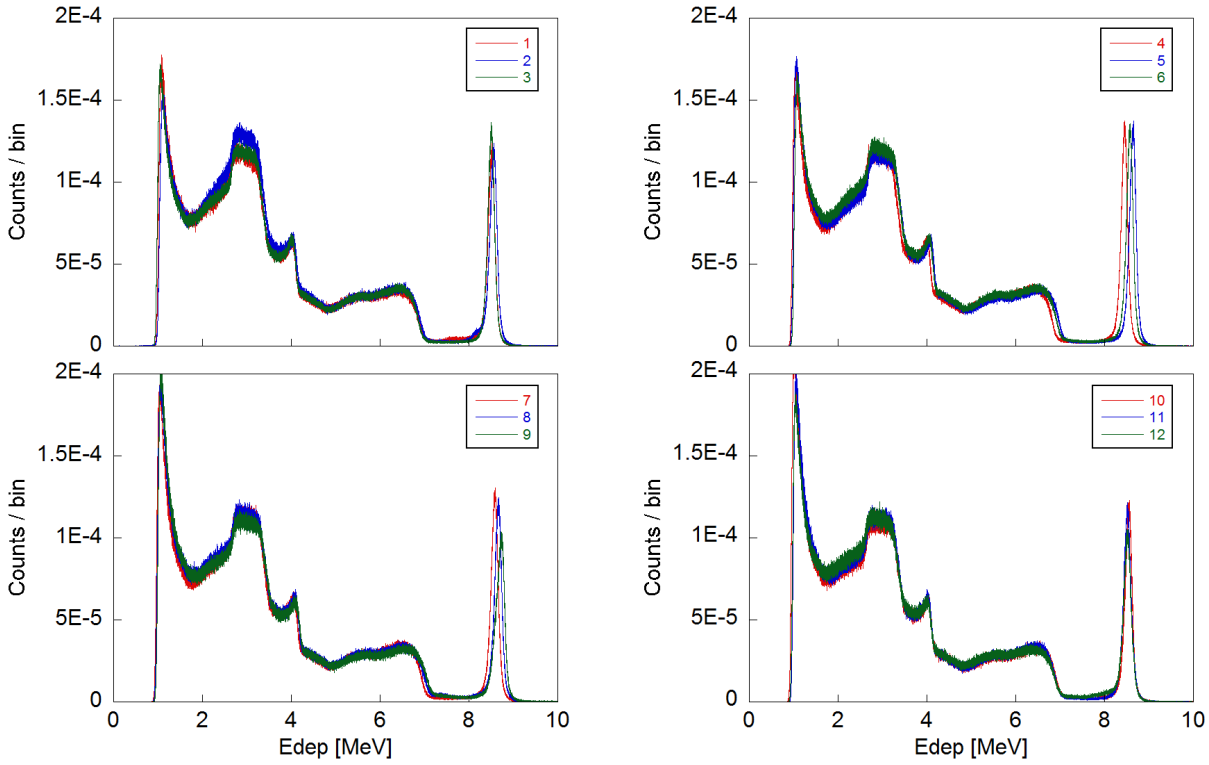

Figure 4.5: Pulse heigth spectra recorded by the 12-pixels single crystal diamond matrix at the Frascati Neutron Generator.

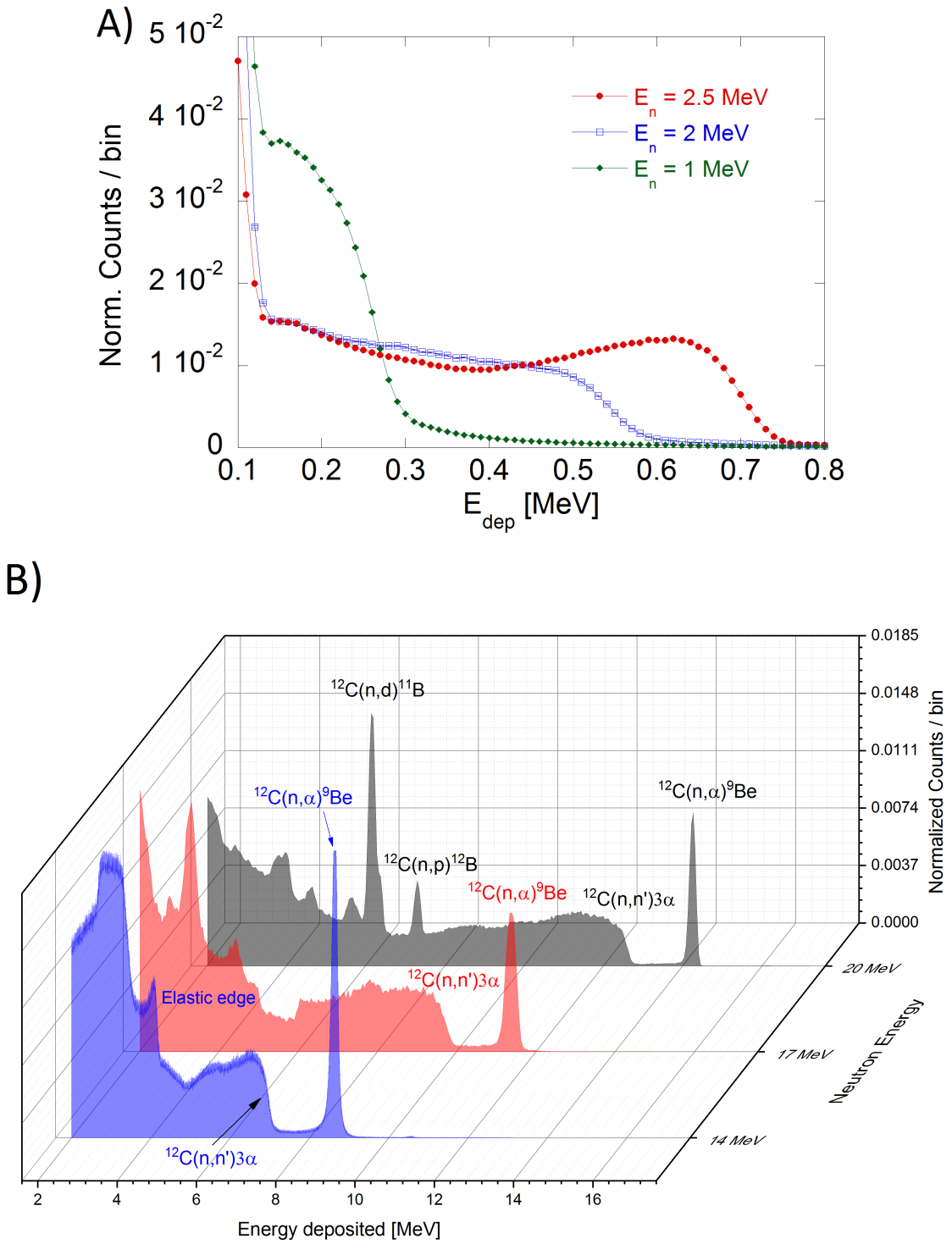

Figure 4.6: Measured response function of a diamond detector to quasi mono-energetic neutrons. Pulse height spectra in graph A have been recorded with the D electronic chain. Pulse height spectra in graph B have been recorded with the DT electronic chain.

4.4 Example of 2.5 MeV JET data

The VNS diamond matrix is currently operating at JET and collecting data since late 2015. First 2.5 MeV neutron spectroscopy measurements on D plasmas have been performed during the C35 and C36 JET campaigns and used to evaluate and validate the detector capabilities. Compared to the quasi mono-energetic 2.5 MeV neutron spectrum, we find from figure 4.7 a significant broadening in the elastic edge when the deuterium plasma is heated by Neutral Beam Injector (NBI) with an average power of about 17 MW. When energetic neutral particles are injected into the plasma, they are ionized by collision with plasma particles so that they are kept confined by magnetic fields and can transfer their energy by further collisions with the plasma. The broadening is even more pronounced when the plasma heating system is a combination of NBI and ICRF heating. Here we find an increased high energy tail which is due to the acceleration of the deuterons up to few MeV from the synergistic effect of fast ions and RF waves [34]. These results highlight the spectroscopic capabilities of the detector which, although was designed and optimized for DT plasmas, offers the possibility to perform 2.5 MeV neutron spectroscopy with moderate energy resolution on D plasmas.

The data collected by the VNS diamond matrix have been validated by comparison with the measurements of the reference 2.5 MeV neutron spectrometer at JET, namely TOFOR which shares the same line of sight of the VNS. As shown in figure 4.8 A) and C) the TOFOR data have been analyzed in order to infer the different spectral components (thermal component, NBI component, RF component, scattered neutrons), therefore obtaining the total neutron spectrum which better describes the TOFOR data in terms of chi-square value (see figure 4.8 B) and C)). Consequently the total neutron spectrum has been convoluted with the diamond response function [35] and summed to the expected gamma-ray background at the detector position whose deposited energy spectrum was previously calculated by MCNP simulations. Figure 4.9 reveals a good agreement with data and consequently to the TOFOR data. Waiting for the forthcoming DT JET campaign, the excellent spectroscopic capabilities of the diamond detectors for 14 MeV neutrons have been deeply studied and explored during the characterization of a 14 MeV neutron generator [paper VI] and are described in next section.

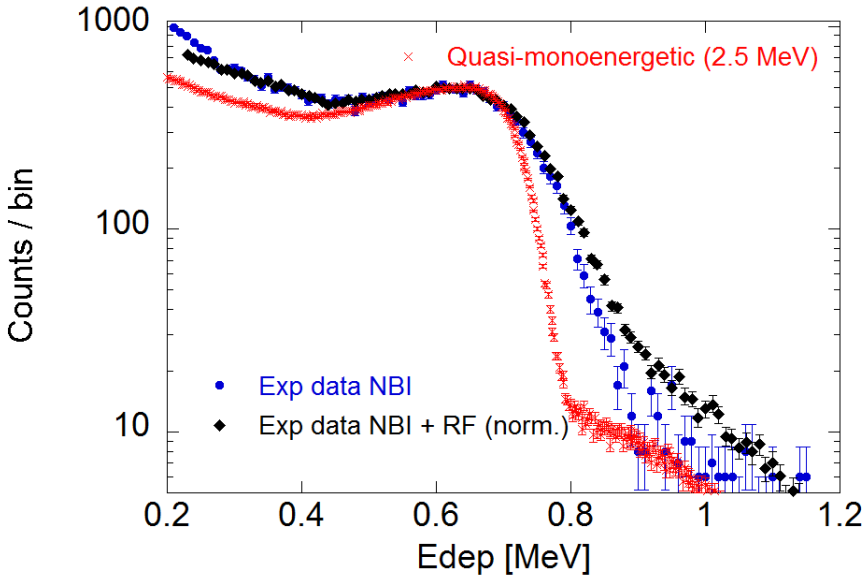

Figure 4.7: Comparison between quasi mono-energetic 2.5 MeV neutron measurements (red cross) and JET measurements with NBI (blue circle) plasma heating and NBI+RF (black rhombus) plasma heating. In order to have a better statistic, a few JET discharges have been summed. NBI: 92169, 92170, 92171, 92172, 92176. NBI+RF: 92068, 92069, 92070, 92071, 92309, 92310, 92311, 92312, 92313, 92314. As reference we used the quasi mono-energetic 2.5 MeV measurement performed at the Institute of Heavy Ion Physics of the Peking University (China).

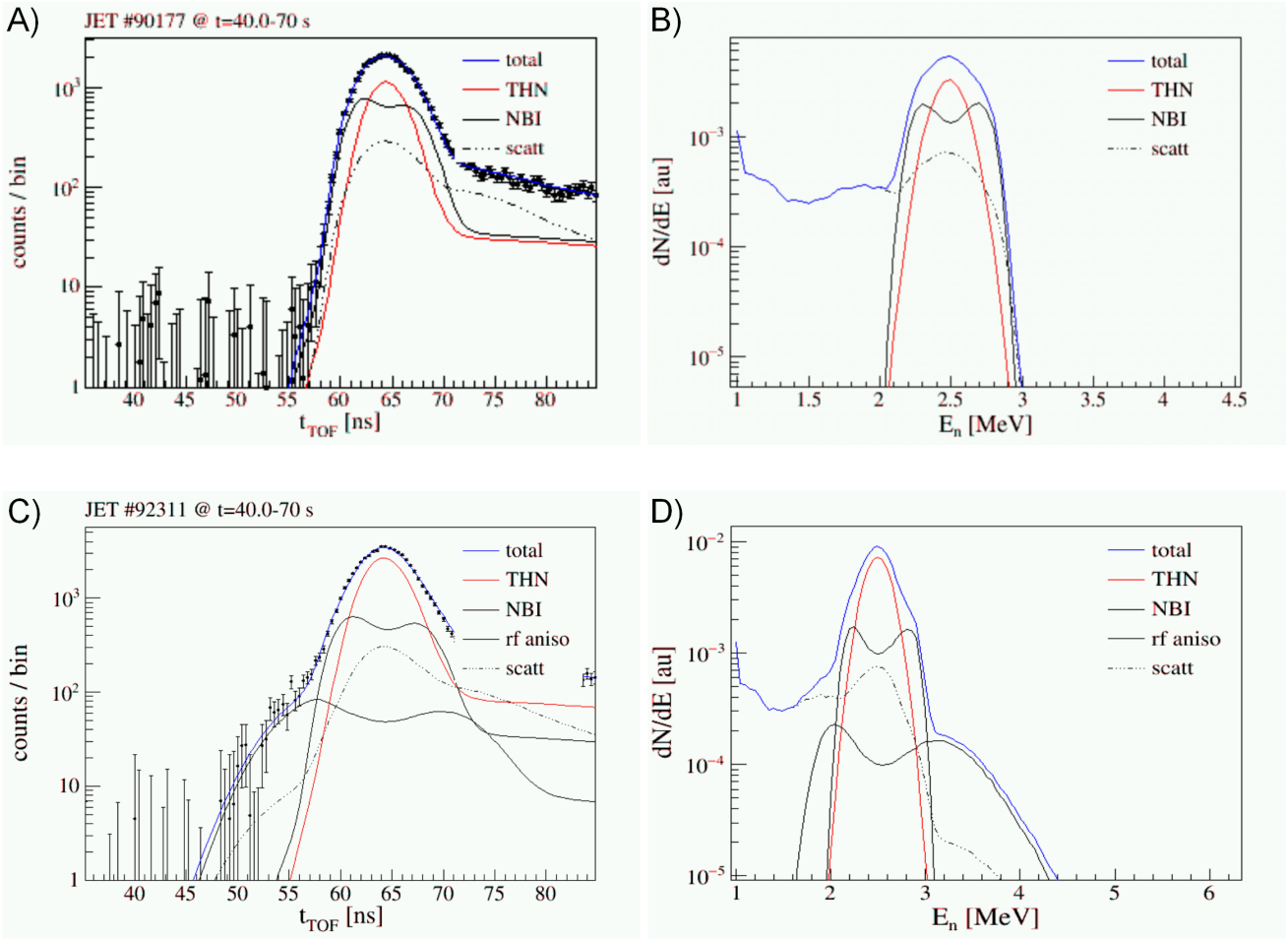

Figure 4.8: Graphs A and C represent the pulse height spectra recorded by TOFOR during NBI and NBI+RF plasma heating systems, respectively. Data are shown with black dots, while lines are the different spectral contributions weighted on the base of the fit results. Graphs B and D are the estimated incoming neutron spectra, together with their different contributions (thermal, NBI, RF and scattered neutrons).

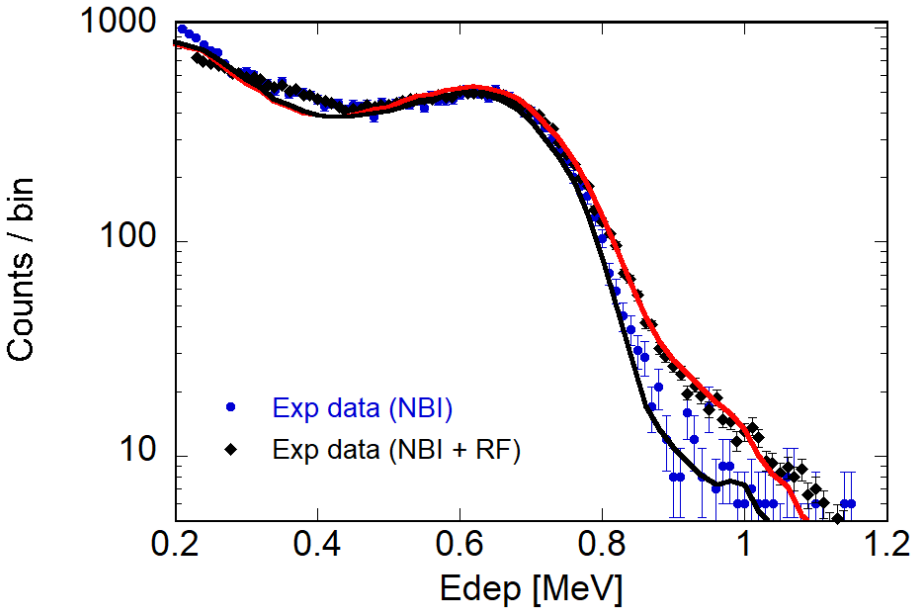

Figure 4.9: Comparison between measured neutron spectra by the VNS diamond matrix with NBI and NBI + RF heating systems and the expected spectra (continuous line) based on TOFOR data analysis.

4.5 High resolution neutron spectroscopy measurements of 14 MeV neutrons

In view of the forthcoming DT JET campaign an accurate calibration of the JET neutron diagnostics with 14 MeV neutrons has been necessary in order to provide a reliable measurement of the fusion power during the next JET deuterium-tritium (DT) campaign. The calibration measurements, to whom I participated, have been performed in the first half of 2017 and consisted in placing a 14 MeV neutron generator of known intensity and energy spectrum at different positions inside the tokamak vessel and recording the signals from the JET neutron diagnostics. The neutron emission intensity was monitored by two absolute calibrated diamond detectors placed on the neutron generator holder (see figure 4.10). In order to achieve an accurate and successfully calibration, the 14 MeV neutron generator (NG) has been previously fully characterized and calibrated at the Neutron Metrology Laboratory of the National Physical Laboratory (NPL, Teddington, UK). The NG was placed in the center of the low scatter area of the laboratory. It was equipped by rotating arms provided by several neutron detectors (liquid scintillator, long counter, activation foils and single crystal diamond detectors) which allowed measuring the intensity and / or the energy spectra emitted by the NG at different angles. 14 MeV neutrons were produced by deuterium-tritium reactions occurring by accelerating

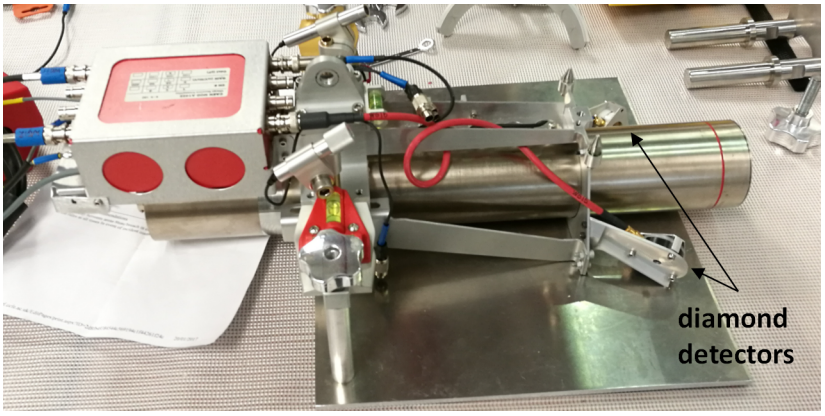

Figure 4.10: Picture of the neutron generator.

the $D_x^+/T_x^+/D_xT_y^+$ beam (nominally 50-50%, x,y=1,2) at a nominally energy of 73 keV onto a titanium target containing T/D (nominally 50-50%) inside a sealed tube. It was observed that D^+, T^+, D_2^+, T_2^+, DT^+, species were present in the beam, resulting in up to six observed different NG neutron energy distributions (see figure 4.11 about the six simulated components). This is due to the different kinetic energy of the species when they reach the T/D target. D^+ and T^+ ions are accelerated by the nominal NG operational voltage. D_2^+ and T_2^+ molecules are accelerated by the same voltage and the individual atoms thus have half of the energy each. Finally, DT^+ ions split into a D^+ and a T^+ ions having 2/5 and 3/5 each of total energy respectively, namely 29.2 keV and 43.8 keV.

As described in detail in [papers VI], high resolution neutron spectroscopy measurements were recorded by using a single crystal diamond detector exploring the neutron energy spectra emitted by the NG at different angles from 0 to 150 degrees (see figure 4.12 in which the x-axis represents the energy deposited in the diamond and the peaks are referred to the n-α reaction channel). As provided by MCNP simulations and confirmed by measurements, the six neutron energy distributions are best separated at zero degrees because of the reaction kinetics, resulting in a broader energy spectrum. By analyzing in detail the neutron energy spectrum emitted at zero degrees, for the first time we demonstrated the capability to accurately determine the detailed ion composition of the beam (see table 4.1). The analysis is based on the numerical fitting of the simulated neutron components resulting from the five ion species convolved with the diamond response function. Figure 4.13 shows the best agreement in terms of reduced chi-square value ($\chi^2 \approx 1.5$) between data and the 5 neutron components weighted by five free parameters which are determined by the fitting process. Here the neutron components due to the reaction D on T at 29.2 keV and T on D at 43.8 keV were added together and considered as a single DT component. The high resolution neutron spectroscopy measurements, together with a detailed analysis, allowed resolving the complex features of the

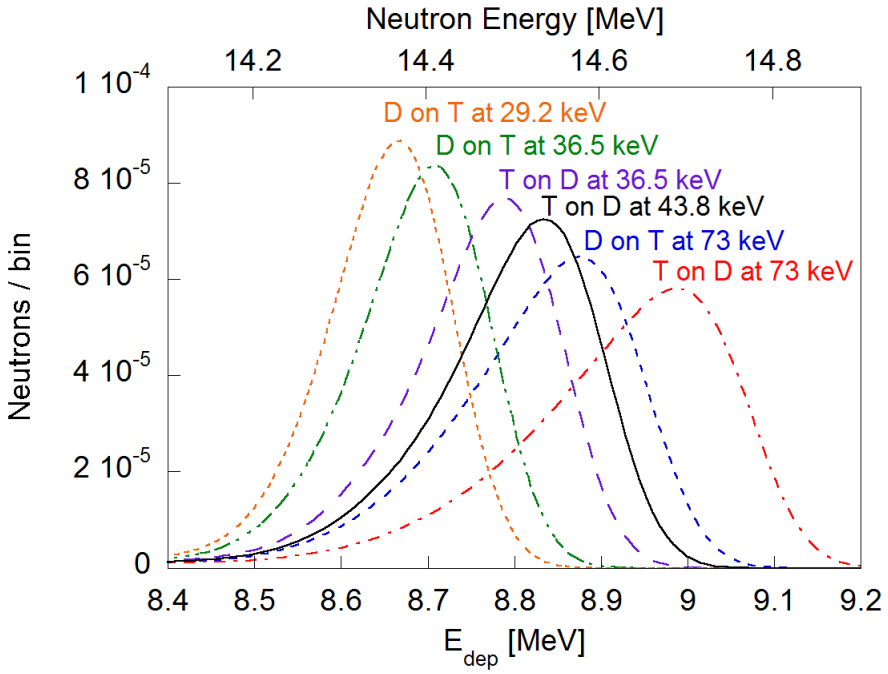

Figure 4.11: Theoretical normalized energy deposited spectra corresponding to each NG neutron emission component and resulting from the MCNP model. The diamond response function of the n-α reaction channel is assumed to be Gaussian-shaped of 120 keV FWHM. The lower x-axis represents the deposited energy inside the detector by neutrons. The upper x-axis represents the energy of the incoming neutrons.

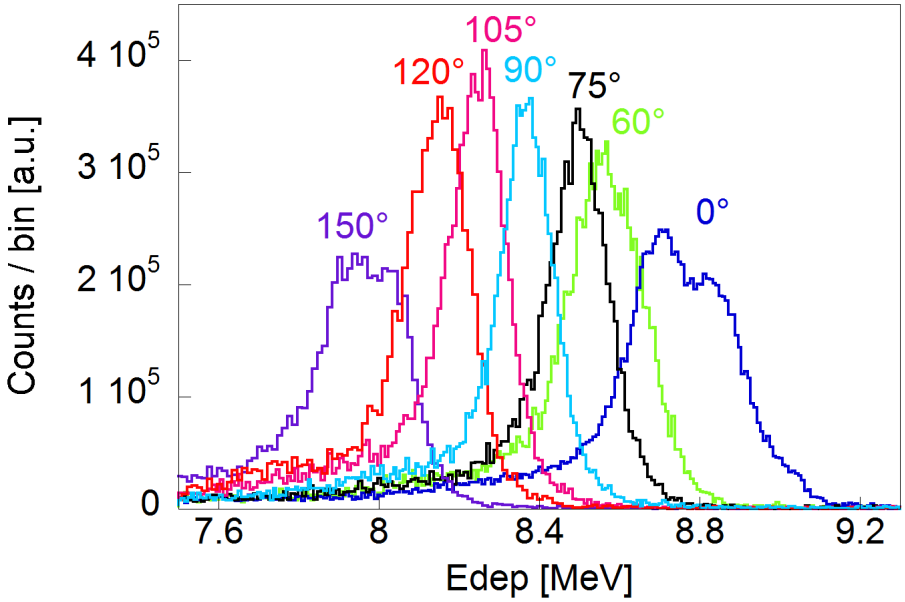

Figure 4.12: Recorded pulse height spectra measured by the SCD at different angles from 0 to 150 degrees. The x-axis represents the deposited energy in the detector and the peaks are due to the n-α reaction channel.

Incident particle beam composition	Concentration [%]
DT^+	80.4±6.1
D_2^+	9±0.9
T_2^+	7.3±2.5
T^+	2.7±0.2
D^+	0.6±0.1

Table 4.1: Summary of the estimated incident particle beam composition derived by the best numerical fit [paper VI].

neutron energy spectra resulting from the mixed D/T beam ions reacting with the T/D nuclei present in the target. This results open up to new prospects for diagnosing DT plasmas on both JET and ITER. The enhanced energy resolution of diamond detectors would allow accurately identifying different neutron components (NBI components, RF components, thermal components) in DT plasma operations and studying non classical phenomena on the beam slowing down for JET and ITER, as shown in [papers V and VI].

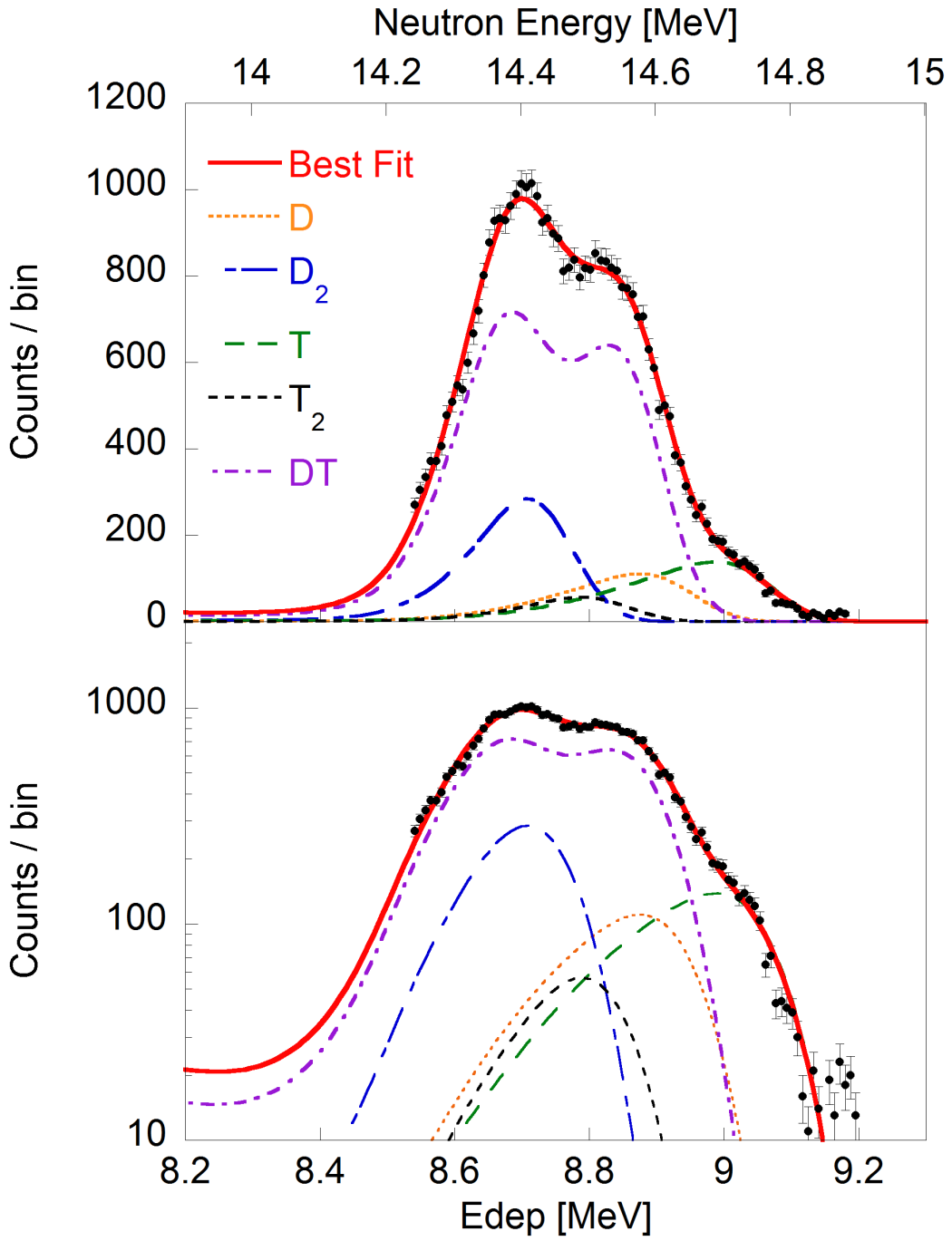

Figure 4.13: Pulse height spectrum recorded at zero degrees by the single crystal diamond detector and shown in linear (top) and logarithmic (bottom) scales . Measured data are shown as black dots without the low energy tail due to partial charge collection. The neutron beam components with their weights and their sum correspond to the best fit to the data. The lower x-axis represents the neutron deposited energy inside the detector while the upper x-axis represents the energy of the incoming neutrons.

4.6 New prospects for diagnosing DT fusion plasmas

From the excellent spectroscopic capabilities achieved with diamond detectors, we extrapolate favorable scenarios for diagnosing DT plasmas. In the second part of manuscripts V and VI we explore the possibility to study the non-classical slowing down of the beam ions in DT plasmas in ITER and JET. This phenomenon was studied by introducing a loss term L(f) in Gaffey's analytical formulas [36] to determine the steady-state distribution function $f_b(v)$ of a beam of neutral ions that slows down in an DT plasma due to Coulomb collisions. The loss term L(f) heuristically describes a non-classical ("anomalous") loss mechanism acting on the beam ions. The loss term L(f) is given by:

$$L(f) = \frac{f_b}{k\tau_s}\left(\frac{v_b}{2v}\right)^{\alpha} = \frac{f_b}{\tau_\alpha(v)}$$

where v_b and τ_s represent the initial velocity and the Spitzer slowing down time, respectively. For $v = v_b/2$, the velocity dependent slowing down time $\tau_\alpha(v)$ is equal to $k \cdot \tau_s$ and the magnitude of k determines the ratio between the classical and anomalous time scales. The exponent α, instead, controls the effect of the anomalous losses on ions at different velocities. The analytical formulas can be solved by standard numerical techniques obtaining the tritons velocity distribution when they are injected with fixed energy and pitch angle into a DT plasma. Consequently a Monte Carlo simulation based on GENESIS code [13] provides the neutron energy spectra viewed from a specific angle for the NBI distribution interacting with the thermal D plasma (beam-thermal component), as well as for the thermal bulk DT plasma component (DT thermal component). The anomalous slowing down of the NBI determines a lower neutron yield and a different spectral shape compared to the classic case. Figure 4.14 shows the beam-thermal neutron components for the 3 cases viewed at 90 degrees resulting by injecting tritons with energy $E_b = 1$ MeV and pitch angle of 0.5 into a ITER DT plasma (with ion and electron temperature of 20 keV and deuterium and tritium density of $1.0 \cdot 10^{20}$ m^{-3}) and the thermal bulk DT plasma component. Here, the latter is shown as dominant contribution since on ITER it is expected to be between 90% and 95% with respect to the NBI one. As shown in [paper VI], we evaluated the response of the high resolution single crystal diamond detectors to these expected neutron distributions. We found that depending on the extent of the anomalous losses (ruled by k and α parameters), there is a measurable change in the neutron spectrum (figure 4.15) which requires a high resolution instrument to fully appreciate the effect. When compared to a poorer neutron detector (energy resolution of 5% at 14 MeV), we find significantly broader spectra with smoother gradients (see figure 4.16). This makes it harder to observe differences among the classical and the anomalous cases and to separate the Thermal and beam-thermal components.

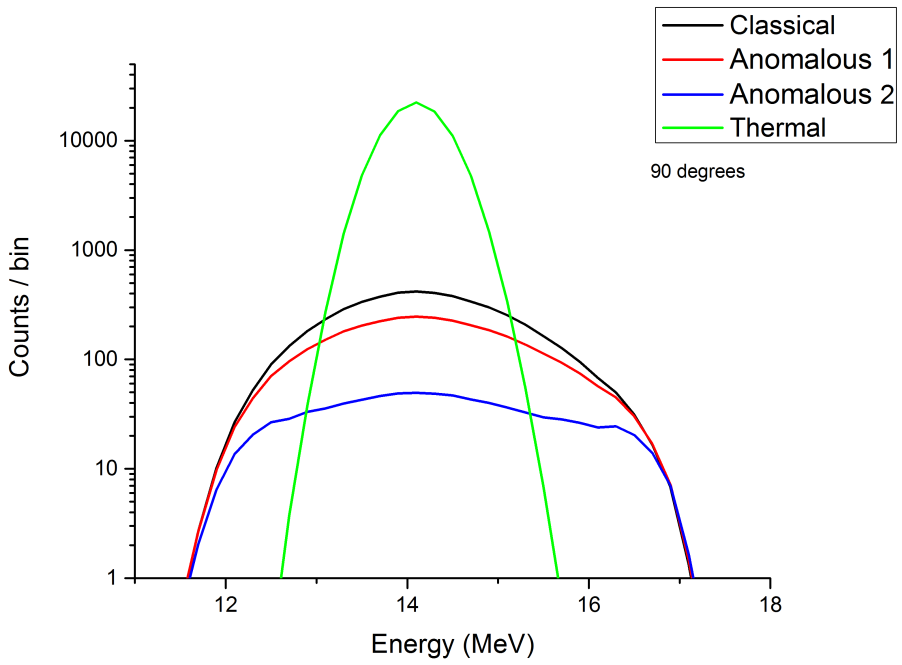

Figure 4.14: Neutron energy spectra (viewed at 90 degrees) calculated by GENESIS code for the ITER case. The neutron energy spectra are generated by the NB tritons interacting with the bulk thermal D (20 keV) plasma for the classical and for two anomalous slowing down cases, together with the neutron energy spectrum emitted by thermal bulk DT plasma at 20 keV.

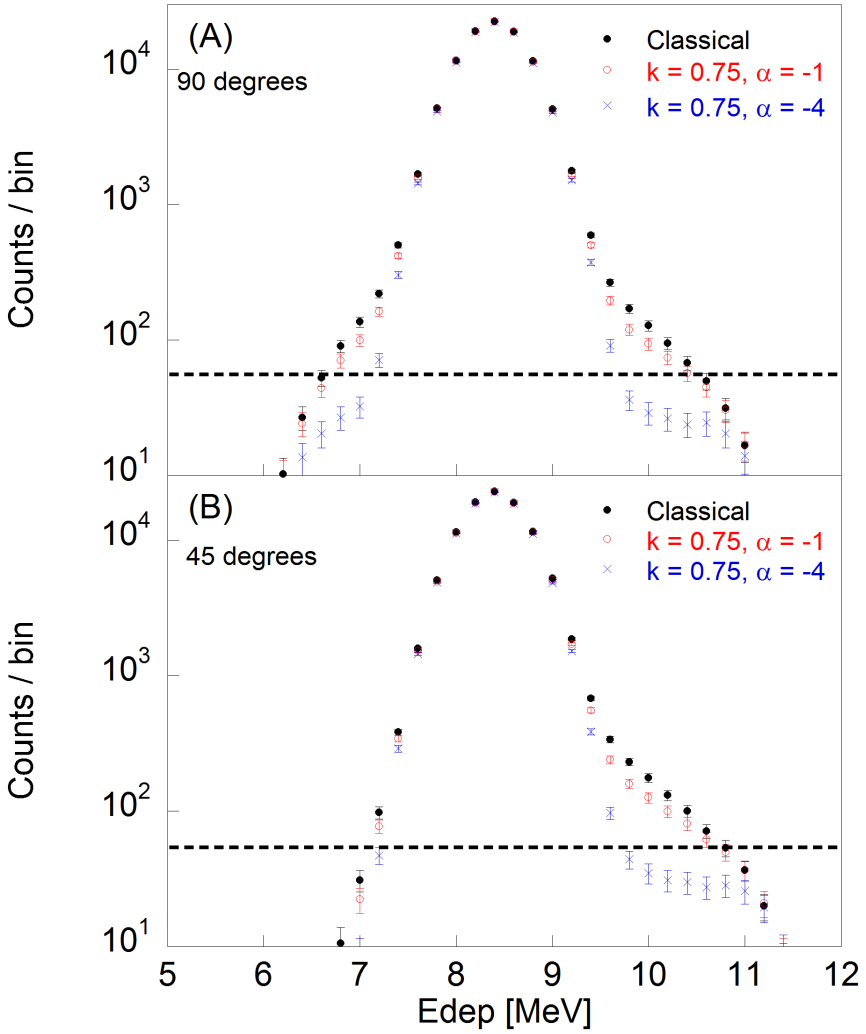

Figure 4.15: Comparison of the neutron spectra in terms of ^{12}C(n,α)^{9}Be peak for the three studied cases after the convolution with diamond response function. The dashed lines represent the level of sensitivity of the diamond detector. Panel (A) and (B) show the neutron spectra viewed at 90 degrees and 45 degrees, respectively. The y-axis of both the graphs is shown in logarithmic scale.

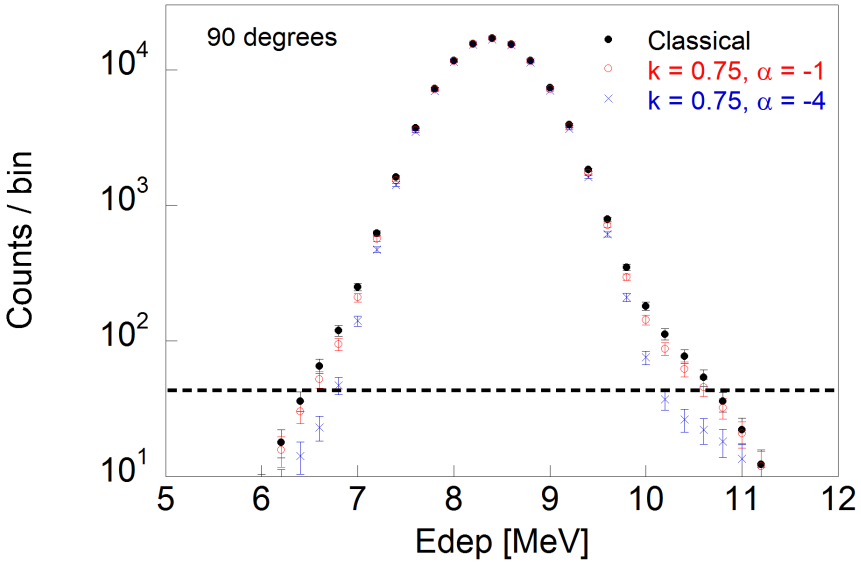

Figure 4.16: Comparison of the neutron spectra viewed at 90 degrees, in terms of $^{12}C(n,\alpha)^{9}Be$ peak for the 3 studied cases after the convolution with a neutron spectrometer with energy resolution equal to 5% at 14 MeV. The dashed line represents the level of sensitivity of the detector. The y-axis is shown in logarithmic scale.

Chapter 5

Conclusions

The estimation and measurement of plasma parameters cover a fundamental role for the understanding of plasma behavior and the optimization of its performances. A burning plasma is a strong source of neutrons and γ-rays which, having no charge, are not affected by magnetic fields of the tokamak and can escape the plasma volume. Neutrons and γ-rays can thus be detected by dedicated diagnostic instruments providing information on fuel and fast ions. Unlike present mid-size tokamaks, where the neutron and γ-rays fluxes are mostly limited and other diagnostics can be preferred, in the next high power devices the neutron and gamma-ray spectroscopy might be the only working fast ion diagnostics. Furthermore, due to the significant increment of neutrons and γ -rays fluxes, neutron and gamma-ray spectroscopy will benefit on ITER and on next high fusion power reactors. Neutrons are directly emitted by fusion reactions carrying information on the fuel ions, allowing the measurement of the ion temperature Ti of the thermal plasma component and to diagnose the supra-thermal components of the fuel ions. Gamma-rays emission in fusion plasmas comes from reactions between fuel nuclei (H, D, T) or fast charged particles (p, d, t, α ,^{3}He) with plasma impurities (such as ^{9}Be and ^{12}C). As mostly demonstrated at the JET, gamma-ray detection can be used to evaluate the behavior of the fusion reaction products as well as of other energetic plasma ions, such as the fusion alpha particles. In view of DT plasmas, of particular interest is the analysis of the Doppler broadened 4.44 MeV gamma-rays emitted from the reactions ^{9}Be(α,nγ)^{12}C through high resolution gamma spectroscopy. Such a measurement would provide qualitative and quantitative information on the energy distribution of α particles which is crucial towards the goal of a reliable commercial reactor. Moreover, by combining this into spatially resolved measurements achieved by an enhanced gamma-ray camera would also provide the spatial distribution of the fusion α particles in a DT plasma and allow studying for example instabilities effects driven by α particles as well as of other fast ions. Due to the harsh environment that characterizes the fusion plasma devices, γ-ray and neutron

spectroscopy become tough and requires dedicated diagnostic systems. The high neutron and gamma-ray fluxes expected at JET in DT plasmas, together with the need to provide time resolution in the range of 10-100 ms, translates into the need of spectrometers capable to operate at counting rates in the MHz range, which poses challenging requirements on the detector capabilities. Moreover, in order to infer detailed information on fast and fuel ions, measurements with high energy resolution are necessary. This poses a further unavoidable requirement on the spectrometer performances. This thesis is focused on the development, characterization and implementation of new compact gamma-ray and neutron spectrometers which combine high counting rate capabilities and very high energy resolution. A prototype compact gamma-ray spectrometer has been developed within an European project which is upgrading the JET gamma ray camera (GC) detectors. The prototype detector is based on a $LaBr_3$ scintillator crystal (25.4 mm diameter, 16.9mm length) coupled to a Silicon PhotoMultiplier (SIPM). The developed prototype spectrometer features an energy resolution of about 5% at 662 keV, which improves for higher energies and provides accurate measurements in the energy range up to a few MeVs. The spectrometer has been designed for operation at counting rates in excess of 1 MCounts/s. For this a suitable shaping circuit of the SIPM signal has been implemented in order to minimize the presence of so called piled up events, which distorts the measurement, allowing operation at counting rates in excess of 1 MCounts/s. The high counting rate capability has been demonstrated up to 3 MCounts/s at an accelerator, by recording the gamma lines produced by the interaction of MeVs protons onto an aluminum target. The 19 new detectors have been successfully calibrated and installed during 2017 in the JET gamma camera and are ready to collect data in the next JET campaigns. The enhanced energy resolution of GC will allow avoiding artifacts in the reconstructed fast ion profile, while the improved time resolution will open the possibility to track for the first time the fast ions profile changes during their slowing down times. On the neutron spectroscopy side, a 12-pixels single crystal diamond matrix has been installed on the vertical line of sight of JET allowing simultaneous measurements of 2.5 MeV and 14 MeV neutrons. The response of diamond neutron spectrometers to 2.5 and 14 MeV neutrons is very different, namely it is dominated by elastic and inelastic scattering for 2.5 MeV neutrons while for 14 MeV neutrons several nuclear reaction channels open up, offering the possibility to perform high resolution spectroscopy. The diamond matrix response function has been measured at nuclear accelerators for incoming different monoenergetic neutron energies, as well as with alpha particles in laboratory at both atmospheric pressure and vacuum. The data validation of the diamond matrix with 2.5 MeV neutrons has been accomplished by comparing with data taken by the reference 2.5 MeV neutron spectrometer at JET, namely TOFOR which shares the same line of sight of the diamond matrix. The results

indicated that the spectrometer works well and can provide a moderated energy resolution in D plasmas. The excellent spectroscopic capabilities of the diamond detectors for 14 MeV neutrons have been studied and explored during the characterization of a 14 MeV DT neutron generator at the National Physical Laboratory. Neutrons were produced by deuterium-tritium reactions occurring by accelerating the $D_x^+/T_x^+/DT^+$ mixed beam (x=1,2) onto a titanium target containing T/D (nominally 50-50%) inside a sealed tube. It was observed that D^+, T^+, D_2^+, T_2^+, DT^+ species were present in the beam resulting in up to six observed different neutron energy distributions. Diamond detectors allowed resolving for the first time the complex features of the neutron energy spectra resulting from the mixed D/T beam ions reacting with the T/D nuclei present in the target. These results open up to new prospects for diagnosing DT plasmas on both JET and ITER. The analysis of the diamond $^{12}C(n,\alpha)^9Be$ peak, in fact, will allow accurately identifying different neutron components (NBI components, RF components, thermal components) in DT plasma operations and studying non classical phenomena on the beam slowing down for JET and ITER. The results presented in this thesis represent a step forward in the development of neutron and gamma-ray spectrometers for fusion plasma diagnostics which combine the MHz counting rate capability with the enhanced energy resolution. The developed instruments feature very compact size and are therefore ideal for integration in a multi line of sight camera on the next step burning plasma fusion devices such as ITER and DEMO.

Bibliography

[1] Jeffrey Freidberg. *Plasma Physics and Fusion Energy*. Cambridge University Press, 2007.

[2] John Wesson. *Tokamaks*. Oxford University Press Inc., 2011.

[3] https://www.euro fusion.org.

[4] John Wesson. The science of JET. Technical report, 2000.

[5] www.iter.org.

[6] D Mazon and et al. As hot as it gets. *Nature Physics*, 12:14–17, 2016.

[7] M Nocente. *Neutron and gamma-ray emission spectroscopy as fast ion diagnostics in fusion plasmas*. PhD thesis, Universita' degli Studi di Milano Bicocca, 2011.

[8] M Tardocchi, M Nocente, and G Gorini. Diagnosis of physical parameters of fast particles in high power fusion plasmas with high resolution neutron and gamma-ray spectroscopy. *Plasma Phys. Control. Fusion*, 55(074014), 2013.

[9] W R Faust and E G Harris. Energy distribution of neutrons produced by a thermonuclear reaction. *Nucl. Fusion*, 1(62), 1960.

[10] M Tardocchi. *Neutron emission spectroscopy studies of fusion plasmas of deuterium-tritium in tokamaks*. PhD thesis, Uppsala University, 2000.

[11] V G Kiptily and et al. Gamma ray diagnostics of high temperature magnetically confined fusion plasmas. *Plasma Phys. Control. Fusion*, 48:R59–R82, 2006. doi: 10.1088/0741-3335/48/8/R01.

[12] I N Chugunov and et al. Development of gamma-ray diagnostics for ITER. *Nucl. Fusion*, 51(083010), 2011.

[13] M Tardocchi and et al. Spectral broadening of characteristic gamma-ray emission peaks from ^{12}C(^{3}He; pγ)^{14}N reactions in fusion plasmas. *Phys. Rev. Lett.*, 107 (205002), 2011.

[14] M Nocente and et al. Energy resolution of gamma-ray spectroscopy of JET plasmas with a LaBr3 scintillator detector and digital data acquisition. *Review of Scientific Instruments*, 81(10D321), 2010. doi: 10.1063/1.3501386.

[15] S J Zweben and et al. Alpha-particle physics in the tokamak fusion test reactor DT experiment. *Plasma Physics and Controlled Fusion*, 39(5A), 1997.

[16] A Fasoli, C Gormenzano, HL Berk, B Breizman, S Briguglio, DS Darrow, N Gorelenkov, WW Heidbrink, Andre Jaun, SV Konovalov, et al. Physics of energetic ions. *Nuclear Fusion*, 47:S264–S284, 2007.

[17] M Nocente and et al. High-resolution gamma ray spectroscopy measurements of the fast ion energy distribution in JET ^{4}He plasmas. *Nuclear Fusion*, 52(063009), apr 2012. doi: 10.1088/0029-5515/52/6/063009.

[18] A Ghassemi, K Sato, and K Kobayashi. Technical note mppc. cat. no. kapd9005e01 mar. 2017. Technical report. URL `http://www.hamamatsu.com`.

[19] http://tukan.ncbj.gov.pl.

[20] *MPPC (Multi-Pixel Photon Counter) arrays S13361-3050 series, Hamamatsu datasheet.* URL `https://www.hamamatsu.com`.

[21] V Perseo. Development of gamma ray spectroscopy camera for fusion plasmas. Master's thesis, Universita' degli Studi di Milano Bicocca, 2016.

[22] http://mcnpx.lanl.gov/.

[23] M Nocente. Report on deliverable D04 - Simulation of expected gamma-ray emission spectra at the detector position. Technical report, 2015.

[24] http://www.caen.it.

[25] G F Knoll. *Radiation Detection and Measurement, 4th ed.* Wiley, 2010.

[26] I Lengar and S Conroy. Final report on m17: Simulation of neutron (background) and gamma-ray transport to the detector positions. Technical report, 2017.

[27] M Nocente and et al. High resolution gamma ray spectroscopy at MHz counting rates with LaBr3 scintillators for fusion plasma applications. *IEEE Trans. Nucl. Sci.*, 60 (1408), 2013.

[28] C Cazzaniga and et al. Single crystal diamond detector measurements of deuterium-deuterium and deuteriumtritium neutrons in Joint European Torus fusion plasmas. *Rev. Sci. Instrum*, 85(043506), 2014.

[29] https://www.e6.com.

[30] https://cividec.at/.

[31] C Hellesen and et al. Measurements of fast ions and their interactions with MHD activity using neutron emission spectroscopy. *Nucl. Fusion*, 50(084006), 2010.

[32] M Pillon and et al. Experimental response functions of a single-crystal diamond detector for 5-20.5 MeV neutrons. *Nuclear Instruments and Methods in Physics Research A*, 640:185–191, 2011.

[33] D. Schlegel. *Target User Manual, PTB-6.42-05-2.* PTB, Braunschweig, 2005.

[34] A Muraro and et al. First neutron spectroscopy measurements with a pixelated diamond detector at JET. *Rev. Sci. Instrum.*, 87(11D833), 2016.

[35] M Rebai and et al. Response function of single crystal synthetic diamond detectors to 1-4 MeV neutrons for spectroscopy of D plasmas. *Rev. Sci. Instrum.*, 87(11D823), 2016. doi: 10.1063/1.4960490.

[36] J D Gaffey. *J. Plasma Phys.*, 16(2):149–169, 1976.

Synopsis of attached papers

The abstracts of the papers attached to this thesis have been collected in this section.

I. **Performance of the prototype LaBr3 spectrometer developed for the JET gamma-ray camera upgrade**

In this work, we describe the solution developed by the gamma ray camera upgrade enhancement project to improve the spectroscopic properties of the existing JET γ-ray camera. Aim of the project is to enable gamma-ray spectroscopy in JET deuterium-tritium plasmas. A dedicated pilot spectrometer based on a LaBr3 crystal coupled to a silicon photo-multiplier has been developed. A proper pole zero cancellation network able to shorten the output signal to a length of 120 ns has been implemented allowing for spectroscopy at MHz count rates. The system has been characterized in the laboratory and shows an energy resolution of 5.5% at Eγ = 0.662 MeV, which extrapolates favorably in the energy range of interest for gamma-ray emission from fast ions in fusion plasmas.

II. **Gamma-ray spectroscopy at MHz counting rates with a compact LaBr3 detector and silicon photomultipliers for fusion plasma applications**

Gamma-ray spectroscopy measurements at MHz counting rates have been carried out, for the first time, with a compact spectrometer based on a LaBr3 scintillator and silicon photomultipliers. The instrument, which is also insensitive to magnetic fields, has been developed in view of the upgrade of the gamma-ray camera diagnostic for α particle measurements in deuterium-tritium plasmas of the Joint European Torus. Spectra were measured up to 2.9 MHz with a projected energy resolution of 3%-4% in the 3-5 MeV range, of interest for fast ion physics studies in fusion plasmas. The results reported here pave the way to first time measurements of the confined α particle profile in high power plasmas of the next deuterium-tritium campaign at the Joint European Torus.

III. **Characterization of a compact LaBr3(Ce) detector with Silicon photomultipliers at high 14 MeV neutron fluxes**

A new compact gamma-ray spectrometer based on a Silicon Photo-Multiplier (SiPM) coupled to a LaBr3(Ce) crystal has been developed for the upgrade of the Gamma Camera (GC) of JET, where it must operate in a high intensity neutron/gamma-ray admixed field. The work presents the results of an experiment aimed at characterizing the effect of 14 MeV neutron irradiation on both LaBr3(Ce) and SiPM that compose the full detector. The pulse height spectrum from neutron interactions with the crystal has been measured and is successfully reproduced by MCNP simulations. It is calculated that about 8% of the impinging neutrons leave a detectable signal of which less than $<$ 4% of the events occur in the energy region above 3 MeV, which is of interest for gamma-ray spectroscopy applications. Neutron irradiation also partly degrades the performance of the SiPM and this is mostly manifested as an increase of the dark current versus the neutron fluence. However, it was found that the SiPM can be still operated up to a fluence of 4 1010 n/cm2, which is the highest value we experimentally tested. Implications of these results for GC measurements at JET are discussed.

IV. **Capabilities of a Diamond Detector matrix for neutron spectroscopy measurements at JET**

Single-crystal Diamond Detectors (SDDs) feature high radiation hardness, fast response and compact size. This makes SDDs ideal candidates for fast neutron detectors in environment where high neutron flux is an issue such as the next generation burning plasmas experiments. Neutron detection in SDD is based on the collection of electron-hole pairs produced by charged particles generated by neutron interaction with 12C nuclei. For neutron energies above about 7 MeV neutron spectroscopy is possible by measuring the deposited energy into the detector via the reaction 12C(n,)9Be. This is indeed the cases of SDD measurements of 14 MeV neutrons of DT plasmas. A single pixel SDD (4.5x4.5x0.5 mm^3) prototype was installed at JET in 2013 and the achieved results allowed to assess also the neutron spectroscopic capability of deuterium plasmas. A 12-pixels SDD matrix has been recently realized and will be installed in 2015 at JET for DT plasmas as part of the Vertical Neutron Spectrometer project. In this paper calibration of the SDD matrix with alpha particles in the laboratory and 14 MeV neutrons performed at the ENEA Frascati Neutron Generator will be presented. These calibrations have been performed with a fast charge preamplifier combined to a fast digital

data acquisition, which allows for neutron spectroscopy measurements with simultaneously high energy resolution and high count rate capability. Both requirements are essential for neutron spectroscopy of high power fusion plasmas. The calibrations results achieved extrapolate favorably in view of future neutron spectroscopy measurements at JET using diamond detectors.

V. **Neutron emission spectroscopy of DT plasmas at enhanced energy resolution with diamond detectors**

This work presents measurements done at the Peking University Van de Graaff neutron source of the response of single crystal synthetic diamond (SD) detectors to quasi-monoenergetic neutrons of 14-20 MeV. The results show an energy resolution of 1% for incoming 20 MeV neutrons, which, together with 1% detection efficiency, opens up to new prospects for fast ion physics studies in high performance nuclear fusion devices such as SD neutron spectrometry of deuterium-tritium plasmas heated by neutral beam injection.

VI. **Neutron spectroscopy measurements of 14 MeV neutrons at unprecedented energy resolution and implications for deuterium-tritium fusion plasma diagnostics**

An accurate calibration of the JET neutron diagnostics with a 14 MeV neutron generator was performed in the first half of 2017 in order to provide a reliable measurement of the fusion power during the next JET deuterium-tritium (DT) campaign. In order to meet the target accuracy, the chosen neutron generator has been fully characterized at the Neutron Metrology Laboratory of the National Physical Laboratory (NPL), Teddington-UK. The present paper describes the measurement of the neutron energy spectra obtained by using a high resolution single-crystal diamond detector (SCD). The measurements, together with a new neutron source routine "ad hoc" developed for the MCNP code, allowed the complex features of the neutron energy spectra resulting from the mixed D/T beam ions interacting with the T/D target nuclei to be resolved for the first time. From the spectral analysis a quantitative estimation of the beam ion composition has been made. The unprecedented intrinsic energy resolution (<1% FWHM at 14 MeV) of diamond detectors opens up new prospects for diagnosing DT plasmas, such as, for instance, the possibility to study non-classical slowing down of the beam ions by neutron spectroscopy on ITER.

Paper I

Performance of the prototype $LaBr_3$ spectrometer developed for the JET gamma-ray camera upgrade

D. Rigamonti,[1,2,a)] A. Muraro,[2] M. Nocente,[1,2] V. Perseo,[1] G. Boltruczyk,[3] A. Fernandes,[4] J. Figueiredo,[4,5] L. Giacomelli,[2] G. Gorini,[1,2] M. Gosk,[3] V. Kiptily,[6] S. Korolczuk,[3] S. Mianowski,[3] A. Murari,[5,7] R. C. Pereira,[4] E. P. Cippo,[2] I. Zychor,[3] M. Tardocchi,[2] and JET Contributors[8,b)]

[1]*Dipartimento di Fisica "G. Occhialini," Università degli Studi di Milano-Bicocca, Milano, Italy*
[2]*Istituto di Fisica del Plasma "P. Caldirola," CNR, Milano, Italy*
[3]*Narodowe Centrum Badań Jądrowych (NCBJ), 05-400 Otwock-Swierk, Poland*
[4]*Instituto de Plasmas e Fusão Nuclear, Instituto Superior Técnico, Universidade de Lisboa, Lisboa, Portugal*
[5]*EUROfusion Programme Management Unit, Culham Science Centre, OX14 3DB Abingdon, United Kingdom*
[6]*Culham Science Centre for Fusion Energy, Culham, United Kingdom*
[7]*Consorzio RFX (CNR, ENEA, INFN, Universita' di Padova, Acciaierie Venete SpA), Padova, Italy*
[8]*EUROfusion Consortium, JET, Culham Science Centre, Abingdon OX14 3DB, United Kingdom*

(Presented 9 June 2016; received 6 June 2016; accepted 18 July 2016; published online 23 August 2016)

In this work, we describe the solution developed by the gamma ray camera upgrade enhancement project to improve the spectroscopic properties of the existing JET γ-ray camera. Aim of the project is to enable gamma-ray spectroscopy in JET deuterium-tritium plasmas. A dedicated pilot spectrometer based on a $LaBr_3$ crystal coupled to a silicon photo-multiplier has been developed. A proper pole zero cancellation network able to shorten the output signal to a length of 120 ns has been implemented allowing for spectroscopy at MHz count rates. The system has been characterized in the laboratory and shows an energy resolution of 5.5% at $E_\gamma = 0.662$ MeV, which extrapolates favorably in the energy range of interest for gamma-ray emission from fast ions in fusion plasmas. [http://dx.doi.org/10.1063/1.4961060]

I. INTRODUCTION

Gamma-ray spectroscopy is a plasma diagnostic technique which can investigate the behaviour of fast ions in high temperature fusion plasmas, as demonstrated at JET.[1–6] In particular, it plays a key role in the study of alpha particle confinement, which is crucial for plasma self-heating in a high power discharge. Gamma-ray emission in thermonuclear plasmas is mainly due to reactions between fast particles and fuel ions or impurities. Of particular relevance is the detection of 4.44 MeV gamma-rays from the $^9Be(\alpha, n\gamma)^{12}C$ reaction, as it gives information on alpha particles in deuterium-tritium plasmas. At JET, a horizontal and a vertical neutron/γ camera[7] provide information on the radial profile of the neutron/γ emission source by collimated measurements along 19 channels. The gamma-ray camera upgrade project aims to improve the spectroscopic properties of the existing γ-ray camera of JET in terms of energy resolution and high counting rate capability, in order to operate in the deuterium-tritium (DT) campaign. This requires a rather significant improvement of the existing CsI detector performance, in order to reach an energy resolution of 5% (Energy Resolution = FWHM/E_n) at 1.1 MeV and count rate capability in excess of 500 kHz. An important constraint is the limited available space which, for example, makes it impossible to use photo-multiplier tubes. The use of fast, high light yield inorganic scintillators such as $LaBr_3$[8] together with Silicon Photo-Multipliers (SiPMs) can represent a good alternative to the existing CsI and photodiodes, given their high photon detection efficiency, high internal gain, insensitivity to magnetic field, and an extremely compact size. SiPMs, which have experienced great improvements in the last years, still show voltage-temperature dependence[9] and a limited linearity but both issues can be corrected for.[9] In this work, we describe the solution developed to meet the requirements. This combines the good energy resolution results achieved by Grodzicka *et al.*[10] and the promising counting rate capability reached by Nocente *et al.*[11] The pilot detector is based on a $LaBr_3$ scintillator crystal (25.4×16.9 mm^2) coupled to a silicon photo-multiplier (12×12 mm^2, see Fig. 1). The final design with the electronic readout circuit of the pilot spectrometer will be presented together with the laboratory measurements at low count rate with radiation sources and at high count rate with a LED pulser.

II. SILICON PHOTO-MULTIPLIER AND ELECTRONIC READOUT CIRCUIT

Silicon photo-multiplier detectors, also known as Multi-Pixel Photon Counters (MPPCs), are relatively novel solid state photo-sensors. They are made up of multiple Avalanche Photo-Diode (APD) pixels connected in parallel and operating

Note: Contributed paper, published as part of the Proceedings of the 21st Topical Conference on High-Temperature Plasma Diagnostics, Madison, Wisconsin, USA, June 2016.

a)Author to whom correspondence should be addressed. Electronic mail: davide.rigamonti@mib.infn.it

b)See the Appendix of F. Romanelli *et al.*, Proceedings of the 25th IAEA Fusion Energy Conference, Saint Petersburg, Russia, 2014.

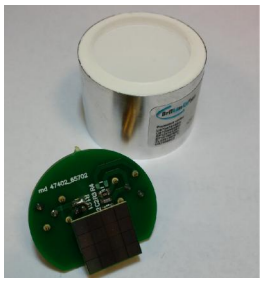

FIG. 1. $LaBr_3$ scintillator crystal and silicon photo-multiplier with its read-out circuit board.

in Geiger mode which provide an internal high gain of the order of 10^6, depending on the operational condition. For each APD cell, the Geiger mode is activated when a reversed bias above the electrical breakdown voltage (V_{bd}) is applied. The chosen SiPMs are 12×12 mm^2 in size, made by 16 channels with 3464 pixels each, and they are manufactured by Hamamatsu, model S12642-0404PB-50. Large area/high pixelization MPPCs are needed in order to match the scintillator size and for photon counting in the multi MeV energy range. The characteristic I-V curve of the device shows a steep increase of the current at the breakdown voltage, which is roughly 65 V. In order to achieve high counting rate capability, a short output signal is necessary to minimize the fraction of pile up events. For this purpose, the dedicated electronic circuit suggested in Nocente's article[11] has been developed by implementing a CR differentiator circuit on the MPPC readout board of Fig. 1. Fig. 2 shows an example of a signal from a standard ^{137}Cs radioactive source after the CR differentiator. A signal width of 120 ns has been achieved without a significant loss of the amplitude (about 60 mV at the 662 keV full peak from ^{137}Cs). This is an improvement with respect to what was done in Ref. 11 since the MPPC signal output can be fed directly in the ADC without the need for further amplification.

III. LABORATORY TEST AT LOW COUNTING RATE

A. Measured spectra and energy resolution

Laboratory measurements with standard radioactive sources have been performed in order to characterize the MPPC response and its dedicated electronic readout circuit. The MPPC was coupled with a LaBr3 scintillator crystal (25.4×16.9 mm^2) and powered with a bias voltage of 65.2 V–67.5 V provided by a TTi EX752M voltage supply. Optical grease and an aluminum foil were used to improve light collection from the scintillator. The output signal from the detector was fed into a waveform digitizer CAEN module DT5730 (14 bit, 500 Msps) equipped with CAEN software able to perform on-line measurements of the pulse area. In order to characterize the pilot spectrometer, several measurements have been performed at different bias voltage, revealing an improvement in the energy resolution by increasing the applied voltage up to 67.5 V. Example of calibrated pulse height spectrum with ^{137}Cs (E_γ = 662 keV) and ^{60}Co (E_γ = 1173 and 1333 keV) radioactive sources at V_{bias} = 67.2 V (roughly 2.3 V over V_{bd}) is shown in Fig. 3. The peaks of the spectrum were fitted by a Gaussian function on a background described by polynomials. An energy resolution (Energy Resolution = FWHM/Energy) of 5.5% was obtained at 662 keV which improves to 3.7% for 1333 keV gamma rays. The trend of the energy resolution (see Fig. 4) is well fitted by the curve[12] $f(E) = (a/\sqrt{(E)} + b/E)$ which extrapolates favorably in the energy range of interest (<2.5% in the range 3–5 MeV) for the observation of 4.44 MeV gamma-rays from the ^{9}Be$(\alpha, n\gamma)^{12}$C reaction at kHz counting rates. The

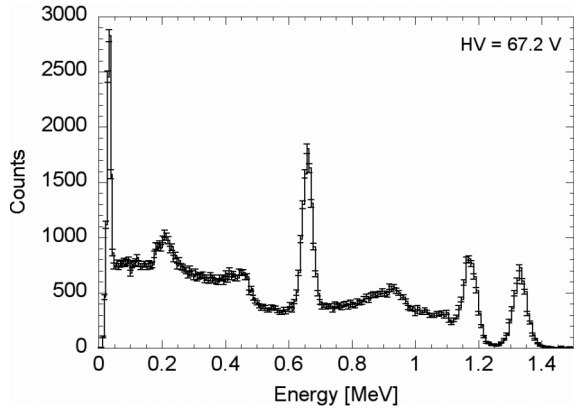

FIG. 3. Pulse height spectrum recorded with ^{137}Cs and ^{60}Co sources. Non-linear calibration has been applied to generate the x-axis.

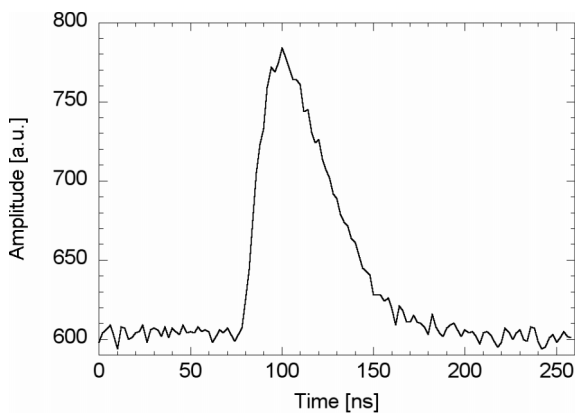

FIG. 2. Output signal from the $LaBr_3$ crystal coupled to the SiPM with the pole zero cancellation network.

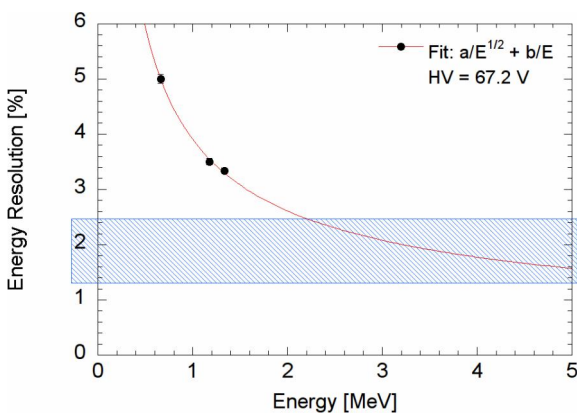

FIG. 4. Measured energy resolution as function of the energy. Error bars are of the same magnitude of the black dots.

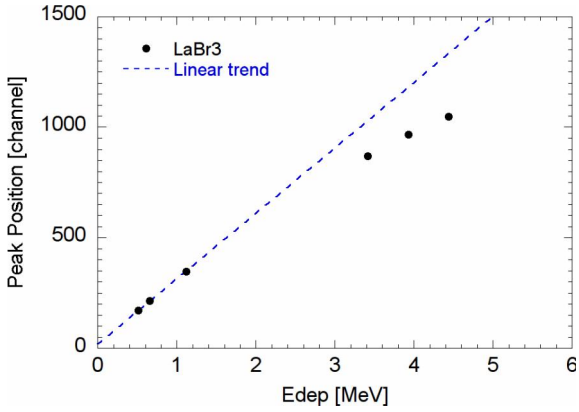

FIG. 5. Linearity of the MPPC. Linear trend has been extrapolated by fitting first two points corresponding to energies 0.511 MeV and 0.662 MeV, respectively. Error bars are of the same magnitude of the black dots.

limited linearity of the SiPM has been investigated at the National Centre for Nuclear Research (NCBJ, Poland) mainly by measuring the 4.44 MeV gamma rays emitted by a PuBe source and that resulted in three peaks in the pulse height spectrum: a full energy peak (4.438 MeV), a single escape peak (3.927 MeV), and a double escape peak (3.416 MeV). Among the other sources we used are ^{137}Cs and ^{65}Zn (E_γ = 1.116 MeV). Measurements have been performed in a climate chamber at stable temperature to prevent peak shifts due to temperature changes. Results (see Fig. 5) indicate that there is a nonlinear relation between the channel position and the gamma-ray energy, but this is of the order of 20% at 4.5 MeV and can be easily corrected for.

B. Comparison with a standard photo-multiplier tube

A comparison in terms of energy resolution with a conventional Photo-Multiplier Tube (PMT), manufactured by Hamamatsu (model R9420-100-10), was done. In order to reduce the effect of the geometric efficiency, an aluminum mask with a hole of the same size as the MPPC has been used to cover the PMT surface coupled to the $LaBr_3$ crystal. In this way, the only small difference in the collecting area between the PMT and the MPPC was due to the geometrical Fill Factor (FF) of the MPPC itself, which is the ratio of the effective photosensitive area to total area.[13] Results show that energy resolution values of the MPPC operating in the optimal condition are comparable within few fractions of % to those with a PMT having the same collecting area (see Table I). These values are also close to those expected from the statistical fluctuation of the number of photoelectrons generated at each energy and that can be estimated at each energy (see the column labelled as "Calculated").[14]

TABLE I. Comparison between the energy resolution of the PMT covered with the aluminum mask and the one of the MPPC. The calculated energy resolution is the one expected from the statistical fluctuation of the number of photoelectrons generated.

Peak energy (keV)	Measured energy resolution (%)	Calculated (%)
PMT with mask (collecting area 12×12 mm^2)		
662	4.7	4.1
1173	3.8	3.1
1333	3.4	2.9
MPPC 12×12 mm^2		
662	5.5	5.0
1173	4.0	3.8
1333	3.7	3.6

IV. LABORATORY TESTS AT HIGH COUNTING RATE WITH A LED PULSE

A. Measurements with LED pulse

In order to simulate the high rate environment expected at JET, a mock up of high counting rate measurements[15] has been performed in the laboratory by using a blue LED powered by Keysight (model 81150A) pulse generator. With this setup, we were able to illuminate the MPPC with blue light at a chosen intensity and at increasing counting rates up to about 1 MHz. A ^{137}Cs source was then placed close to the $LaBr_3$ crystal and used to monitor the effect of the LED light (perturbation) on the position and energy resolution of the corresponding full peak at 662 keV from ^{137}Cs. We have observed that the mean position of the ^{137}Cs progressively drifted as the counting rate from the blue LED was increased. This effect was mainly caused by the voltage drop across a resistor placed between the power supply and the MPPC and can be easily reduced by decreasing the value of this resistor, without any appreciable effect on other detector parameters. The peak shift was then observed to increase at higher MPPC bias voltages and at larger intensities of LED perturbation source. Both parameters control the current that flows in the device and that is increased at higher intensities and rates, resulting in an augmented drop on the input resistor. Several measurements allowed investigating and reducing the shift of the peak position in the pulse height spectrum due to the high counting rate. By selecting a sufficiently low resistance (10 Ω) as input, we were able to reduce the shift to 5% at the ^{137}Cs peak, when the LED was operated at 500 kHz and with an equivalent energy of 2 MeV. Part of the contribution to this shift may also come from local heating of the MPPC induced by the larger signal current, as we did not perform our tests in a climatic chamber. This second contribution can however be reduced by adjusting the MPPC gain with a temperature feedback sensor.[9]

Dedicated tests at counting rates up to few MHz were also successfully performed by using reactions emitting gamma-rays at nuclear accelerators and in a condition that closely mirrored the radiation load expected from deuterium-tritium plasma at full power at JET. The experimental setup and results of these measurements are addressed in Nocente's article.[16]

B. JET-like measurements

In order to investigate the behavior of the pilot spectrometer during a JET discharge, a 60 s measurement with two LED pulses has been performed. A LED pulse was used as reference pulse with fix amplitude (corresponding to 3 MeV gamma rays) and fixed repetition rate (10 kHz). The second one, corresponding to a gamma ray of 662 keV, worked as

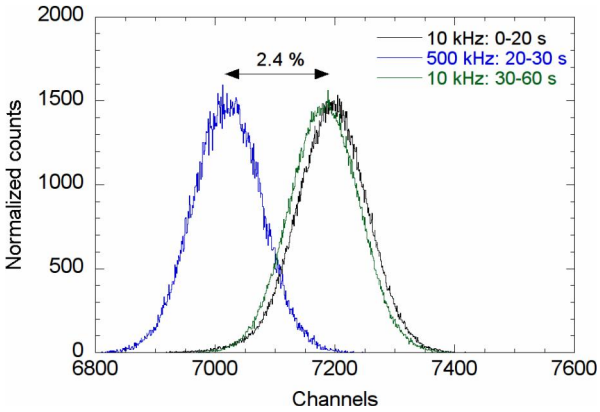

FIG. 6. JET-like measurement with a perturbation window of 10 s at high counting rate.

perturbation source in a temporal window of 10 s in which its repetition rate was ramped up to 500 kHz in order to simulate the experimental conditions of a JET shot. The recorded spectrum has been analyzed by sampling the measurement in temporal windows before, during, and after the high rate flux. Results, shown in Fig. 6, highlight a modest shift of 2.4% obtained, thanks to the previous evaluations on the input resistor. We can also assert that this shift can be judged acceptable.

V. $LaBr_3$ INTRINSIC RADIOACTIVITY AS GAIN MONITOR SYSTEM

Due to spatial and cabling constraints, a gain monitor system based on a LED fiber optics cannot be installed on each detector of the gamma ray camera at JET. However, the intrinsic radioactivity of the $LaBr_3$ crystal can be in principle used as a gain monitor to verify the detector stability.[12] Fig. 7 shows a spectrum of the detector intrinsic radioactivity integrated over 20 min, which is the average time in between two JET discharges. A clear peak at 1.47 MeV is observed and can be used to monitor peak shifts of few % from one discharge to the next one. Here we also note that the natural

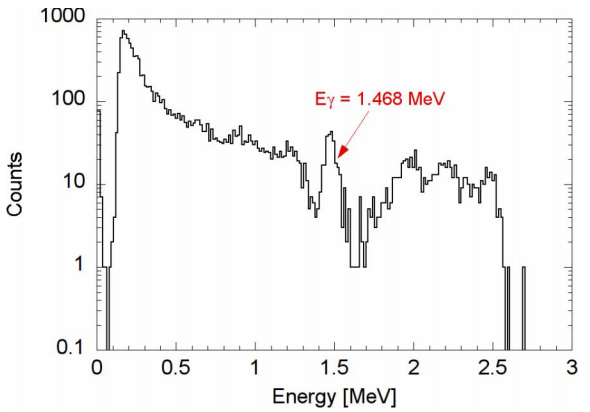

FIG. 7. Intrinsic activity spectrum of a 25.4×16.9 mm^2 $LaBr_3$ crystal collected in 20 min of measurement. The x-axis has been generated with the nonlinear calibration.

radioactivity of $LaBr_3$ does not interfere with peaks expected from fast ions in the plasma ($E > 3$ MeV), as it does not extend above 2.6 MeV.

VI. CONCLUSIONS

A dedicated pilot spectrometer based on a LaBr3 scintillator crystal (25.4×16.9 mm^2) coupled to a Silicon Photo-Multiplier (SiPM) (12×12 mm^2) has been developed in order to meet the requirements needed for the gamma camera upgrade project. A read-out electronic circuit has been built by implementing a proper CR differentiator able to shorten the output signal width down to 120 ns, allowing for gamma-ray spectroscopy at MHz counting rates and good energy resolution. Laboratory measurements with standard radioactive sources show an energy resolution of about 5.5% at 662 keV at the bias voltage of 67.2 V which extrapolates to <2.5% in the range of interest for plasma diagnostics (3-5 MeV). Mock up measurements at high count rate with LEDs revealed a peak shift in the measured spectra, which has however been minimized by choosing a sufficiently small input resistor for the readout board. The intrinsic radioactivity of the $LaBr_3$ crystal can be used to monitor gain changes in between shots. The overall performance of the system is significantly better than that of CsI detectors of the present gamma ray camera and will allow for improved measurements of the γ-ray emission profile in fast ion experiments of the next JET campaigns and, later on, in high performance deuterium-tritium plasmas.

ACKNOWLEDGMENTS

This work has been carried out within the framework of the EUROfusion Consortium and has received funding from the Euratom research and training programme 2014-2018 under Grant Agreement No. 633053. The views and opinions expressed herein do not necessarily reflect those of the European Commission.

[1]V. G. Kiptily *et al.*, Nucl. Fusion **42**, 999–1007 (2002).
[2]M. Nocente *et al.*, Nucl. Fusion **52**, 063009 (2012).
[3]M. Nocente *et al.*, Nucl. Fusion **52**, 094021 (2012).
[4]M. Tardocchi, M. Nocente, and G. Gorini, Plasma Phys. Controlled Fusion **55**, 074014 (2013).
[5]M. Tardocchi *et al.*, Phys. Rev. Lett. **107**, 205002 (2011).
[6]J. Eriksson *et al.*, Nucl. Fusion **55**, 123026 (2015).
[7]V. Kiptily, F. E. Cecil, and S. S. Medley, Plasma Phys. Controlled Fusion **48**, R59 (2006).
[8]M. Nocente *et al.*, IEEE Trans. Nucl. Sci. **60**, 1408 (2013).
[9]I. Zychor *et al.*, Phys. Scr. **91**, 064003 (2016).
[10]M. Grodzicka, M. Moszyński, T. Szczęśniak, M. Szawłowski, D. Wolski, and J. Baszak, "MPPC array in the readout of CsI:Tl, LSO:Ce:Ca, LaBr:Ce, and BGO scintillators," IEEE Trans. Nucl. Sci. **59**(6), 3294 (2012).
[11]M. Nocente *et al.*, Rev. Sci. Instrum. **85**, 11E108 (2014).
[12]G. F. Knoll, *Radiation Detection and Measurement*, 4th ed. (Wiley, 2010).
[13]See http://www.hamamatsu.com for details on the MPPCs.
[14]V. Perseo, "Development of gamma ray spectroscopy camera for fusion plasma," Master thesis, University of Milano Bicocca, 2016.
[15]M. Tardocchi *et al.*, Rev. Sci. Instrum. **79**, 10E524 (2008).
[16]M. Nocente *et al.*, Rev. Sci. Instrum. **87**, 11E714 (2016).

Paper II

Gamma-ray spectroscopy at MHz counting rates with a compact $LaBr_3$ detector and silicon photomultipliers for fusion plasma applications

M. Nocente,[1,2,3,a)] D. Rigamonti,[2,3] V. Perseo,[2] M. Tardocchi,[3] G. Boltruczyk,[4] A. Broslawski,[4] A. Cremona,[3] G. Croci,[2,3] M. Gosk,[4] V. Kiptily,[5] S. Korolczuk,[4] M. Mazzocco,[6] A. Muraro,[3] E. Strano,[6] I. Zychor,[4] G. Gorini,[2,3] and JET Contributors[1,b)]

[1]*EUROfusion Consortium, JET, Culham Science Centre, Abingdon, United Kingdom*
[2]*Dipartimento di Fisica, Università di Milano-Bicocca, Milano, Italy*
[3]*Istituto di Fisica del Plasma "Piero Caldirola," Milano, Italy*
[4]*Narodowe Centrum Badan Jadrowych (NCBJ), Otwock-Swierk, Poland*
[5]*Culham Centre for Fusion Energy, Culham, United Kingdom*
[6]*Dipartimento di Fisica, Istituto Nazionale di Fisica Nucleare, Padova, Italy*

(Presented 9 June 2016; received 6 June 2016; accepted 21 July 2016; published online 18 August 2016)

Gamma-ray spectroscopy measurements at MHz counting rates have been carried out, for the first time, with a compact spectrometer based on a $LaBr_3$ scintillator and silicon photomultipliers. The instrument, which is also insensitive to magnetic fields, has been developed in view of the upgrade of the gamma-ray camera diagnostic for α particle measurements in deuterium-tritium plasmas of the Joint European Torus. Spectra were measured up to 2.9 MHz with a projected energy resolution of 3%-4% in the 3-5 MeV range, of interest for fast ion physics studies in fusion plasmas. The results reported here pave the way to first time measurements of the confined α particle profile in high power plasmas of the next deuterium-tritium campaign at the Joint European Torus. [http://dx.doi.org/10.1063/1.4961073]

I. INTRODUCTION

As magnetic fusion science matures towards the exploitation of high power tokamak devices, there is a pressing demand to better understand the role played by the energetic ions in the sustainment of the thermonuclear process.[1] From the experimental point of view, this calls for the need to develop dedicated diagnostic systems that can be operated in the harsh, neutron rich environment of a high performance tokamak. As mostly demonstrated at the Joint European Torus (JET), neutron and gamma-ray spectroscopy measurements are among the primary techniques for fast ion studies in plasmas of deuterium and deuterium-tritium at high power. Neutron measurements can especially diagnose supra-thermal components of the fuel ion energy distribution by observation of the corresponding high energy tails in the spectrum.[2–4] Gamma-rays are instead the main tool to study the charged energetic products of the fusion reactions.[5–10]

In view of the forthcoming full power deuterium-tritium campaign, a number of diagnostics are undergoing major upgrades at JET. The gamma-ray camera,[5,11] i.e., a multi-chord system aimed at determining the map of the gamma-ray emissivity in the poloidal plane by tomographic inversion, is among these and is expected to be the main instrument that will determine the α particle profile by measurements of the gamma-ray emission at 4.44 MeV from $^9Be(\alpha, n\gamma)^{12}C$ reactions in the plasma (at JET ^9Be comes from erosion of the machine first wall). The requirements for operating the detectors of the gamma-ray camera at full power are however very demanding. Space limitations constrain the detectors to fit a cylindrical capsule of 35 mm × 35 mm (height x diameter). There is then need for MHz counting rate capabilities, insensitivity to magnetic fields, and a peak energy resolution of 3%-4% in the 3-5 MeV range. No detector that can simultaneously satisfy these requirements is commercially available.

A dedicated instrument, based on a $LaBr_3$ crystal combined with silicon photo-multipliers (commercially known as Multi-Pixel Photon Counter, MPPC), has been developed to meet all of these requirements. Its detailed design and characterization in the laboratory are described elsewhere in these proceedings.[12] In this paper, we focus instead on the first time demonstration of gamma-ray spectroscopy measurements at MHz counting rates with this type of detector. The measurements were obtained in an experiment at a tandem nuclear accelerator, where counting rates up to 2.9 MHz could be reached.

The paper is organised as follows. The measurement setup and data analysis procedure are described in Section II. Gamma-ray spectra obtained in our experiment and their characterisation in terms of peak shift and energy resolution are presented in Section III. Implications of our findings and routes for further improvements are finally addressed in Section IV.

Note: Contributed paper, published as part of the Proceedings of the 21st Topical Conference on High-Temperature Plasma Diagnostics, Madison, Wisconsin, USA, June 2016.
[a)]massimo.nocente@mib.infn.it
[b)]See the Appendix of F. Romanelli *et al.*, Proceedings of the 25th IAEA Fusion Energy Conference 2014, Saint Petersburg, Russia.

II. EXPERIMENTAL SETUP AND DATA ANALYSIS

High counting rate gamma-ray spectroscopy measurements were performed at the TANDEM-ALPI accelerator of the Italian Institute of Nuclear Physics in Legnaro. A beam of 10 MeV protons was collimated onto a target of ^{27}Al placed in a cylindrical vacuum chamber. The MPPC detector was installed inside the chamber and at a distance of less than 1 cm from the target. The thickness of the target was chosen to fully stop the proton beam and maximise gamma-ray production. This arose from either inelastic proton scattering on aluminium or the ^{27}Al(p,$\alpha\gamma$)^{24}Mg nuclear reaction. A photo-multiplier tube (PMT) equipped with a $1'' \times 1''$ $LaBr_3$ detector was placed outside the vacuum chamber and at a distance of about 20 cm from the target. This second detector, whose counting rate never exceeded 250 kHz at the highest proton currents we have used (30 nA), was used to benchmark the determination of the counting rate on the MPPC detector (see the description below).

The raw signals from both the PMT and MPPC were digitized with a CAEN DT5730 digitizer (500 MHz, 14 bits, 2 V dynamic range), without any intermediate amplification stage. In this way, the duration of the electronic signal from a gamma-ray event was about 100 ns, which is essential to limit the extent of pile up for spectroscopy measurements at MHz counting rates.[13–15] When a pulse exceeded a chosen threshold, corresponding to an energy around 500 keV, a trigger was launched and a window of 300 ns was opened to digitise signals from the PMT and MPPC occurring within the window. The MPPC was operated at 65.8 V, which is 0.6 V above the breakdown voltage (see Ref. 16). The energy spectrum was reconstructed after each measurement based on the interpolation procedure described in Ref. 13. To this end, we fitted each digitised waveform with the expected pulse shape $y(t)$ from a silicon photomultiplier,[17] i.e.,

$$y(t) = \begin{cases} A \text{ if } t < t_0 \\ A + N \cdot (1 - \exp(-(t - t_0)/\tau_1)), \\ \exp(-(t - t_0)/\tau_2) \text{ if } t > t_0 \end{cases} \quad (1)$$

where $\tau_1 = 30.4$ ns and $\tau_2 = 22.6$ ns were constant for all waveforms and A, N, and t_0 were instead determined by the fit. The resulting fit parameters were used to calculate the pulse height of each event and build the energy spectrum. A standard pile up rejection routine was applied before fitting so to discard events that had more than one pulse within a single 300 ns acquisition window.

An essential quantity for our experiment was the counting rate r on the MPPC which, due to pile up, does not always coincide with the number of triggers per unit time, especially at the highest detector loads. We have thus determined r by averaging the number of pulses recorded in several acquisition windows lasting 1 μs and launched before each measurement of the spectrum without any energy threshold. In order to benchmark our determination, we have further verified that, as the beam current was increased, r remained proportional to the rate of the external PMT monitor, which was exposed to a 10 times lower radiation load. Counting rates between 52 kHz and 2.9 MHz on the MPPC detector were assessed in our experiment.

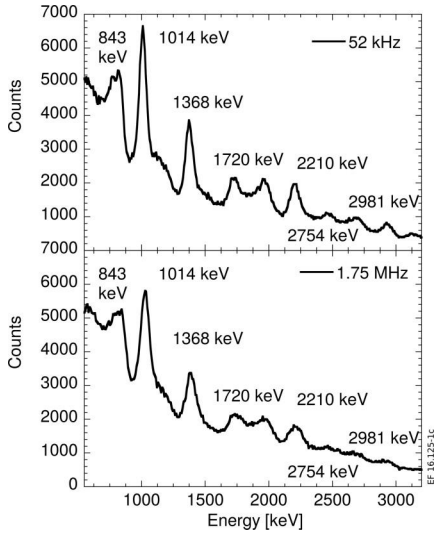

FIG. 1. Gamma-ray spectra measured by the MPPC detector at counting rates of 52 kHz (top) and 1.75 MHz (bottom). The energies of the peaks observed in the spectrum are individually marked in each panel.

III. RESULTS

Figure 1 shows the gamma-ray energy spectra measured at counting rates of 52 kHz and 1.75 MHz. Even when r is as high as 1.75 MHz, we are able to resolve all of the peaks marked in the figure and observed at the more moderate rate of 52 kHz. The main difference between the two spectra is mostly in terms of the energy resolution, which appears to be coarser at high counting rates. The gamma-ray peaks we have identified sit on an exponential background that is significantly more pronounced in the MHz range. This is due to the activation of the vacuum chamber where the experiment was performed and which increases at the highest proton beam currents.

As the energy resolution is an important parameter for our goal, we have quantified its changes as a function of r, with the results shown in Figure 2. The resolution (%) is here defined as the ratio between the width and position of each peak. The error bar associated to $E_\gamma = 1720$ keV is largest as this energy had the worst peak to background ratio. We also did not try to extract values at the 2754 and 2981 keV peaks, as they barely stand out of the background at 1.75 MHz. Unlike the measurement in Ref. 13 with a $3'' \times 6''$ $LaBr_3$ scintillator and a PMT, we here observe a clear change

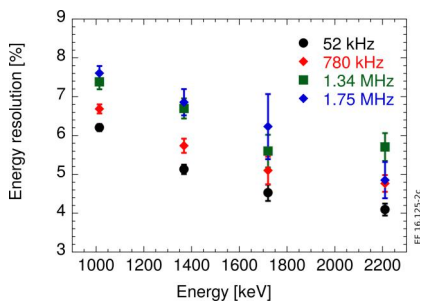

FIG. 2. Energy resolution measured at the main peaks observed in the spectrum and as a function of the counting rate.

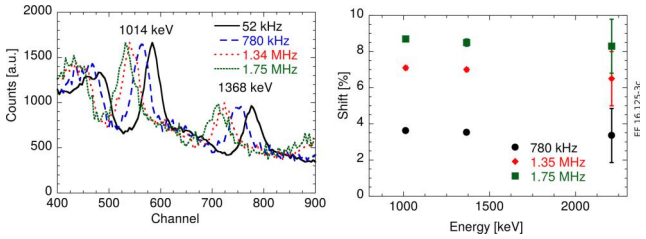

FIG. 3. (left) Effect of the gain drift on the gamma-ray spectra measured in our experiment and due to the increasing average current flowing in the MPPC. The amplitudes of the spectra were normalised to the values at $r = 52$ kHz (right). Relative change of the mean peak position as a function of the counting rate and with respect to values at 52 kHz. When not indicated, the size of the error bars coincides with that of the symbols.

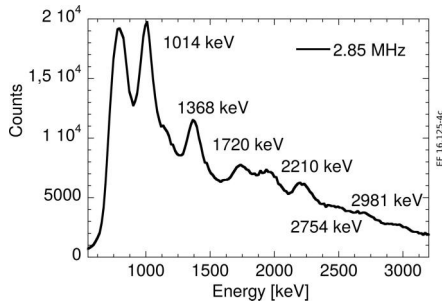

FIG. 4. Gamma-ray energy spectrum measured at a counting rate of 2.9 MHz and by operating the MPPC at a reduced voltage of 65.5 V. A higher energy threshold has been used compared to the measurements in Figure 1.

of the energy resolution between 1% and 2% at all peaks. However, we have verified that, at a given counting rate, the energy resolution predominantly scales as $1/\sqrt{E_\gamma}$, as expected from Poisson statistics. This implies that we can extrapolate a value between 3% and 4% at the 4.44 MeV peak from the ^{9}Be$(\alpha,\mathrm{n}\gamma)^{12}$C reaction at $r = 1.75$ MHz, which is deemed sufficient to distinguish this emission from nearby lines, with mean energies typically separated by a few hundreds keV.

A second aspect that is worth mentioning is the observed downward shift of the mean peak position as a function of r and illustrated in Figure 3. As shown in the right panel, the relative shift increases with the counting rate, but is independent from the gamma-ray energy. This suggests that the increasing average current flowing in the device, $\langle I_S \rangle$, which scales linearly with r, affects the gain of the MPPC. In particular, by analysing time resolved data, we were able to separate two contributions to the peak shift. The first contribution was manifested from the beginning and comes from an additional voltage drop along the resistors of the MPPC electronic board.[12] This is due to $\langle I_S \rangle$ and reduces the effective gain of the MPPC. Since $\langle I_S \rangle$ is also a source of local heating for the device, there is then a second contribution that comes from the increase of the local temperature, which further reduces the MPPC gain,[16] and occurs until thermal equilibrium is reached on a time scale of a few seconds. In Figure 3, we only show the first, unavoidable contribution to the shift, as the latter can be counteracted by real time control of the MPPC gain with a temperature sensor[18] or by time resolved measurements. The energy resolutions reported in Figure 2 were instead evaluated by integrating our measurements over a time window after the MPPC had reached thermal equilibrium.

As a final test of the capability of our device to operate at high counting rates, we finally increased the proton beam current up to 30 nA, which was the highest value allowed by radiation protection limits and corresponded to 2.9 MHz on the MPPC detector. We also decided to operate the device at 65.5 V, i.e., only about 0.3 V above the break down. The resulting spectrum is displayed in Figure 4 and shows that all of the peaks can still be distinguished, but at the price of an overall worsened energy resolution (7% at $E_\gamma = 2210$ keV) and a significantly higher background from the activation of the vacuum chamber. Even higher counting rates may be sustained by the device, which provides additional confidence on the detector capability to perform spectroscopy measurements in the MHz range.

IV. DISCUSSION

Gamma-ray measurements of the 4.44 MeV peak from the ^{9}Be$(\alpha,\mathrm{n}\gamma)^{12}$C reaction in deuterium-tritium plasmas must always be accomplished in a high background of 14 MeV neutrons, which are born from the main fusion reactions. 14 MeV neutrons interact with the $LaBr_3$ crystal[19,20] and induce a direct background that can be reduced by the use of suitable attenuators, but that cannot be fully suppressed. Preliminary calculations for a JET deuterium-tritium plasma reveal that a detector load of the order of 1 MHz, mostly with events at $E_\gamma < 3$ MeV, may be expected in a full power deuterium-tritium discharge from the 14 MeV neutrons, with a contribution of about 1-10 kHz from ^{9}Be$(\alpha,\mathrm{n}\gamma)^{12}$C reactions at 4.44 MeV. As discussed in Ref. 13, the effect of the radiation load on the detector depends on the average current flowing in the device, which is in turn proportional to the product between the average energy of the measured spectrum, $\langle E_\gamma \rangle$, and the counting rate. From Figure 1 we can calculate $\langle E_\gamma \rangle \approx 0.65$ MeV for our measurements and that compares to $\langle E_\gamma \rangle \approx 0.68$ MeV for 14 MeV neutrons impinging on the $LaBr_3$ crystal we have used. As we were able to successfully measure the spectrum from p + ^{27}Al reactions up to 2.9 MHz, this implies that a correspondingly high detector load may be tolerated in a measurement at JET.

Although our measurements already demonstrate the technical feasibility of α particle measurements by gamma-ray spectroscopy in a JET deuterium tritium plasma, further improvements may be envisaged. An example is the energy resolution that, at kHz counting rates, has an optimum at about 3 V above the MPPC breakdown[16,17] so that, depending on the actual extent of the 14 MeV neutron background in each plasma scenario, operations at higher MPPC voltage (and correspondingly better energy resolution) may be feasible. In our measurements, we did not seek to obtain the optimal energy resolution, but rather to show that spectroscopy measurements at MHz counting rates could be performed at an energy resolution sufficient for our scope.

A second amelioration may then come from the use of an active circuit for signal read-out from the MPPC, for example, based on a transimpedance amplifier circuit (TIA) instead of a passive differentiator circuit as in our measurements.[12,18] Laboratory tests[18] have shown that a TIA circuit can minimise the gain shifts due to the average current in the device, but with the need of an additional power supply to feed the operational

amplifier of the TIA. High counting rate tests of a $CeBr_3$ detector coupled with an MPPC and TIA readout were also performed in our experiment and will be reported in a separate paper.

V. CONCLUSIONS

Gamma-ray spectroscopy measurements from $p + {}^{27}Al$ reactions at counting rates from 50 kHz up to 2.9 MHz were successfully performed for the first time with a compact $LaBr_3$ detector and a silicon photo-multiplier readout. In all cases, we were able to successfully reconstruct all of the peaks expected from the reactions and with an energy resolution that extrapolates to 3%-4% in the E_γ = 3-5 MeV range of interest for fast ion studies with gamma-ray spectroscopy at JET. An increasing downward shift of the mean peak position as a function of the counting rate was also observed, as expected, but this is of no concern as it can be counteracted by time resolved measurements at JET.

Our results demonstrate the technical feasibility of spectroscopy measurements with the JET gamma-ray camera upgrade in forthcoming deuterium-tritium plasmas at high performance and, more generally, show that good energy resolution, MHz rate capabilities, insensitivity to magnetic fields, and compact dimensions can all be combined within a single gamma-ray spectrometer.

ACKNOWLEDGMENTS

This work has been carried out within the framework of the EUROfusion Consortium and has received funding from the Euratom research and training programme 2014-2018 under Grant Agreement No 633053. The views and opinions expressed herein do not necessarily reflect those of the European Commission.

[1]N. N. Gorelenkov, S. D. Pinches, and K. Toi, Nucl. Fusion **54**, 125001 (2014).
[2]J. Eriksson *et al.*, Nucl. Fusion **55**, 123026 (2015).
[3]C. Hellesen *et al.*, Nucl. Fusion **53**, 113009 (2013).
[4]M. Tardocchi, M. Nocente, and G. Gorini, Plasma Phys. Controlled Fusion **55**, 074014 (2013).
[5]V. Kiptily, F. E. Cecil, and S. S. Medley, Plasma Phys. Controlled Fusion **48**, R59 (2006).
[6]M. Nocente *et al.*, Nucl. Fusion **52**, 063009 (2012).
[7]M. Tardocchi *et al.*, Phys. Rev. Lett. **107**, 205002 (2011).
[8]M. Salewski *et al.*, Nucl. Fusion **55**, 093029 (2015).
[9]M. Salewski *et al.*, Nucl. Fusion **56**, 046009 (2016).
[10]I. Proverbio, M. Nocente, V. G. Kiptily, M. Tardocchi, G. Gorini, and JET-EFDA Contributors, Rev. Sci. Instrum. **81**, 10D320 (2010).
[11]V. G. Kiptily *et al.*, Nucl. Fusion **45**, L21 (2005).
[12]D. Rigamonti *et al.*, "Performance of the prototype $LaBr_3$ spectrometer developed for the JET gamma-ray camera upgrade," Rev. Sci. Instrum. (these proceedings).
[13]M. Nocente *et al.*, IEEE Trans. Nucl. Sci. **60**, 1408 (2013).
[14]M. Nocente *et al.*, Rev. Sci. Instrum. **81**, 10D321 (2010).
[15]B. Löher, D. Savran, E. Fiori, M. Miklavec, N. Pietralla, and M. Vencelj, Nucl. Instrum. Methods Phys. Res., Sect. A **686**, 1 (2012).
[16]M. Grodzicka, M. Moszynski, T. Szczesniak, M. Szawlowski, and J. Baszak, J. Instrum. **8**, P09020 (2013).
[17]M. Nocente, A. Fazzi, M. Tardocchi, C. Cazzaniga, M. Lorenzoli, C. Pirovano, M. Rebai, C. Uboldi, V. Varoli, and G. Gorini, Rev. Sci. Instrum. **85**, 11E108 (2014).
[18]I. Zychor *et al.*, Phys. Scr. **91**, 064003 (2016).
[19]C. Cazzaniga, M. Nocente, M. Tardocchi, M. Rebai, M. Pillon, F. Camera, A. Giaz, L. Pellegri, and G. Gorini, Nucl. Instrum. Methods Phys. Res., Sect. A **778**, 20 (2015).
[20]C. Cazzaniga *et al.*, Rev. Sci. Instrum. **84**, 123505 (2013).

Paper III

Jinst

Published by IOP Publishing for Sissa Medialab

Received: *May 19, 2017*
Accepted: *October 3, 2017*
Published: *October 18, 2017*

2nd European Conference on Plasma Diagnostics (ECPD2017)
from 18th to 21st April 2017
Bordeaux, France

Characterization of a compact $LaBr_3$(Ce) detector with Silicon photomultipliers at high 14 MeV neutron fluxes

D. Rigamonti,[a,b,1] **M. Nocente,**[a,b] **L. Giacomelli,**[b] **M. Tardocchi,**[b] **M. Angelone,**[c] **A. Broslawski,**[d] **C. Cazzaniga,**[e] **J. Figueiredo,**[f,g] **G. Gorini,**[a,b] **V. Kiptily,**[h] **S. Korolczuk,**[d] **A. Murari,**[g,i] **M. Pillon,**[c] **R. Pilotti,**[j] **I. Zychor**[d] **and JET Contributors**[2]

[a] *Dipartimento di Fisica "G. Occhialini", Università degli Studi di Milano-Bicocca, Piazza della Scienza 3, 20126, Milano, Italy*
[b] *Istituto di Fisica del Plasma "P. Caldirola", CNR, Via R. Cozzi 53, 20125, Milano, Italy*
[c] *ENEA C.R. Frascati, Via E. Fermi 45, 00044 Frascati, Italy*
[d] *Narodowe Centrum Badań Jądrowych (NCBJ), 05-400 Otwock-Swierk, Poland*
[e] *ISIS Facility, Science and Technology Facilities Council, Rutherford Appleton Laboratory, Didcot OX11 0QX, United Kingdom*
[f] *Instituto de Plasmas e Fusão Nuclear, Instituto Superior Técnico, Universidade de Lisboa, Lisboa, Portugal*
[g] *EUROfusion Programme Management Unit, Culham Science Centre, OX14 3DB Abingdon, United Kingdom*
[h] *Culham Science Centre for Fusion Energy, Culham, United Kingdom*
[i] *Consorzio RFX (CNR, ENEA, INFN, Università di Padova, Acciaierie Venete SpA), Padova, Italy*
[j] *Università degli Studi Tor Vergata (Roma), Via del Politecnico 1, 00100, Roma, Italy*

E-mail: davide.rigamonti@mib.infn.it

Abstract: A new compact gamma-ray spectrometer based on a Silicon Photo-Multiplier (SiPM) coupled to a $LaBr_3$(Ce) crystal has been developed for the upgrade of the Gamma Camera (GC) of JET, where it must operate in a high intensity neutron/gamma-ray admixed field. The work presents the results of an experiment aimed at characterizing the effect of 14 MeV neutron irradiation on both $LaBr_3$(Ce) and SiPM that compose the full detector. The pulse height spectrum from neutron interactions with the crystal has been measured and is successfully reproduced by MCNP simulations. It is calculated that about 8% of the impinging neutrons leave a detectable signal of which less than $< 4\%$ of the events occur in the energy region above 3 MeV, which is of interest for gamma-ray spectroscopy applications. Neutron irradiation also partly degrades the performance of

[1] Corresponding author.
[2] See the author list of X. Litaudon et al., *Overview of the JET results in support to ITER*, *Nucl. Fusion* **57** (2017) 102001.

https://doi.org/10.1088/1748-0221/12/10/C10007

the SiPM and this is mostly manifested as an increase of the dark current versus the neutron fluence. However, it was found that the SiPM can be still operated up to a fluence of 4×10^{10} n/cm^2, which is the highest value we experimentally tested. Implications of these results for GC measurements at JET are discussed.

KEYWORDS: Nuclear instruments and methods for hot plasma diagnostics; Photon detectors for UV, visible and IR photons (solid-state) (PIN diodes, APDs, Si-PMTs, G-APDs, CCDs, EBCCDs, EMCCDs etc); Radiation-hard detectors; Spectrometers

2017 JINST 12 C10007

Contents

2017 JINST 12 C10007

1 Introduction

Gamma-ray spectroscopy aims at investigating the behaviour of fast ions in high temperature fusion reactors by observation of the gamma-ray (γ) emission produced in nuclear reactions between the energetic ions and impurities in the machine. The success of this technique has been demonstrated mostly at JET [1–5], where a number of γ diagnostics consisting of scintillator detectors, germanium detectors and two Gamma Cameras (GC), one horizontal and one vertical, are available. The GC systems consist of a fan shaped array of detectors embedded in a concrete shielding block and measuring γ emission along 9 vertical and 10 horizontal well collimated lines of sights through the plasma poloidal section. The main application of the diagnostics is to infer the spatial profile of γ's emitted in the plasma from fast ion reactions, which is obtained by a tomographic inversion of line integrated measurements [6]. Of special interest is its use in plasmas with Deuterium (D) and Tritium (T), where the reaction D(T,n)α takes place and the detection of the 4.44 MeV γ's emitted by ^{9}Be(α,nγ)^{12}C reactions is one way to measure the profile of confined alpha particles [7] in view of the presence of Be impurities from the Be tiles of JET ITER-like wall.

In order to improve the data quality of the existing system, new detectors have been developed and are being installed at JET to enable γ spectroscopy in the forthcoming high power plasma campaigns with and without tritium. The upgrade makes γ measurements at MCounts/s counting rates possible for the first time, in addition to an improved energy resolution (say 5% at 662 keV compared with 10–20% of the present system) in the harsh neutron-γ mixed environmental background expected especially during operations with tritium [8, 9]. In order to meet these requirements, together with the very limited space available for the detectors — which rules out the use of conventional Photo-Multiplier Tubes (PMT) with magnetic shielding — a compact γ spectrometer based on a Silicon Photo-Multiplier (SiPM) coupled to a $LaBr_3$(Ce) scintillator crystal has been developed. The detailed design and characterization of the detectors are described in [9] and its capability to work at MCounts/s counting rates is reported in [8].

This paper presents instead the experimental results on the effect of 14 MeV neutrons on the GC spectrometers. The measurements were performed at the Frascati Neutron Generator (FNG) under controlled neutron fluxes. In particular, the background energy spectrum induced by 14 MeV neutrons interacting with the spectrometer was studied and successfully interpreted by means of MCNP simulations. Results on the neutron damage of the SiPM used as an alternative to conventional PMT for our detector are also reported. Implications of these results on the use of the JET GC for different plasma conditions are finally discussed.

2 Experimental setup

Measurements were performed at FNG where quasi monochromatic 14 MeV neutrons are produced by accelerated deuterium ions impinging on a tritiated-titanium target [10]. In order to separately study the response of $LaBr_3$(Ce) to 14 MeV neutrons and the damage of SiPM under neutron irradiation, we have performed two different experiments.

In the first experiment, the 25.4 mm × 16.9 mm (diameter × height) $LaBr_3$(Ce) crystal was coupled to a standard Photomultiplier Tube (PMT) manufactured by Hamamatsu [11] (model R9420-100-10) and equipped with an active base. The detector was placed at an angle of zero degrees with respect to the beam and at the distance of 33 cm from the target, which corresponded to a neutron flux of 3.5×10^4 n/cm^2/s and a counting rate of 57 kCounts/s at the detector position. As the detector signal is 80 ns long at full width at half maximum (FWHM), at this rate we estimate that the pile up probability is lower than 1% and the distortion of the pulse height spectrum due to unresolved pile up events should be negligible. The neutron yield from the target was monitored as a function of time by the standard diagnostics of FNG which are alpha counters of the α's produced by DT reactions in the target. Individual events from the detector were recorded by a 500 MSample/s-14bit CAEN digitizer (model DT5730) [12], both by digitizing each waveform and by an online processing of the signals with a standard charge integration algorithm. The detector was calibrated with ^{137}Cs (E_γ = 662 keV) and ^{60}Co (E_γ = 1173 keV and 1333 keV) radioactive sources before neutron irradiation. In the second experiment, we placed a new Hamamatsu SiPM sample (model S12642-0404PB-50) [11], without the $LaBr_3$ crystal, at a distance of 18 cm from the target in order to study the effect of neutron irradiation at increased fluxes, up to a fluence of 4×10^{10} n/cm^2, which was obtained within some hours of irradiation also by increasing the deuterium beam current. A Keithley picoammeter Model 6487 was connected to the SiPM and used to monitor in real time the bias voltage of the device with a high degree of accuracy and its dark current with a precision of 1 pA (see figure 4-B). The SiPM was wrapped in an aluminum foil to provide shielding against possible electromagnetic pick up noise. Besides the dark current, we periodically measured the characteristic current-voltage (I-V) curve of the device at different values of the fluence during the irradiation as a way to track possible changes in the break down voltage of the SiPM.

3 Results

3.1 $LaBr_3$ crystal response to 14 MeV neutron irradiation

The pulse height spectrum obtained by irradiating the $LaBr_3$ crystal with 14 MeV neutrons was recorded at a neutron flux of 3.5×10^4 n/cm^2/s and with an integration time of 1200 seconds (see

2017 JINST 12 C10007

figure 1). The overall shape of the spectrum is roughly exponential with a few characteristic peaks that stand out. We find that most of the events occur in the region $E_{\mathrm{dep}} < 3$ MeV. In the region nearby 4.44 MeV the shape is instead relatively flat and the absolute magnitude is suppressed by a factor about 300 compared to values at $E_{\mathrm{dep}} < 1$ MeV, which is beneficial for gamma-ray spectroscopy applications.

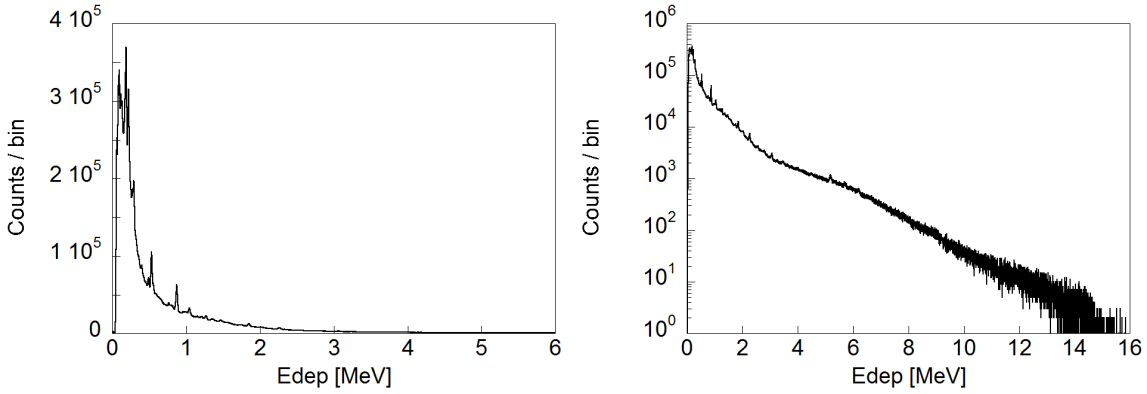

Figure 1. Energy spectra both in linear (left) and logarithmic (right) scale measured at FNG with a 25.4 mm × 16.9 mm $LaBr_3$ crystal in 14 MeV neutron irradiation experiments. The counting rate at the detector is 57 kCounts/s and the integration time is 1200 s.

Specifically, as described in [13], we can ascribe the detailed structures appearing in the spectrum to reactions between 14 MeV (direct) neutrons and nuclei of the detector material (^{139}La, ^{79}Br, ^{81}Br). Inelastic neutron scattering is an important mechanism and is the main contributor to the visible peaks in the spectrum. In the high energy range of relevance for gamma-ray applications, however, the signal is dominated by the production of secondary particles from nuclear reactions in the scintillator material. These can either be charged particles (protons, deuterons, alphas), that deposit their full energy in the detector, or secondary neutrons from (n,2n) reactions that lead to an additional background. Besides the direct neutrons, scattered neutrons as well as environmental gamma-rays contribute to the measured spectrum.

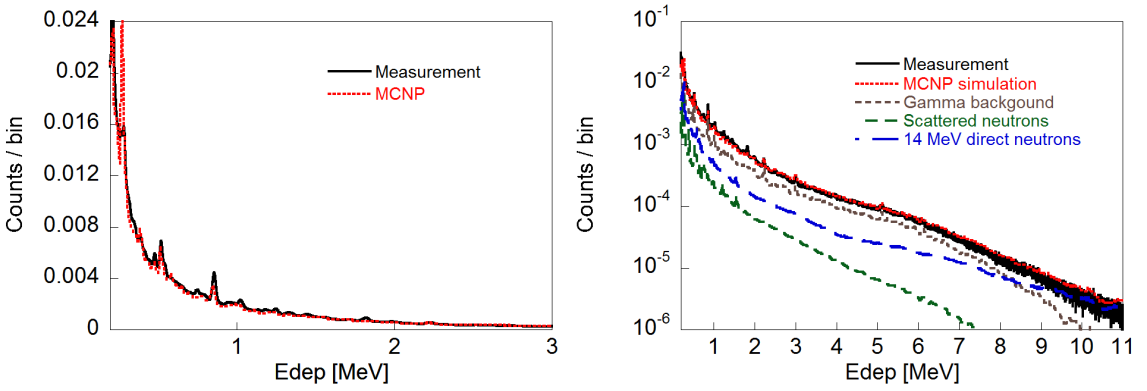

Figure 2. Comparison between the measurement (normalized) and the MCNP simulation both in linear (left) and in logarithmic (right) scale. In the figure on the right, the contributions due to the gamma background, the scattered neutrons and the 14 MeV direct neutrons are shown.

2017 JINST 12 C10007

For a detailed understanding of the $LaBr_3(Ce)$ response, a MCNP model of the FNG facility [10] has been used to evaluate the contribution of the direct neutron component based on the reactions listed in [13] and to disentangle the signatures from scattered neutrons and γ's. The comparison between simulation and measurements (figure 2) shows a remarkably good agreement. By fitting the spectral shape of the three components to the data of figure 2, we find that of the recorded events 50% is due to direct 14 MeV neutrons (efficiency detection of about 8.2%), 31% is due to environmental γ and 19% are scattered neutrons. Purely in terms of counting rate capability of the spectrometer, since the maximum counting rate that can be sustained by the detector is of a few MCounts/s (as shown in [8]), our results imply that operations at impinging neutron fluxes up to a few 10^6 n/cm^2/s can be coped with at JET.

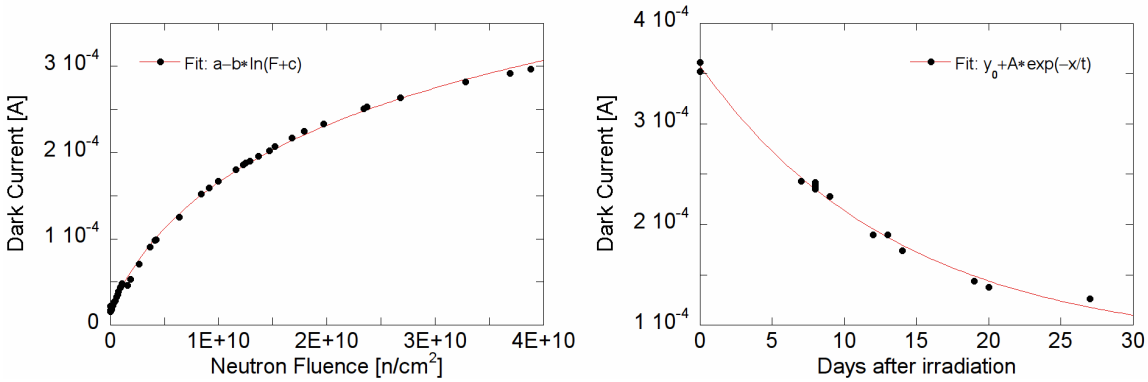

Figure 3. (Left) Dark current measured as a function of the neutron fluence at the detector. (Right) Dark current measured after the neutron irradiation experiment partially decreases after few days.

3.2 Resistance of SiPM to high 14 MeV neutron flux

The effect of neutron damage of the SiPM was studied by measurements of the dark current (initially at about 5.0 μA) and pulse height spectrum as a function of the neutron fluence. As shown in figure 3

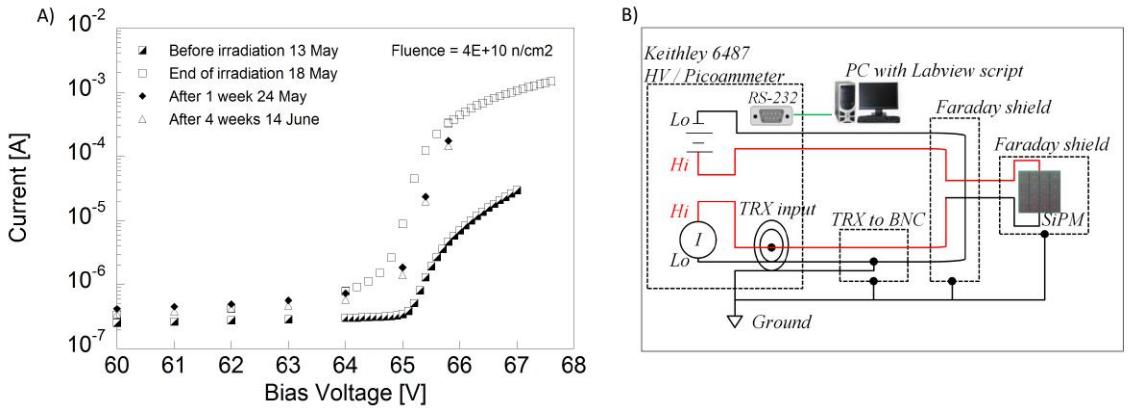

Figure 4. (A) Characteristic current-voltage curve before and after the neutron irradiation. (B) Schematic of the experimental setup.

2017 JINST 12 C10007

(left), the SiPM dark current increases as a function of the neutron fluence F and the data points are experimentally well fitted by the curve $f(F) = a - b \cdot \ln(F + c)$; here, a, b and c are free parameters. The graph on the right of figure 3 illustrates that, after irradiation, a self-recovery process takes place and the dark current decreases exponentially on a time scale of a few days down to an asymptotic value that, however, is larger than that measured before the irradiation experiment. This phenomenon occurred at room temperature with no applied bias voltage and is consistent with the findings of [14].

As far as the current-voltage curve of the SiPM after irradiation is concerned (figure 4-A), we observe that, in general, it has a higher value after irradiation, but it decreases on a time scale of a few days in a way consistent with the behavior found for the dark current. The breakdown voltage of each curve is however the same in all cases and this suggests that no permanent damage occurred to the SiPM, up to the maximum fluence we tested, i.e. 4×10^{10} n/cm^2. An independent confirmation comes from the calibration spectrum of figure 5, which we obtained with a ^{60}Co γ source in the vicinity of the $LaBr_3$+SiPM detector right after the end of the irradiation experiment. The two 1173 keV and 1333 keV γ emission peaks are clearly visible. The measured energy resolutions are 5.1 and 5.2%, respectively, which compare to the values before the irradiation. We also observe a higher background contribution in the spectrum which is ascribed to the activation of the FNG experimental hall and materials near the spectrometer.

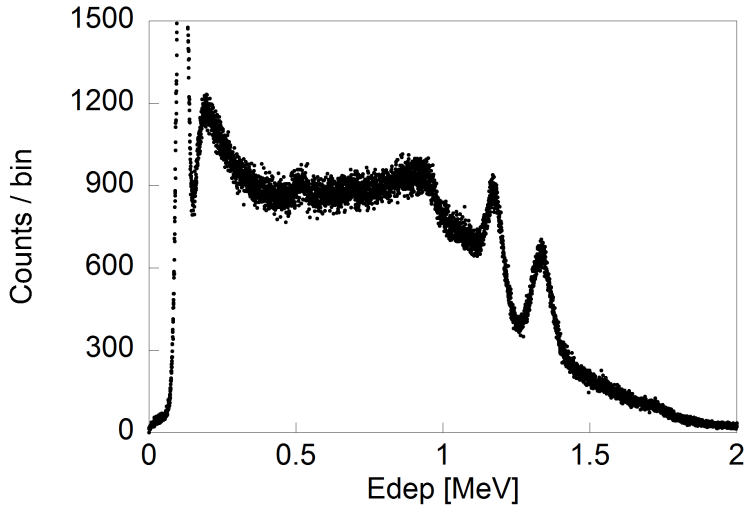

Figure 5. Gamma-ray energy spectrum measured from a ^{60}Co gamma-ray source.

4 Discussions

The extrapolation of the SiPM irradiation results to measurements at JET is very favorable. The estimated neutron fluxes for the next JET DT plasmas are in the range 10^7 n/cm^2/s on the central channel of the vertical camera and 10^8 n/cm^2/s for the horizontal GC, when the total neutron yield for JET high power DT plasmas is about 2×10^{18} n/s. This is the record value obtained so far in a DT plasma for less than 1 s in a transient scenario. The maximum fluence we have tested at FNG

2017 JINST 12 C10007

therefore corresponds to about 400 s and 4000 s integration time of a full power DT discharge, in steady state conditions, for the horizontal and the vertical GC, respectively. Since the expected duration of the heating phase in full power DT plasmas at JET is about 5 s, and it is foreseen that only few discharges will reach record conditions, we conclude that the neutron damage of the SiPM is not an issue for our applications. A different consideration applies instead to the extent of direct neutron interactions with the $LaBr_3$(Ce) crystal. In this case, as discussed, in terms of counting rate capability the system can tolerate a maximum direct neutron flux of a few 10^6 n/s/cm^2. Moreover, as shown in [13], no evidence of neutron damage have been experienced with a neutron fluence up to 3×10^9 n/s which corresponds to more than 1000 s of few 10^6 n/s/cm^2 neutron irradiation flux. At JET a water attenuator, which provides a 14 MeV neutron attenuation factor of 100, is installed in front of the vertical camera, and a thinner one provides an attenuation of about 15 for the horizontal one. Furthermore, calculations reveal that, due to the relatively poor gamma-ray shielding available at JET, the direct neutron and background gamma-rays, mostly in the range $E < 1$ MeV, might be comparable. This implies that, in DT, the background counting rate is the limiting factor and might constrain the application of the cameras up to yields in the range 10^{16} n/s, well below those expected in a record discharge at steady state. On the other hand, no limitations are foreseen for applications in deuterium plasmas, where the projected neutron yields are always below 10^{16} n/s.

5 Conclusions

The effect of 14 MeV neutron irradiation on a new compact gamma-ray spectrometer, based on $LaBr_3$(Ce) and Silicon Photo-Multipliers and developed for the Gamma Camera (GC) at JET, has been studied. The pulse height spectrum resulting from neutron interactions with the $LaBr_3$(Ce) crystal has been measured and is successfully interpreted by MCNP simulations. It was found that about 8% of the impinging direct neutrons leave a signal in the detector and only about 3.7% of the events occur in the energy region above 3 MeV. Neutron induced damage of the SiPM is also observed, mostly as an increase of the dark current of the device as a function of the neutron fluence. The breakdown voltage is however unchanged and the SiPM can still be operated up to a fluence of 4×10^{10} n/cm^2. When projected to applications at JET, our results reveal that, due to the unavailability of suitable attenuators and shielding, the background counting rate from direct neutron interactions with $LaBr_3$(Ce) is the limiting factor and might constrain the use of the γ camera up to neutron yields in the range 10^{16} n/s in DT plasmas. For comparison, the highest neutron yield obtained so far in DT is 10^{18} n/s, albeit in a transient phase only. No limitations are instead expected for operations in D plasmas. Damage of the SiPM by neutron interactions is in general of no concern for both DT and D plasma operations.

Acknowledgments

This work has been carried out within the framework of the EUROfusion Consortium and has received funding from the Euratom research and training programme 2014–2018 under grant agreement No 633053. The views and opinions expressed herein do not necessarily reflect those of the European Commission.

2017 JINST 12 C10007

References

[1] V.G. Kiptily, F.E. Cecil and S.S. Medley, *Gamma ray diagnostics of high temperature magnetically confined fusion plasmas*, *Plasma Phys. Control. F.* **48** (2006) R59.

[2] M. Tardocchi, M. Nocente and G. Gorini, *Diagnosis of physical parameters of fast particles in high power fusion plasmas with high resolution neutron and gamma-ray spectroscopy*, *Plasma Phys. Control. F.* **55** (2013) 074014.

[3] M. Nocente et al., *High-resolution gamma ray spectroscopy measurements of the fast ion energy distribution in JET ^{4}He plasmas*, *Nucl. Fusion* **52** (2012) 063009.

[4] J. Eriksson et al., *Dual sightline measurements of MeV range deuterons with neutron and gamma-ray spectroscopy at JET*, *Nucl. Fusion* **55** (2015) 123026.

[5] M. Salewski et al., *MeV-range velocity-space tomography from gamma-ray and neutron emission spectrometry measurements at JET*, *Nucl. Fusion* **57** (2017) 056001.

[6] J. Bielecki et al., *Phillips-Tikhonov regularization with a priori information for neutron emission tomographic reconstruction on Joint European Torus*, *Rev. Sci. Instrum.* **86** (2015) 093505.

[7] M. Nocente et al., *Conceptual design of the radial gamma ray spectrometers system for α particle and runaway electron measurements at ITER*, *Nucl. Fusion* **57** (2017) 076016.

[8] M. Nocente et al., *Gamma-ray spectroscopy at MHz counting rates with a compact $LaBr_3$ detector and silicon photomultipliers for fusion plasma applications*, *Rev. Sci. Instrum.* **87** (2016) 11E714.

[9] D. Rigamonti et al., *Performance of the prototype $LaBr_3$ spectrometer developed for the JET gamma-ray camera upgrade*, *Rev. Sci. Instrum.* **87** (2016) 11E717.

[10] M. Angelone et al., *Absolute experimental and numerical calibration of the 14 MeV neutron source at the Frascati neutron generator*, *Rev. Sci. Instrum.* **67** (1996) 2189.

[11] http://www.hamamatsu.com.

[12] http://www.caen.it.

[13] C. Cazzaniga et al., *Response of $LaBr_3$(Ce) scintillators to 14MeV fusion neutrons*, *Nucl. Instrum. Meth.* **A 778** (2015) 20.

[14] Y. Qiang, C. Zorn, F. Barbosa and E. Smith, *Radiation Hardness Tests of SiPMs for the JLab Hall D Barrel Calorimeter*, *Nucl. Instrum. Meth.* **A 698** (2013) 234 [arXiv:1207.3743].

2017 JINST 12 C10007

Paper IV

PROCEEDINGS OF SCIENCE

Capabilities of a Diamond Detector matrix for neutron spectroscopy measurements at JET*

D. Rigamonti[1,b,a], M. Tardocchi[a], C. Cazzaniga[b,a], M. Rebai[b,a], G. Croci[b,a], L.C. Giacomelli[a], G. Grosso[a], A. Muraro[a,b], M. Nocente[b,a], E. Perelli Cippo[a], P. Calvani[c], M. Gerolami[c], D. M.Trucchi[c], M. Angelone[d], M. Pillon[d], J. Figuereido[e], A. Murari[e], G. Gorini[a,b] and JET Contributors*

EUROfusion Consortium, JET, Culham Science Centre, Abingdon, OX14 3DB, UK
[a]Istituto di Fisica del Plasma "P. Caldirola", Milano, Italy
[b]Dipartimento di Fisica "G. Occhialini", Università degli Studi di Milano-Bicocca, Milano, Italy
[c]CNR–IMIP, Via Salaria, Monterotondo Scalo (Rm), Italy.
[d]ENEA-Frascati, Via E. Fermi XX, (Rm), Italy
[e]EUROfusion Programme Management Unit, Culham Science Centre, OX14 3DB, Abingdon, UK

E-mail: Tardocchi@ifp.cnr.it

Single-crystal Diamond Detectors (SDDs) feature high radiation hardness, fast response and compact size. This makes SDDs ideal candidates for fast neutron detectors in environment where high neutron flux is an issue such as the next generation burning plasmas experiments. Neutron detection in SDD is based on the collection of electron-hole pairs produced by charged particles generated by neutron interaction with ^{12}C nuclei. For neutron energies above about 7 MeV neutron spectroscopy is possible by measuring the deposited energy into the detector via the reaction $^{12}C(n,\alpha)^{9}Be$. This is indeed the cases of SDD measurements of 14 MeV neutrons of DT plasmas. A single pixel SDD (4.5x4.5x0.5 mm^3) prototype was installed at JET in 2013 and the achieved results allowed to assess also the neutron spectroscopic capability of deuterium plasmas. A 12-pixels SDD matrix has been recently realized and will be installed in 2015 at JET for DT plasmas as part of the Vertical Neutron Spectrometer project.

In this paper calibration of the SDD matrix with alpha particles in the laboratory and 14 MeV neutrons performed at the ENEA Frascati Neutron Generator will be presented. These calibrations have been performed with a fast charge preamplifier combined to a fast digital data acquisition, which allows for neutron spectroscopy measurements with simultaneously high energy resolution and high count rate capability. Both requirements are essential for neutron spectroscopy of high power fusion plasmas. The calibrations results achieved extrapolate favourably in view of future neutron spectroscopy measurements at JET using diamond detectors.

* See the Appendix of F. Romanelli et al., Proceedings of the 25th IAEA Fusion Energy Conference 2014, Saint Petersburg, Russia.

First EPs Conference on Plasma Diagnostics - 1st ECPD
14-17 April 2015,
Villa Mondragone , Frascati (Rome) Italy

1 Speaker

PoS(ECPD2015)061

1.Introduction

Single-crystal Diamond Detectors (SDDs) offer advantages such as high radiation hardness, fast response time and low sensitivity to magnetic fields which make them ideal candidates for fast neutron detectors in environments where high neutron flux is an issue, such as the next generation burning plasmas experiments [1]. Furthermore, their small size can be highly appreciated in those facilities for which a compact device is required. Neutron detection in SDD is based on the collection of electron-hole pairs produced by charge particles generated by neutron interaction with ^{12}C carbon nuclei in the detector. The main nuclear reaction channels occurring are:

- elastic and inelastic scattering $^{12}C(n,n')^{12}C$;
- n-3α reaction (carbon breakup) $^{12}C(n,n')3\alpha$ (Q_{value}=7.23 MeV);
- n-α reaction $^{12}C(n,\alpha)^{9}Be$ (Q_{value}=5.7 MeV).

The latter reaction $^{12}C(n,\alpha)^{9}Be$ is the selected one for 14 MeV neutron spectroscopy measurements from a Deuterium-Tritium (DT) plasma [2]. In this case, in fact, the resulting deposited energy in the detector corresponds to the incoming neutron energy minus the reaction Q-value. A peak centred at E ≈ 8.3 MeV which can be directly related to the incoming neutron spectrum. From the 14 MeV neutron spectrum information on plasma parameters can be extracted such as the ion temperature and the thermal/non thermal neutron emission ratio [3]. Furthermore, the remaining reaction channels give rise to a continuum in the pulse height spectrum. In particular the elastic and inelastic scattering contribute to the characteristic broad response function typical of compact neutron detectors which are based on recoil ion scattering and can still in principle be exploited for a basic neutron spectroscopy.

Previous tests with a single pixel prototype SDD have already shown excellent performances in neutron spectroscopy, such as a good energy resolution when a fast digital spectroscopic chain is used, a high count rate capability and the possibility to perform spatially resolved measurements of a fast neutron flux [4]. A single pixel SDD (4.5x4.5x0.5 mm^3) prototype was installed at JET in 2013 and the achieved results allowed to assess the 2.5 MeV neutron spectroscopic capability of Deuterium-Deuterium plasmas [5]. A new system based on a 12-pixels SDD matrix has been recently realized. Each pixel is equipped with independent high voltage supply and read-out electronics ad hoc built to combine the high counting rate capability with the good energy resolution. The matrix will be installed in 2015 at JET on a collimated vertical line of sight, for Deuterium-Tritium campaign as part of the Vertical Neutron Spectrometer project.

In this work the design and realization of the diamond system composed of 12 pixels SDD matrix and dedicated electronics will be presented. The use of dedicated fast charge preamplifier combined to a fast digital data acquisition has allowed for the first time to perform neutron spectroscopy measurements with simultaneously high energy resolution (<3% at 14 MeV) and high count rate capability (>1 MHz). Both requirements are essential for neutron spectroscopy of high power fusion plasmas. Calibration results with alpha particles in the laboratory and 14 MeV neutrons performed at the Frascati Neutron Generator will be presented.

2.Experimental setup description

1.1 Design and realization of the 12-pixel SDD matrix

A 12 pixel matrix was designed as neutron spectrometer and built at the CNR-ISM institute in Rome (Italy) [6-9]. Each pixel is made of a single-crystal diamond sample (4.5 x 4.5 mm^2 , 500 μm thick, with a boron concentration [B] < 5 ppb and nitrogen concentration [N] < 1 ppb), provided by Element Six Ltd [10]. In order to remove any organic and metallic impurity, each crystal was cleaned for 30 s in a boiling mixture (1:1:1) of nitric, sulphuric and perchloric acid, then rinsed in deionized water. Ohmic contacts were obtained on top and bottom surfaces by subsequent sputtering deposition of a multilayer metal structure (patent pending), followed by a final gold layer deposition. A dedicated 1 mm-thick alumina Printed Circuit Board (PCB) was designed and fabricated for the 12 pixel matrix. The bottom surface of the diamonds were glue with a thin layer of conductive silver paste on their respective pixel pad, whereas their top surfaces were wire-bonded on the ground plane [10]. Aimed at reducing cross-talk effects, each pixel pad and each signal track were completely surrounding by the ground plane. All pads and signal tracks, as well as the ground plane, are aluminum-made to minimize the metal activation by neutrons. A properly aluminum metal case has been designed and realized in order to house in the alumina PCB and to shield it from electromagnetic interference. Finally, the case was equipped with 12 SMA (SubMiniature version A) connectors for pixel biasing and signal collecting, and the top is provided with 12 holes (one per each pixel) to allow alpha particles to reach the diamonds for calibration measurements (the holes operate like pinhole collimators).

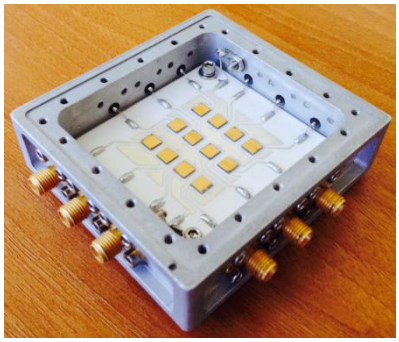

Figure 1. Picture of the 12-pixel diamond matrix without the top.

1.2 The acquisition chain

All the experiments present in this work, have been performed with the same digital acquisition chain, which will be used at JET.

Each pixel was equipped with an own independent read-out electronic, as well as an independent high voltage supply. The diamonds were powered with a bias voltage of +400 V provided by a CAEN HV module NDT1470 (4 channels) and an ISEG HV module EBS 8005 (8 channels) for the firsts four and the remaining pixels, respectively. Furthermore, each diamond was coupled through a 10 cm RG62 cable to a CIVIDEC C6 fast charge preamplifier [12], which has a rise time equal to 3.5 ns and a Gaussian pulse shape with a FWHM of 10 ns [13]. The fast preamplifier has been used in order to meet high rate measurement requirements. The downside of using a fast charge preamplifier is a degraded energy resolution compared to what can be achieved with conventional spectroscopic preamplifiers [13], which however are too

slow for usage in high rate applications. Via 15 m long cables the signals from the preamplifiers were fed into a 16 channel waveform digitizer CAEN module V1730B (14-bit, 500 MS/s) which was used to record the signals. The digitizer is equipped with a CAEN software able to perform on-line measurements of the pulse area, by integrating each signal in a user defined gate. In this way it was possible to build and store the deposited energy spectra.

1.3 Alpha particle measurements

In order to characterize and calibrate each single pixel with its own electronic chain, alpha particle measurements with a ^{241}Am source were performed in laboratory at the Istituto di Fisica del Plasma in Milan. At first, measurements were carried out in a vacuum chamber so as to decrease the alpha particle energy straggling and to have a more accurate calibration, then they were done again at atmospheric pressure. These second measurements were aimed to evaluate any future calibration performed in those environments where a vacuum chamber cannot be used, such as on the vertical line of sight of JET. Each pixel was coupled to the ^{241}Am source thanks to the 12 holes and the acquisition was performed pixel-by-pixel by using the electronic chain already described.

1.4 Measurements of 14 MeV neutrons at Frascati Neutron Generator

Measurements of 14 MeV neutrons were performed at the ENEA Frascati Neutron Generator (FNG) aimed to evaluate the matrix detector response. In this facility, the deuterium ions are accelerated and sent onto a tritiated-titanium target so that neutrons production occurs by deuterium-tritium reaction. The device was placed at 90° respect to the incoming deuterium beam at a distance of 22 cm from the target. A typical single pulse of a 14 MeV neutron recorded by a diamond pixel is shown in figure 2. It can be appreciated that the FWHM of the pulse is about 10 ns which is a necessary condition to be able to perform measurements at very high counting rates.

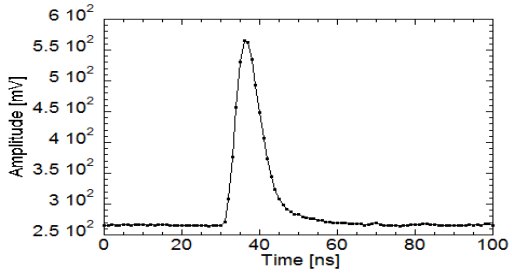

Figure 2: A single recorded waveform for a 14 MeV neutron is shown.

3.Results

Calibration measurements have been performed per each pixel with alpha particles both in vacuum and in air at atmospheric pressure. For the latter set-up, alpha-particle energy loss in air has been evaluated by SRIM code [14], which calculate the stopping and range of ions into matter. At first, each recorded spectrum was fitted by a Gaussian function in order to estimate its FWHM and peak position and then it was calibrated. Energy Resolution (FWHM/Peak Position) is plotted in figure 3. The mean value of the energy resolution for the recorded peaks during the measurements in vacuum is 1.74 % (96 KeV in terms of FWHM) with a standard deviation of

0.08 %. Figure 4, furthermore, shows the ratio of the peak position in vacuum to the peak position in air.

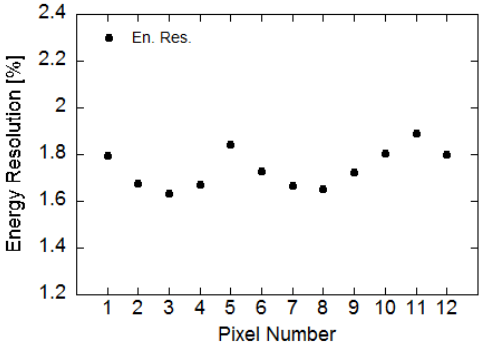

Figure 3: Energy Resolution dispersion graph for measurements in vacuum. Errors are not shown because of the same magnitude of the black dots.

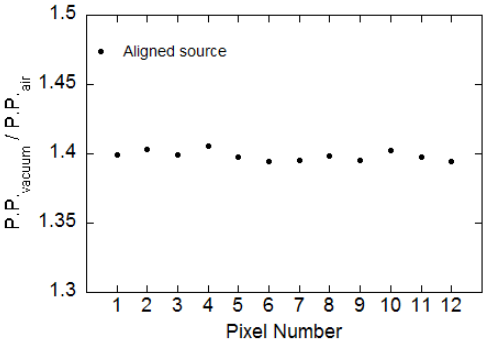

Figure 4: Ratio of the peak position in vacuum to the peak position in air. The blue dot represents the measurement with the non-aligned source.

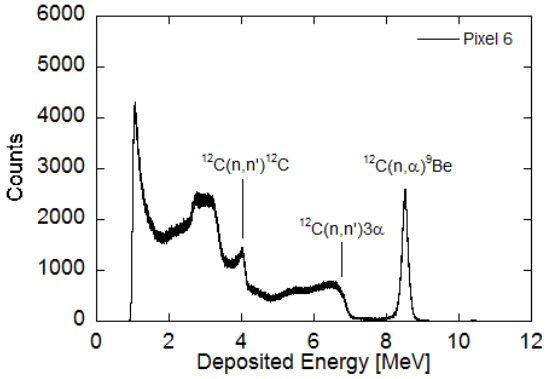

Figure 5: Deposited energy spectrum of 14 MeV neutrons for Pixel 6.

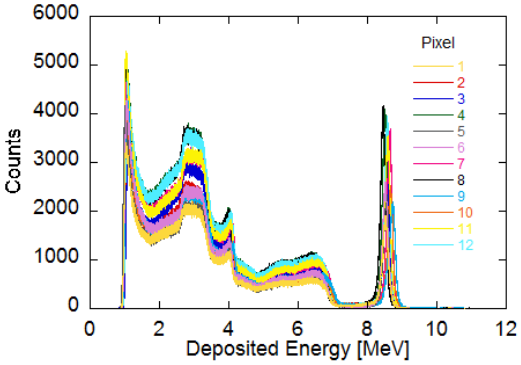

Figure 6: Pulse height spectra measured for each pixel at the FNG with14 MeV neutrons.

The recorded spectra at Frascati Neutron Generator were calibrated with the alpha calibration spectra. The peaks due to the n-α reaction were analyzed by a Gaussian fit in order to find the FWHM and peaks positions. The mean value of the calculated energy resolution for the 12 peaks is 191 KeV (in terms of FWHM) with a standard deviation of 17 KeV. Instead, the contribution of the beam energy width is estimated to be about 150 KeV. Therefore, we can assert that the intrinsic energy resolution of the detector is even less than 191 KeV. Figure 5 shows a single calibrated spectrum, whereas the figure 6 shows the calibrated pulse height spectra measured for each pixel of the matrix detector. In the latter graph, it is possible to notice a small shift of the (n,α) peak between different pixels. This is because the 12 pixels, which are in different positions, detect neutrons of different energy depending on their emission angle. Thanks to these measurements we can infer that all the pixel detectors feature a similar response in term of gain and energy resolution.

4.Conclusions

The response of a Single-crystal Diamond Detector matrix was measured with 14 MeV neutrons and alpha particles obtaining a mean energy resolution of 96 KeV and less than 191 KeV for 5.486 MeV alphas and 14 MeV neutrons, respectively. Furthermore as shown in the Rebai's paper [11], an equal response of each pixel to radiation was observed also for different

electronic chains and for neutron measurements. The detection system described in this work will allow for the first time to perform neutron spectroscopy measurements with simultaneously high energy resolution and high count rate capability, both required for neutron spectroscopy of high power fusion plasmas.

Acknowledgments

This work has been carried out within the framework of the EUROfusion Consortium and has received funding from the Euratom research and training programme 2014-2018 under grant agreement No 633053. The views and opinions expressed herein do not necessarily reflect those of the European Commission.

References

[1] H. Sjostrand et. al., *Rev. Sci. Instrum.* 77 (10), 10E702 (2006) http://dx.doi.org/10.1063/1.2336459.

[2] A. V. Krasilnikov et al., *Study of d-t neutron energy spectra at JETusing natural diamond detectors*, Nucl. Instrum. Methods Phys. Res. A476 (2002) 500-505.

[3] M. Tardocchi, M. Nocente and G. Gorini, *Diagnosis of physical parameters of fast particles in high power fusion plasmas with high resolution neutron and gamma-ray spectroscopy*, Plasma Phys. Control. Fusion **55** (2013) 074014.

[4] M. Nocente et. al., *Neutron spectroscopy measurements of tritium beam transport at JET*, Nucl. Fusion 54 (2014) 104010.

[5] C. Cazzaniga et. al., *Single crystal diamond detector measurements of deuterium-deuterium and deuterium-tritium neutrons at Join European Torus fusion plasmas*, ReV. Sci. Instrum. 85 (2014) 043506

[6] M. Rebai, *Response of a single-crystal diamond detector to fast neutrons*, 2013 JINST 8 P10007.

[7] M. Trucchi et al., *Very Fast and Primingless Single-Crystal-Diamond X-Ray Dosimeters*, IEEE Electron Device Lett. 33 (2012) 615.

[8] M. Girolami et al., *Diamond Detectors for UV and X-Ray Source Imaging*, IEEE Electron Device Lett. 33 (2012) 224.

[9] D.M. Trucchi et al., *Resistant and sensitive single-crystal diamond dosimeters for ionizing radiation*, Nucl. Instrum. Meth. A 718 (2013) 373.

[10] Element Six Ltd, http://www.e6.com

[11] M. Rebai et al., *Pixelated Single-crystal Diamond Detector for fast neutron measurements*, 2015 *JINST* **10** C03016

[12] Cividec, http://www.cividec.at

[13] C. Cazzaniga *et al., Rev. Sci. Instrum*. **85**, 11E101 (2014); http://dx.doi.org/10.1063/1.4885356

[14] SRIM, http://www.SRIM.org

Paper V

Neutron emission spectroscopy of DT plasmas at enhanced energy resolution with diamond detectors

L. Giacomelli,[1,a)] M. Nocente,[1,2] M. Rebai,[1,2] D. Rigamonti,[1,2] A. Milocco,[2] M. Tardocchi,[1] Z. J. Chen,[3] T. F. Du,[3] T. S. Fan,[3] Z. M. Hu,[3] X. Y. Peng,[3] A. Hjalmarsson,[4] G. Gorini,[1,2] and JET Contributors[5,b)]
[1]*Istituto di Fisica del Plasma "P. Caldirola," CNR, Milano, Italy*
[2]*Dipartimento di Fisica "G. Occhialini," Università degli Studi di Milano-Bicocca, Milano, Italy*
[3]*School of Physics, State Key Lab of Nuclear Physics and Technology, Peking University, Beijing, China*
[4]*Departments of Physics and Astronomy, Uppsala University, Uppsala, Sweden*
[5]*EUROfusion Consortium, JET, Culham Science Centre, Abingdon OX14 3DB, United Kingdom*

(Presented 7 June 2016; received 6 June 2016; accepted 2 July 2016; published online 17 August 2016)

This work presents measurements done at the Peking University Van de Graaff neutron source of the response of single crystal synthetic diamond (SD) detectors to quasi-monoenergetic neutrons of 14-20 MeV. The results show an energy resolution of 1% for incoming 20 MeV neutrons, which, together with 1% detection efficiency, opens up to new prospects for fast ion physics studies in high performance nuclear fusion devices such as SD neutron spectrometry of deuterium-tritium plasmas heated by neutral beam injection. [http://dx.doi.org/10.1063/1.4960307]

I. INTRODUCTION

Neutron emission spectroscopy (NES) is a diagnostic technique that measures the energy spectrum of neutrons born from the nuclear reactions of fusion plasmas. The application of neutron spectrometers based on different detection principles (magnetic proton recoil, time of flight, and compacts) includes studies at nuclear facilities as well as the development of diagnostic systems for fusion tokamaks.[1–5] The Joint European Torus[6] (JET, Culham, UK) has a special role in this respect as advanced spectrometers for 2.5 MeV and 14 MeV neutrons have been here developed for the first time and used to demonstrate measurements of the neutron spectrum from Deuterium (D) and Deuterium-Tritium (DT) plasmas with unprecedented energy resolution, accuracy, and time resolution, establishing NES as a key diagnostic for fast ion studies in high performance plasmas.[7–11]

Progress in chemical vapor deposition techniques has recently made it possible to grow Single crystal synthetic Diamonds (SDs), which can be used for NES applications.[12–18] SDs of the so-called electronic grade have been produced reliably with dimensions up to 4.5×4.5 mm^2 area and 0.5 mm thickness. SDs feature better performance with respect to what was achieved with natural diamonds.[19] The neutron detection principle is based on elastic scattering for neutrons up to 6 MeV and on $^{12}C(n,\alpha)^9Be$ ($Q_{value} = -5.7$ MeV) reactions at 14 MeV, of relevance for DT plasma discharges. SD offers the advantage of being compact, insensitive to magnetic field, low sensitivity to gamma ray background with intrinsic high energy resolution. In this paper we present the measurement of the response of SD to fast neutrons in the energy range 14–20 MeV performed at State Key Lab of Nuclear Physics and Technology of Peking University (Beijing, China) using a Van de Graaf accelerator.[20,21] Measurements of SD in the neutron energy range 1–4 MeV have also been done and are reported in Ref. 23. From the analysis of the measured SD response, a very good energy resolution has been found. The second part of the paper is dedicated to illustrate the potentiality offered by the SDs superior and unprecedented energy resolution for spectral studies of 14 MeV neutrons from DT plasmas, particularly, with regard to discharges heated by Neutral Beam Injection (NBI), and discuss its use to shed light on the ubiquitous discrepancy between simulated and measured neutron emissions at the JET.

II. EXPERIMENTAL SETUP AND MEASUREMENT OF THE SD RESPONSE FUNCTION

The SD used in these measurements was built at the CNR-ISM institute in Rome (Italy) and consists of a single crystal diamond sample ($4.5 \times 4.5 \times 0.5$ mm^3) with gold contacts. The detector was coupled through a short RG62 cable to a very fast charge sensitive preamplifier (rise time of 3.5 ns, shaping time of 25 ns, gain of 6 mV/fC) and was biased at +400 V which provided an electric field in the bulk of 0.8 V/μm. The preamplifier output was directly connected to the waveform digitizer CAEN DT5730 (14 bit and 500 MS/s sampling rate) equipped with software able to process the data on-line and sort them into a pulse charge histogram, i.e., pulse height spectrum (PHS). This setup allows achieving simultaneously a high energy resolution (see later) together with a counting rate capability in excess of 1 MCounts/s, with negligible fraction of pile up events. The latter is a specific requirement of NES of fusion plasmas in order to achieve good time resolutions during a plasma discharge.[22] The SD was exposed to neutrons

Note: Contributed paper, published as part of the Proceedings of the 21st Topical Conference on High-Temperature Plasma Diagnostics, Madison, Wisconsin, USA, June 2016.

a)Author to whom correspondence should be addressed. Electronic mail: giacomelli@ifp.cnr.it

b)See the Appendix of F. Romanelli *et al.*, Proceedings of the 25th IAEA Fusion Energy Conference 2014, Saint Petersburg, Russia.

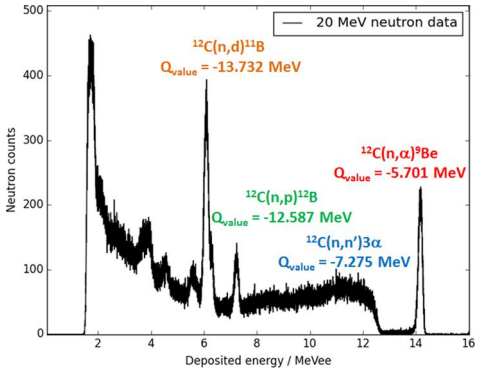

FIG. 1. 20 MeV neutron SD PHS at 0° at the Van de Graaf accelerator.

in the energy range of 14-20 MeV created by 3.3 MeV deuterons on a tritiated titanium target at different angles. High count rate measurements were obtained by placing the SD very close to the target but affecting the accuracy on the angle determination. The recorded pulse height spectrum (PHS) in Fig. 1 for the case of E_n = 20 MeV neutrons at 0° shows, among several other features, a well separated peak at about $E_{dep} = E_n - 5.7$ MeV deposited energy, due to the reaction ^{12}C(n, α)^{9}Be, which can be directly used for neutron spectroscopy of 14 MeV DT neutrons.

The impinging neutron spectrum at the SD position has been calculated by modeling the target (geometry and materials) and the beam-target reactions with the code TARGET.[23] Results show that for E_n = 20.0 MeV neutrons, the neutron beam mean energy has a Doppler shift of 119 keV. This value should be compared with the 174 keV full width at half maximum (FWHM) broadening measured for the ^{12}C(n, α)^{9}Be peak (see Fig. 2). By convolving the simulated incoming neutron spectrum with the SD response function approximated with a Gaussian of broadening W (expressed in keV), it results in W = 132 keV which makes it possible to estimate the SD energy resolution $\eta = W/E_n = 0.93\%$.[24] Similar W values are found for the other measured neutron energies, which indicates that the main contribution to the resolution comes from the electronic noise of the electronic chain, mainly the fast spectroscopy preamplifier. The SD was installed at the JET in October 2015 and has been operational in D plasma experiments.[25]

The theoretical response of this SD to 0.1-18.2 MeV neutrons has been obtained with the code MCNPX.[26] To verify their effects, different cross section libraries, namely, the Evaluated Nuclear Data File (ENDF/BVII.1),[27] the Fusion Evaluated Nuclear Data Library (FENDL-3),[28] and the Talys Evaluated Nuclear Data Library (TENDL-2014)[29] were used in the calculations. Comparison for neutrons of E_n = 14.0 MeV (see Fig. 3) shows that the ^{12}C(n, α)^{9}Be peak is at $E_{dep} = E_n - Q_{value}$ = 8.3 MeVee and it is the same for the three libraries. The spectral region of E_{dep} < 7.0 MeVee instead features differences with the largest in magnitude for ENDF/BVII.1. For larger neutron energies, i.e., E_n > 15.7 MeV, the discrepancies affect also the ^{12}C(n, α)^{9}Be peak region.

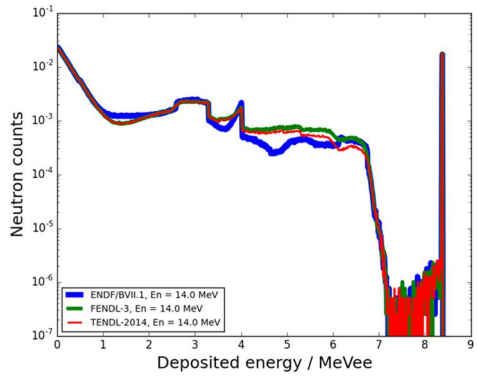

FIG. 3. Comparison of the 14.0 MeV neutron spectra calculated with MCNPX using three different cross section libraries.

With this theoretical result, the SD response function[30] has been then determined considering the measurements at the Van de Graaff accelerator[20,21] to define the SD resolution function $\eta = f(E_{dep})$. For this the 2.5 MeV neutron PHS from 3.3 MeV protons on the tritiated titanium target was also analyzed.[22] It features a plateau up to a shoulder about E_{dep} = 0.7 MeVee which corresponds to the maximum energy ^{12}C deposits in the SD after the elastic collision with a backscattered neutron from the beam. Modeling this shoulder as a Gaussian convolved step function, it results W = 99 keV broadening which is consistent with Ref. 22 although pursued with a different method. This W contribution combined with 38 keV broadening of the TARGET[23] incoming 2.5 MeV neutron beam indicates that the SD features η = 13% at this neutron energy. The SD resolution function has been then determined as $\eta = f(E_{dep}) = 0.093 E_{dep}^{-1}$ for $E_{dep} \leq 1.0$ MeVee and $\eta = 0.132 E_{dep}^{-1}$ for $E_{dep} > 1.0$ MeVee, respectively, in view of the two SD electronic setups (preamplifiers and amplifiers) implemented for 2.5 MeV D and 14 MeV DT neutron measurements at JET.[22,25] Fig. 4 displays the SD response function obtained by convolving $\eta = f(E_{dep})$ with the MCNPX response for FENDL-3.

Considering now the SD response to E_n = 14.0 MeV neutrons, the SD detection efficiency is about 1% of the incoming neutrons in the entire PHS of which 1.5% in the ^{12}C(n, α)^{9}Be peak with η = 1.6% (from Fig. 4). To date, for comparison, the most important NES results in DT plasmas were obtained with a magnetic spectrometer of ~3% energy resolution and ~10^{-5} detection efficiency, although with a wider dynamic range and better sensitivity to weak spectral components.[2]

The SD PHS corresponding to 14 MeV DT neutrons has been then used to assess the SD capability as a high resolution neutron spectrometer for studying fast ions in DT fusion plasmas subjected to NBI auxiliary heating.[31]

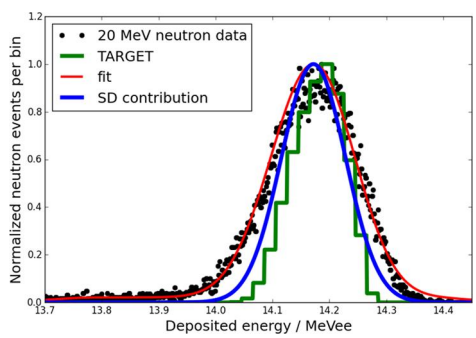

FIG. 2. Detail of Fig. 1: Fit (red line) of the ^{12}C(n, α)^{9}Be peak with a FWHM = 174 keV as a result of the convolution of a Gaussian (blue line), which mimic the SD response function, with E_n = 20 MeV TARGET neutrons.

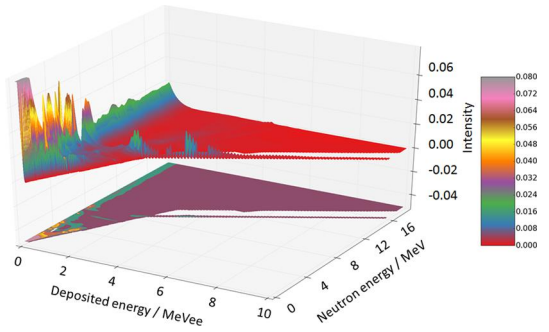

FIG. 4. SD response function for 0.1-18.2 MeV neutrons for SD dimensions of $4.5\times4.5\times0.5$ mm^3.

III. ANALYSIS OF THE NEUTRON EMISSION FROM NBI FAST IONS IN DT PLASMAS

Operations at ITER[32,33] towards high performance rely on the good confinement and classical slowing down of the neutral beam ions. These are essential for heating and fueling purposes and to sustain the plasma discharge. Experiments on mid-size tokamaks have shown that, under some circumstances, intrinsic and extrinsic processes can lead to deviations from the expected classical behavior. An example of the former processes are magnetic islands, that lead to enhanced diffusion of the beams well before the flux surfaces are destroyed and the field lines become stochastic.[34] Among the extrinsic processes, we especially recall resonant magnetic perturbations (RMPs) that are planned to mitigate edge localized modes at ITER, allowing for tolerable first wall loads in steady state operations. RMP can however cause distinctive additional losses of the beam ions that need to be monitored.[35]

While in mid-size machines fast ion loss detectors (FILDs) are the reference diagnostics to understand the behavior of the beam ions, the situation in large size, high power tokamaks, such as JET or ITER, is different. Here, FILD find some limitations, both due to the more limited fraction of ions that get lost in these machines and because of some practical constraints (e.g., high heat loads) that are common to the actual implementation of all edge probes. There is some evidence that the neutron emission spectrum is also modified when beam ions are lost from the plasma which requires a rather dramatic change in the measured spectrum to be detected by the present neutron spectrometers, which have, at their best, a resolution of the order of 2.5% around 14 MeV. We here suggest instead that, thanks to their enhanced energy resolution (~1% at 14 MeV), this limitation may be overcome with super resolution SDs, making NES a useful probe of the non-classical slowing down of the beam ions in high performance tokamaks. In order to quantitatively support this argument, we have considered the analytical model of Gaffey[36] that describes the evolution of the distribution function $f_b(v)$ of a beam of ions with initial velocity v_b, and in which we have added an "anomalous," albeit simplistic, loss term L(f) of the form

$$L(f) = \frac{f_b}{k\tau_s}\left(\frac{v_b}{2v}\right)^{\alpha} = \frac{f_b}{\tau_a(v)}, \tag{1}$$

where τ_s is the Spitzer slowing down time. The characteristic time scale of the anomalous losses, say τ_a, is given by $k = \tau_a/\tau_s$ at $v = v_b/2$. The exponent α controls the effect of the losses on ions of different energies. When $\alpha < 0$, ions with velocities $v > v_b/2$ are lost preferentially. By expanding $f_b(v)$ in terms of Legendre polynomials $P_l(\xi)$ as in Ref. 36, i.e.,

$$f_b(v) = \sum_{l=0}^{+\infty} f_l(v) P_l(\xi) \tag{2}$$

where l is an integer and ξ indicates pitch, we find that the coefficients $f_l(v)$ satisfy

$$\frac{df_l}{dv} + \frac{(3v^3 - Z_2/2l(l+1)v_c^3 - \frac{\tau_s v^3}{\tau_a(v)})}{v(v^3+v_c^3)} f_l = 0, \tag{3}$$

where the critical velocity v_c and effective charge Z_2 are defined as in Ref. 36. If we assume that all beam ions start at a pitch ξ_b and have initial velocity v_b, $f_l(v)$ must satisfy the boundary condition

$$f_l(v = v_b) = \frac{1}{v_b^3 + v_c^3}\frac{\tau_s}{2}(2l+1)S_0 P_l(\xi_b) \tag{4}$$

where S_0 is the number of (ions/m^3)/s that are injected. We now observe that Equation (3) is an ordinary differential equation subject to the initial condition (4) and that can be solved by standard numerical techniques.

Fig. 5 shows $f_b(v)$ as obtained from (2)–(4) for a typical JET NBI scenario of tritons with $E_b = 0.5mv_b^2 = 120$ keV and $\xi_b = 0.5$ in a DT plasma. The classical solution in panel (a) is compared to the cases when $\alpha = -4$ and $k = 0.5$ and 0.25 in panels (b) and (c), respectively. The Monte Carlo code GENESIS[37] has been used to calculate the corresponding normalized neutron spectra as displayed in panel (d). Here we observe that, depending on the extent of the anomalous losses, there is indeed a measurable change in the neutron spectrum which requires a high resolution instrument, such as an SD, to fully appreciate the effect. Together with lower neutron yields, anomalous transport affects the neutron spectrum for $E_n < 14$ MeV where different shapes are visible with respect to the classical slowing down distribution due to fast ions losses. To verify the capability of the super-resolution SD neutron spectrometer to recognize such details of Fig. 5(d), these neutron spectra were folded with the SD response function of Fig. 4 to determine the corresponding PHS SD would measure. The results are presented in Fig. 6 in terms of ^{12}C(n, α)^{9}Be peak containing 10^4 and 10^5 counts, respectively.

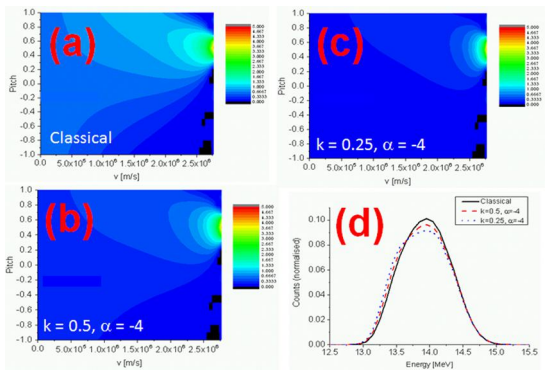

FIG. 5. Calculations of the slowing down distributions of NBI tritons in a DT plasmas using both classical (a) and "anomalous" models with (k, α) = (0.5, –4) (b) and (0.25, –4) (c), respectively. The corresponding effects on the shape of the normalized neutron spectrum are highlighted in (d).

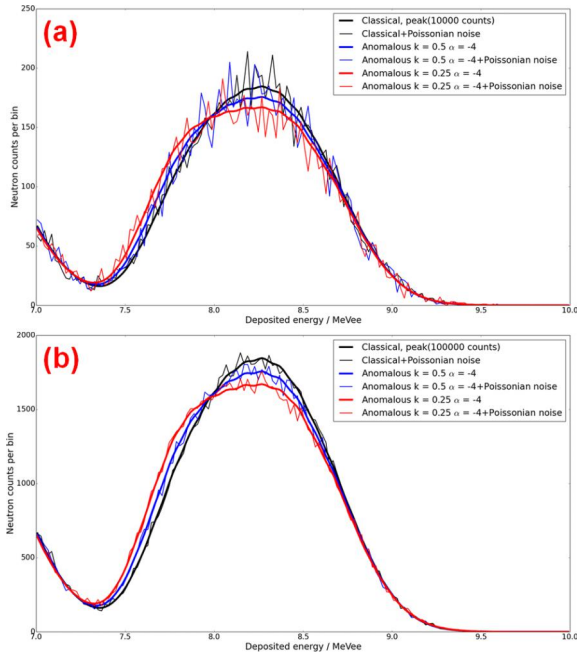

FIG. 6. Comparison of SD PHS with 10^4 and 10^5 counts in the $^{12}C(n,\alpha)^9Be$ peak positioned at about $E_{dep} = 8.3$ MeVee for the neutron spectra shown in Fig. 5(d). Poissonian statistics has been added to mimic real experimental data.

Poissonian counting statistics has been taken into account to mimic real experimental data. For 14 MeV DT neutrons SD features about 1.5% neutron detection efficiency in $^{12}C(n,\alpha)^9Be$ peak although its very small dimensions of $4.5 \times 4.5 \times 0.5$ mm^3. Applying an 1 MeVee data acquisition (DAQ) threshold for dedicated 14 MeV neutron measurements of DT plasmas, the super-resolution of the SD would allow for good statistics in 1 s acquisition time at 0.3 MCounts/s which is achievable in view of the >1 MCounts/s capability of the DAQ system implemented in the SD setup. With our simplified model, we have found that changes in the neutron spectrum are more pronounced for small k and negative α. Little to no changes are observed in the spectrum when $\alpha > 0$, i.e., when the slower ions are preferentially lost, for example, as a result of micro-turbulence which is thought to play a minor role on energetic ion transport.[38]

As DT plasma diagnostic, SDs need to operate in stable conditions, namely, avoiding polarization effects,[15] which can be mitigated/avoided in operational conditions by inverting the applied high voltage. Moreover, the SDs physical properties of resilience at high temperatures and insensitivity to magnetic fields make the SDs a valuable candidate as high resolution neutron spectrometer for present and future nuclear fusion facilities as ITER and DEMO.[39]

IV. CONCLUSIONS

In this paper we have presented measurements of the response of single crystal diamond detectors to quasi-monoenergetic neutrons in the range 14–20 MeV. The results show that an energy resolution of 1% together with a detection efficiency of about 1% can be achieved. This opens up to new routes for fast ion physics studies in high performance fusion devices. SD potentials in DT plasmas have been addressed, especially for neutron spectrum measurements in discharges heated by neutral beam injection.

ACKNOWLEDGMENTS

This work has been carried out within the framework of the EUROfusion Consortium and has received funding from the Euratom research and training programme 2014-2018 under Grant Agreement No. 633053. The views and opinions expressed herein do not necessarily reflect those of the European Commission.

[1]J. Scott McCauley and J. D. Strachan, Rev. Sci. Instrum. **63**, 4536 (1992).
[2]G. Ericsson *et al.*, Rev. Sci. Instrum. **72**, 759 (2001).
[3]E. Andersson Sundén *et al.*, Nucl. Instrum. Methods Phys. Res., Sect. A **610**, 682–699 (2009).
[4]M. Gatu Johnson *et al.*, Nucl. Instrum. Methods Phys. Res., Sect. A **591**, 417–430 (2008).
[5]L. Giacomelli, A. Zimbal, K. Tittelmeier, H. Schuhmacher, G. Tardini, and R. Neu, Rev. Sci. Instrum. **82**, 123504 (2011).
[6]See http://www.efda.org/jet/ for JET tokamak.
[7]H. Henriksson, S. Conroy, G. Ericsson, L. Giacomelli, G. Gorini, A. Hjalmarsson, J. Källne, M. Tardocchi, and M. Weiszflog, Plasma Phys. Controlled Fusion **47**, 1763–1785 (2005).
[8]M. Tardocchi *et al.*, Rev. Sci. Instrum. **77**, 126107 (2006).
[9]C. Hellesen *et al.*, Rev. Sci. Instrum. **79**, 10E510 (2008).
[10]L. Giacomelli *et al.*, Rev. Sci. Instrum. **79**, 10E514 (2008).
[11]L. Giacomelli *et al.*, Phys. Procedia **62**, 124–128 (2015).
[12]A. Zimbal, L. Giacomelli, R. Nolte, and H. Schuhmacher, Radiat. Meas. **45**, 1313–1317 (2010).
[13]L. Giacomelli *et al.*, Nucl. Phys. B, Proc. Suppl. **215**, 242–246 (2011).
[14]M. Rebai *et al.*, Nucl. Phys. B, Proc. Suppl. **215**, 313–315 (2011).
[15]M. Rebai *et al.*, J. Instrum. **7**, C05015 (2012).
[16]C. Cazzaniga *et al.*, Rev. Sci. Instrum. **85**, 11E101 (2014).
[17]C. Cazzaniga *et al.*, Rev. Sci. Instrum. **85**, 043506 (2014).
[18]M. Nocente, C. Cazzaniga, M. Tardocchi, F. Binda, J. Eriksson, L. Giacomelli, A. Muraro, M. Rebai, S. Sharapov, and G. Gorini, Rev. Sci. Instrum. **86**, 103501 (2015).
[19]A. V. Krasilnikov, E. A. Azizov, A. L. Roquemore, V. S. Khrunov, and K. M. Young, Rev. Sci. Instrum. **68**, 553 (1997).
[20]J. Y. Wang, L. H. Gong, X. J. Yang, J. H. Gong, and X. C. Lu, http://en.cnki.com.cn/Article_en/CJFDTOTAL-YZJS2008S1049.htm.
[21]X. Yuan, X. Zhang, X. Xie, G. Gorini, Z. Chen, X. Peng, J. Chen, G. Zhang, T. Fan, and G. Zhong, J. Instrum. **8**, P07016 (2013).
[22]M. Rebai *et al.*, "Response function of single crystal synthetic diamond detectors to 1-4 MeV neutrons for spectroscopy of D plasmas," Rev. Sci. Instrum. (these proceedings).
[23]D. Schlegel, Target User's Manual, PTB-6.42-05-2, PTB, Braunschweig, 2005.
[24]T. Shimaoka *et al.*, Rev. Sci. Instrum. **87**, 023503 (2016).
[25]A. Muraro *et al.*, "First neutron spectroscopy measurements with a pixelated diamond detector at JET," Rev. Sci. Instrum. (these proceedings).
[26]See http://mcnpx.lanl.gov/ for MCNPX simulation program.
[27]See http://www.nndc.bnl.gov/endf/b7.1/ for ENDF/BVII.1 library.
[28]See https://www-nds.iaea.org/fendl3/ for FENDL-3.
[29]See http://www.talys.eu/tendl-2014/ for TENDL-2014.
[30]M. Rebai, A. Milocco, L. Giacomelli, E. Perelli Cippo, M. Tardocchi, A. Fazzi, A. Pietropaolo, and G. Gorini, J. Instrum. **8**, P10007 (2013).
[31]M. Nocente *et al.*, Nucl. Fusion **54**, 104010 (2014).
[32]See https://www.iter.org/ for ITER project.
[33]M. Sasao, T. Nishitani, A. Krasilnilov, S. Popovichev, V. Kiptily, and J. Källne, Fusion Sci. Technol. **53**, 604 (2008), http://www.ans.org/pubs/journals/fst/a_1681.
[34]M. García-Muñoz, P. Martin, H.-U. Fahrbach, M. Gobbin, S. Günter, M. Maraschek, L. Marrelli, and H. Zohm, Nucl. Fusion **47**, L10 (2007).
[35]M. Garcia-Munoz *et al.*, Nucl. Fusion **53**, 123008 (2013).
[36]J. D. Gaffey, J. Plasma Phys. **16**, 149 (1976).
[37]M. Tardocchi *et al.*, Phys. Rev. Lett. **107**, 205002 (2011).
[38]D. C. Pace *et al.*, Phys. Plasmas **20**, 056108 (2013).
[39]See http://www.ipp.mpg.de/16355/demo for DEMO project.

Paper VI

IOP Publishing Measurement Science and Technology
Meas. Sci. Technol. **00** (2018) 000000 (9pp) UNCORRECTED PROOF

Neutron spectroscopy measurements of 14 MeV neutrons at unprecedented energy resolution and implications for deuterium–tritium fusion plasma diagnostics

D Rigamonti[1,2], L Giacomelli[2], G Gorini[1,2], M Nocente[1,2], M Rebai[1,2], M Tardocchi[2], M Angelone[3], P Batistoni[3], A Cufar[4], Z Ghani[5], S Jednorog[6], A Klix[7], E Laszynska[6], S Loreti[3], M Pillon[3], S Popovichev[5], N Roberts[8], D Thomas[8] and JET Contributors[10]

[1] Dipartimento di Fisica 'G. Occhialini', Università degli Studi di Milano-Bicocca, Milano, Italy
[2] Istituto di Fisica del Plasma 'P. Caldirola', CNR, Milano, Italy
[3] ENEA, I-00044 Frascati, Rome, Italy
[4] Jozef Stefan Institute, Jamova cesta 39, 1000, Ljubljana, Slovenia
[5] CCFE, Abingdon, Oxon, OX14 3DB, United Kingdom
[6] Institute of Plasma Physics and Laser Microfusion, Hery 23, 01-497 Warsaw, Poland
[7] Karlsruhe Institute of Technology, 76344 Eggenstein-Leopoldshafen, Karlsruhe, Germany
[8] National Physical Laboratory, Teddington, TW11 OLW, United Kingdom
[9] EUROfusion consortium, Culham Science Centre, Abington, United Kingdom AQ1

E-mail: davide.rigamonti@mib.infn.it AQ2

Received 7 November 2017, revised 8 January 2018
Accepted for publication 10 January 2018
Published

Abstract

An accurate calibration of the JET neutron diagnostics with a 14 MeV neutron generator was performed in the first half of 2017 in order to provide a reliable measurement of the fusion power during the next JET deuterium–tritium (DT) campaign. In order to meet the target accuracy, the chosen neutron generator has been fully characterized at the Neutron Metrology Laboratory of the National Physical Laboratory (NPL), Teddington-UK. The present paper describes the measurement of the neutron energy spectra obtained by using a high resolution single-crystal diamond detector (SCD). The measurements, together with a new neutron source routine 'ad hoc' developed for the MCNP code, allowed the complex features of the neutron energy spectra resulting from the mixed D/T beam ions interacting with the T/D target nuclei to be resolved for the first time. From the spectral analysis a quantitative estimation of the beam ion composition has been made. The unprecedented intrinsic energy resolution (<1% full width at half maximum (FWHM) at 14 MeV) of diamond detectors opens up new prospects for diagnosing DT plasmas, such as, for instance, the possibility to study non-classical slowing down of the beam ions by neutron spectroscopy on ITER.

Keywords: neutron spectroscopy, diamond detectors, plasma diagnostics, 14 MeV neutron generator

AQ3 (Some figures may appear in colour only in the online journal)

AQ14 [10] See the author list of [23].

JNL:MST PIPS: AAA675 TYPE: PAP TS: NEWGEN DATE:18/1/18 EDITOR: IOP SPELLING: UK

1. Introduction

The Joint European Torus (JET) is the largest experimental fusion device in the world and currently is the only one that can operate with tritium. It is equipped with several neutron diagnostics [1], in particular fission chambers (KN1) and in-vessel activation system (KN2), both able to measure the absolute neutron emission rate over the whole range from 10^8 n s^{-1} up to 10^{19} n s^{-1} in deuterium–tritium (DT) plasma scenarios. An accurate calibration of both KN1 and KN2 with 14 MeV neutrons is needed in order to provide reliable measurements of the neutron yield and of the fusion power during the next DT campaign planned in 2019 [2]. The neutron calibration consists in placing a neutron source of known intensity and energy spectrum at different positions inside the tokamak vessel and recording the KN1 and KN2 signals. The chosen neutron source was a 14 MeV neutron generator (NG) type ING-17 provided by VNIIA [3]. Two nominally identical neutron generators (NG#1 and NG#2) have been procured to mitigate the risk of failure. In the NGs, a mixed $D_x^+/T_x^+/D_xT_y^+$ beam (nominally 50–50%, $x, y = 1, 2$) is accelerated at a nominal energy of 100 keV onto a titanium target containing T/D (nominally 50–50%) inside a sealed tube. The NG thus produces 14 MeV neutron beam-target fusion reactions [4].

In order to meet the calibration target accuracy of 10% on KN1 and KN2, the two NGs have been fully characterized and calibrated at the Neutron Metrology Laboratory of the National Physical Laboratory (NPL, Teddington, UK). Two experimental campaigns were performed in November 2015 and June 2016 and aimed at determining the neutron emission rate and spectrum as a function of the angle of observation for both NGs. The NGs were placed at the centre of the low-scatter area of the accelerator hall which is equipped with rotating arms so that simultaneous measurements with several types of detectors at different angles with respect to the NG are possible. In this experiment a liquid scintillator detector (NE213), a long counter, activation foils and single crystal diamond detectors were used. The whole calibration and characterization campaign is described in [4].

For carrying out the data analysis and to simulate the NG neutron emission spectra a neutron source routine has been developed with the MCNP code [5] version 6. The MCNP code describes in detail the geometry of the neutron generator and simulates the neutron spectra resulting from all possible reactions occurring between the D/T (mono-atomic, bi-atomic etc) ions in the beam and the TiT/D target [6].

The present paper describes the neutron energy spectra obtained by employing high resolution SCD neutron spectrometers. For the first time, we demonstrate the capability to accurately determine the detailed ion composition of the beam. This is made possible by exploiting the instrument's high energy resolution to discriminate the different reaction components that make up the whole neutron spectrum and that come from reactions between mixed D/T beam ions and T/D nuclei in the target. The result opens up new prospects for beam ion studies, and in general for neutron spectroscopy studies, in DT plasmas. An example that we have studied regards to the possibility of observing non classical beam slowing down in current drive studies at ITER using neutron spectroscopy.

2. Experimental setup and calibration procedure

2.1. Single crystal diamond detector

Artificial chemical vapour deposition SCD detectors have shown excellent performances in fast neutron spectroscopy due to their high energy resolution, fast time response and high radiation hardness [7–10] and are now being exploited for measurements of the 2.5 MeV neutron spectrum in deuterium plasmas at JET [11, 12]. Neutron detection in SCD is based on the collection of the electron–hole pairs generated by the slowing down of the charged particles produced by the interactions between neutrons and carbon nuclei. For 14 MeV neutrons the main reaction channels of interest are: elastic and inelastic scattering ^{12}C(n,n')^{12}C which features the highest cross section and gives rise to a continuum in the measured pulse height spectrum (PHS); the n-3α reaction ^{12}C(n,n')3α with a Q_{value} of -7.23 MeV; and the n-α reaction ^{12}C(n,α)^{9}Be with a Q_{value} of -5.702 MeV. The latter is the best candidate reaction for 14 MeV neutron spectroscopy, as it leads to a well-defined peak centred at $E_{\text{dep}} = E_{\text{n}} - 5.702$ MeV which provides a univocal one to one relation between incoming neutron energy and measured deposited energy. The shape of this peak is due to two independent contributions, namely the broadening due to the intrinsic resolution of the SCD itself and an additional kinematic broadening that depends on the energy distribution of the incoming neutron beam around 14 MeV. When the kinematic contribution dominates over the intrinsic broadening the shape of this peak becomes a diagnostic of the incoming 14 MeV neutron energy spectrum. The SCD neutron spectrometer used in these measurements was designed and built by the CNR-ISM institute in Rome (Italy) and is made of an artificial single-crystal chemical vapour deposition diamond sample ($4.5 \times 4.5 \times 0.5$ mm^3) grown by Element Six Ltd [13]. The Ohmic contacts on the top and bottom surfaces were obtained by subsequent sputtering deposition of a multilayer metal structure (patent pending), followed by a final gold layer deposition. In figure 1, the SCD is shown together with the dedicated 1 mm thick alumina printed circuit board (PCB) and the aluminium metal case. The latter is needed to shield the detector from electromagnetic interferences and to provide mechanical protection.

A dedicated custom electronic chain was used for these measurements (see figure 2). The detector was coupled to a CIVIDEC C6 fast charge preamplifier [14], which features a rise time of 3.5 ns and a shaping time of 25 ns. The preamplifier, supplied with a 12 V DC power supply has a bias current of 25 mA, a gain of 6 mV fC^{-1} and a bandwidth of 100 MHz. A CAEN [15] high voltage supply model NDT1470 was used to supply a voltage of $+400$ V to the detector, which corresponds to an average electric field of 0.8 V μm^{-1} in the bulk material. In some measurements, instead of the C6 model, a CIVIDEC CX preamplifier optimized for high resolution spectroscopy was used. The latter has a rise time of 80 ns, a shaping time of 180 ns and a gain of 12 mV fC^{-1}. The preamplifier output

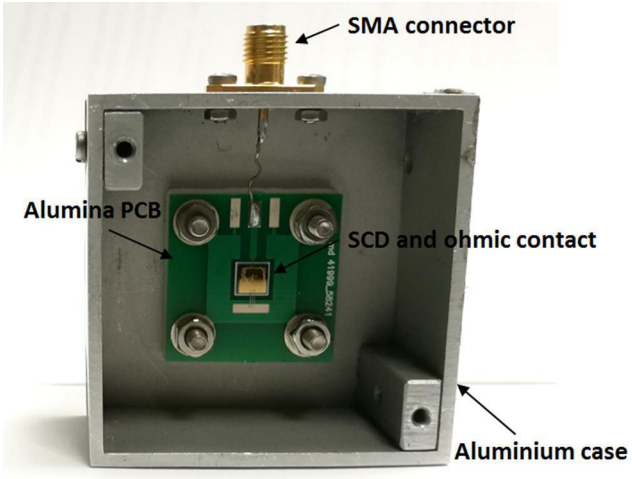

Figure 1. Picture of the SCD detector.

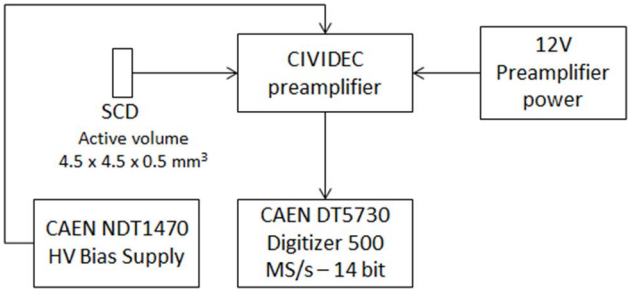

Figure 2. Scheme of the SCD electronic chain.

was fed to an 8-channel waveform digitizer, CAEN DT5730. This is a 14 bit and 500 MSamples s^{-1} rate digitizer equipped with CAEN software able to perform on-line measurements of the pulse area, by integrating each signal in a user defined gate, namely 40 ns for the C6 preamplifier and about 700 ns for the CX preamplifier. In some cases, the analog signal produced as output of the preamplifier was duplicated by a linear Fan-In Fan-Out module and simultaneously acquired with two different digitizers. The first was configured to digitize the full waveform corresponding to each detection event for offline analysis, while the second digitizer was set to process online each pulse from the detector, so to obtain energy/time list mode data.

The detector was placed on a rotating arm at different distances and angles to characterise the neutron energy emission spectra of the NGs.

2.2. Calibration procedure

Initially, the SCD was calibrated in the laboratory in vacuum with a ^{241}Am electro-deposited source which emits α particles with three different energies (5.486, 5.442, 5.388 MeV) with branching ratio (84.5%, 13.06%, 1.62%, respectively). On site, during the experiment, the calibration was verified with ^{241}Am electro-deposited source in air and correction factors due to the alpha particle energy loss in air were calculated and applied. The dominant factors that affect the accuracy of the α calibration in vacuum are connected to the energy straggling of the α particles in the materials before reaching the active part of the detector, namely the Ohmic contacts of the diamond. It was found that the uncertainties in the knowledge of the SCD contact thicknesses limit the accuracy in the calibration to a few tens of keV, which is not sufficient for a detailed data analysis. For this reason, an iterative Bayesian calibration method based on prior assumptions has been implemented and is described below.

At the time of the measurements, the NG specifications provided by the supplier refer to a D/T mixture in the beam and in the target with nominal concentration at 50–50%. Instead, it was observed that D^+, T^+, D_2^+, T_2^+, DT^+, species were present in the beam, resulting in up to six observed different NG neutron energy distributions. This is due to the different kinetic energy of the species when they reach the T/D target. D^+ and T^+ ions are accelerated by the nominal NG operational voltage V_{op}. D_2^+ and T_2^+ molecules are accelerated by the same voltage and the individual atoms thus have half of the energy each. Finally, DT^+ ions split into a D^+ and a T^+ ions having 2/5 and 3/5 each of total energy, respectively. For this reason, a neutron source routine was developed in MCNP together with the detailed model of the generator [6, 16], producing the six neutron energy spectra resulting from all possible reactions occurring with the D/T ions in the beam impinging on the TiT/D target.

In previous experiments [7–9], the SCD was characterized, namely its resolution was measured at a neutron source to be equal to 120 keV FWHM at 14 MeV for the n-α reaction $^{12}C(n,\alpha)^9Be$. In the case of the NG neutron calibration, the expected SCD pulse height spectra were thus obtained convoluting the simulated six neutron energy spectra with a Gaussian-shaped SCD response function of FHWM equal to 120 keV (as shown in figure 4). We observe that the six simulated neutron components provide pulse height spectra that cover deposited energy from 8.4 to 9.2 MeV. AQ4

The iterative Bayesian calibration method was performed on the neutron data recorded at zero degrees with respect to the beam direction. Zero degrees is the best angle since, due to the reaction kinematics, the six different neutron energy components are better separated in energy (see section 3.1). Furthermore, at zero degrees, the neutron energy uncertainty due to the angular uncertainty of the experimental setup is minimized due to neutron energy dependence on the cosine of the emission angle. The observed PHS (see figure 5 left) recorded at zero degrees features a complex shape in which the structures are due to three main reactions in ^{12}C: elastic scattering, $^{12}C(n,n')3\alpha$ and $^{12}C(n,\alpha)^9Be$. The most energetic peak (see figure 5 right) centred at ~8.8 MeV is due to the $^{12}C(n,\alpha)^9Be$ reaction and is the most useful one for neutron spectroscopy. We note that it features three characteristic structures caused by the different neutron energy components. The Bayesian calibration method we have used employs two calibration points to determine the relation between deposited energy and ADC channels. The first point is given by the neutron elastic scattering edge on ^{12}C which is at a well-defined position $E_{edge} = 0.284 * E_n$ while the second is obtained with *a priori* assumption on the first structure located at about 8.7

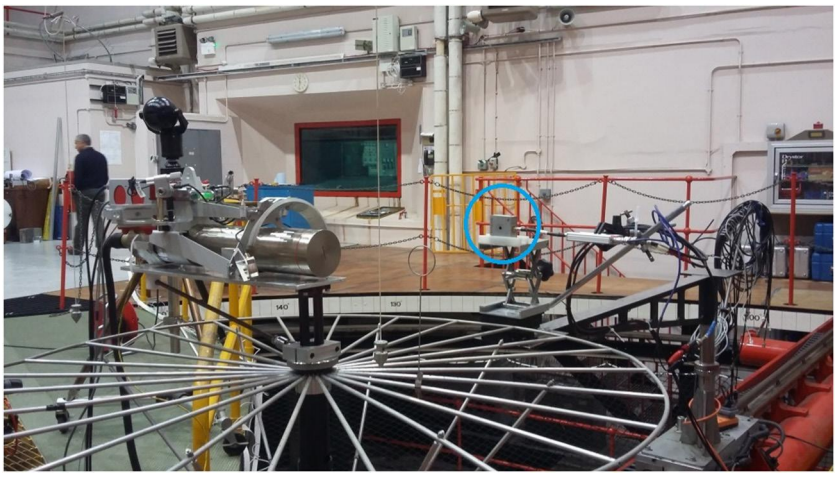

Figure 3. Experimental setup. The NG (on the left) is in the centre of a circular platform and the SCD (circled) at 90° with respect to the D/T beam direction in the NG.

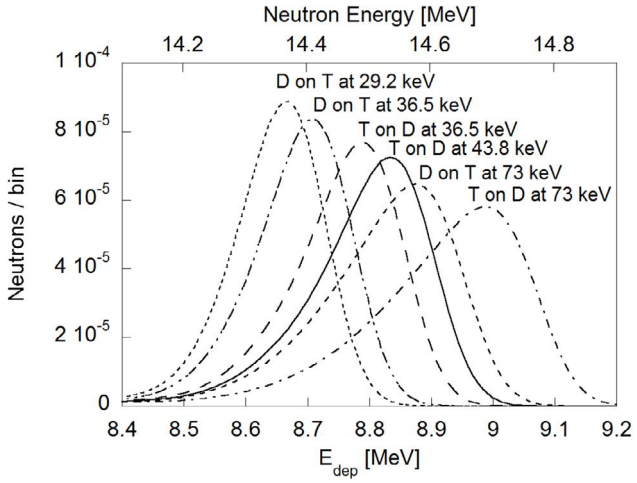

Figure 4. Theoretical normalized SCD pulse height spectra corresponding to each NG neutron emission component and resulting from the MCNP model. The SCD response function is assumed to be Gaussian-shaped of 120 keV FWHM. The lower *x*-axis represents the deposited energy inside the detector by neutrons. The upper *x*-axis represents the energy of the incoming neutrons.

MeV in the PHS spectrum. A calibration curve is so obtained and used in a numerical fit between measured data and the six MCNP simulated neutron energy spectral components. The method is repeated for different *a priori* assumptions and the best agreement was obtained when the first structure of the figure 5 right is associated to the combination of the first two peaks of the figure 4, namely D on T at 29.2 keV and D on T at 36.5 keV. Other assumptions on the first structure in the PHS provided significantly worse Chi-square value.

In order to validate the iterative calibration method, a consistency check with the α particles calibration performed on site during the measurement was done and indicates that they are in agreement within $\pm 5\%$ uncertainty (see figure 6). Moreover, a second independent consistency check of the iterative calibration is given by the comparison between the measurement carried out at nominally 90° with respect to the incoming NG beam and the MCNP simulations (see figure 7). In this case the six neutron components overlap due to the kinematics. It was found that the best agreement comes with the simulation at 84°, which is within the expected angular uncertainty due to the experimental-setup. We noted that on the low energy side of the peak of figure 7, the data show a low energy tail which does not overlap with the simulation. This is interpreted as due to neutron events that lead to a partial charge collection in the SCD.

3. Results and discussion

3.1. Study of the energy spectrum dependence on the emission angles

The SCD neutron spectrometer was placed on a rotating arm at different distances exploring the neutron energy spectrum dependence on the neutron emission angle for the NG. Neutron energy spectra have been recorded at different angles from 0 to 150° with respect to the beam direction. Figure 8 shows the anisotropy of the neutron emission intensity which is due to the reaction kinetics. The evaluation of the anisotropy profile of the neutron emission rate was a key aspect in the NG calibration in order to derive the total neutron emission in 4π. In particular, as shown in detailed in [4], the neutron emission rate as a function of the angle has been studied by using calibrated long counter detectors and activation foils. Furthermore, as shown in figure 8, the neutrons emitted at zero degrees exhibit a broader spectrum than at other angles, because of the reaction kinetics. In particular, the broadening of the spectra decrease from 0 to 90° and then it increases again from 90 to 150°. This is due to the six different neutron energy components which are well separated at zero degrees and overlap at 90°.

3.2. Analysis of the beam composition

The aim of the analysis is to resolve the complex features of the neutron energy spectra resulting from the mixed D/T beam ions reacting with the T/D nuclei present in the target. The analysis is based on the numerical fitting of the simulated neutron components resulting from the five ion species convolved

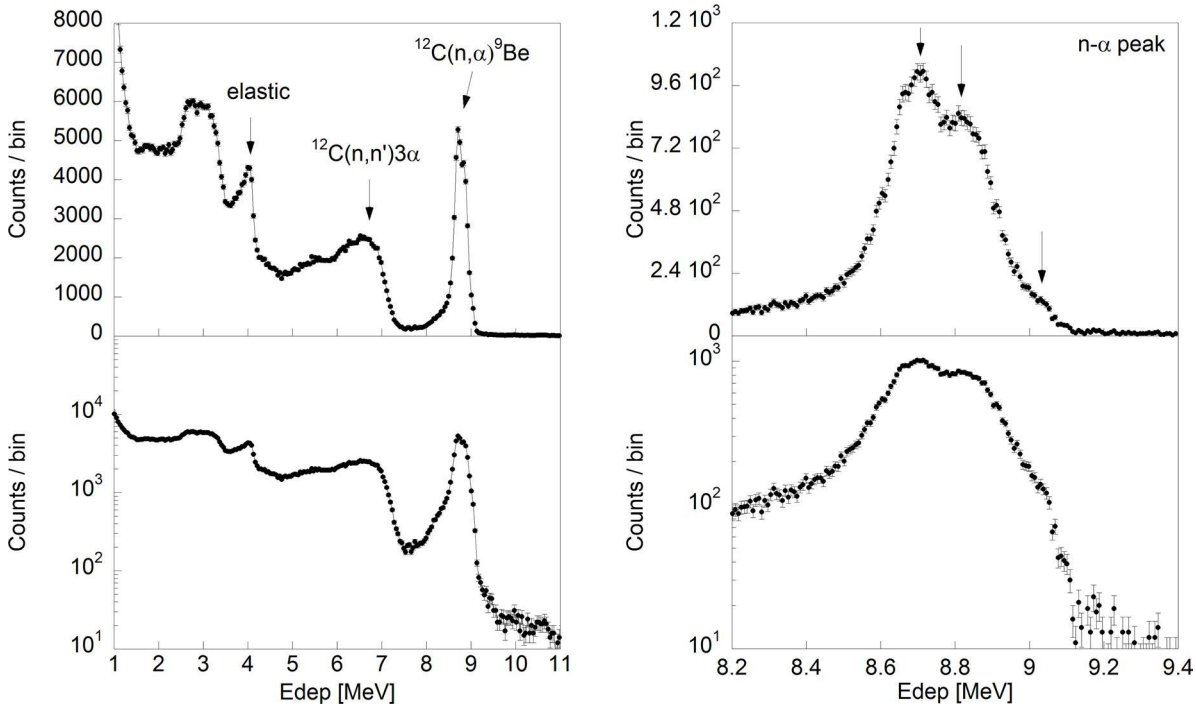

Figure 5. PHS recorded at zero degrees in linear scale (top-left) and logarithmic scale (bottom-left). The n-α peak is shown in detail in linear scale (top-right) and in logarithm scale (bottom-right). The arrows in the plot indicate the main structures in the PHS spectrum and the structures of the peak. $E_{\mathrm{peak}} = E_{\mathrm{n}} - 5.702$ MeV.

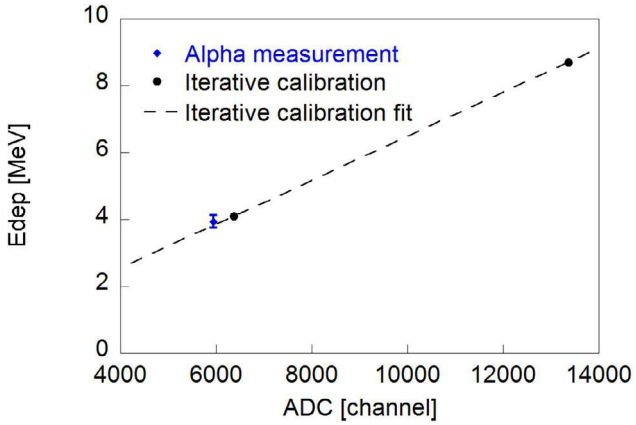

Figure 6. Calibration fit based on the iterative calibration process shown with the ^{241}Am calibration point.

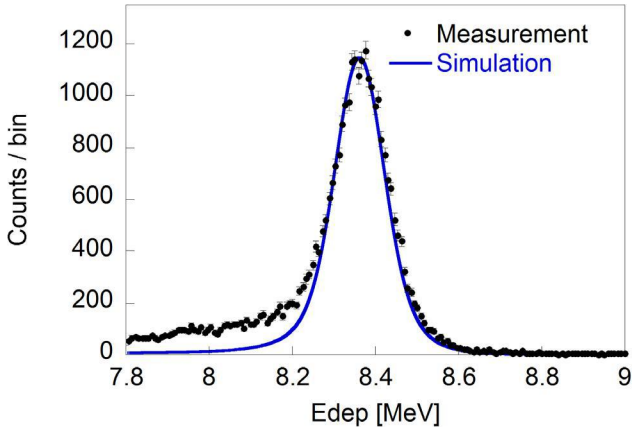

Figure 7. Comparison between the PHS measured at nominally 90° and the simulation at 84°.

with the SCD response function to the experimental data taken at zero degrees. In addition to the model components displayed in figure 4, an MCNP calculation [16] has been performed to determine the absolute neutron yield related to each component. Figure 9 shows the best 5-free parameters numerical fit of the data, together with the neutron contributions of the five ion species weighted to the neutron yield. Here the neutron components due to the reaction D on T at 29.2 keV and T on D at 43.8 keV (see figure 4) were added together and considered as a single DT component. The goodness of the fit is assessed on the reduced Chi-square value which results to be equal to 1.50. This indicates that the analysis model used for the data fit provides a good description of the SCD data. Looking at the figure 9, it can be noticed that the DT component is the dominant one and it is the one responsible for the '*double*' peak structure. The T component (T on D at 73 keV), instead, is the most energetic one and it is the only one that can describe the high energy tail of the peak. Table 1 summarizes the calculated neutron yields of each component and the estimated incident particle beam composition, respectively. The dominant fraction of the incident beam is represented by the DT molecules (~80.4%) followed by D_2 and T_2 molecules (~9% and 7.3% respectively), T ions (~2.7%) and finally by D ions (~0.6%). The errors in table 1 represent the statistical uncertainties of the parameters based on the covariance matrix resulting from the Chi-square minimization in the fit procedure and they include the effect of correlations with the other parameters. The analysis has been performed by using the software framework ROOT [17]. In figure 10 the fit results are shown together with the 95% of confidence interval of the fit.

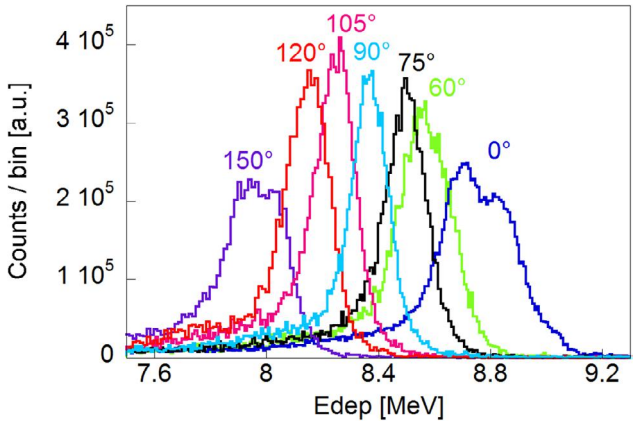

Figure 8. Recorded pulse height spectra measured by the SCD at different angles from 0 to 150°. The *x*-axis represents the deposited energy in detector.

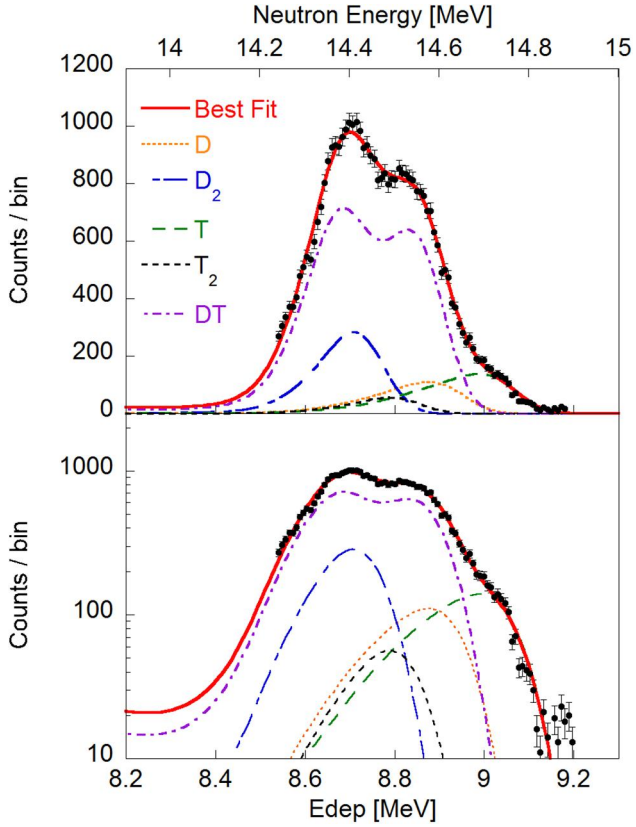

Figure 9. SCD PHS at 0° shown as black dots without the low energy tail due to partial charge collection (see text). The neutron beam components with their weights and their sum correspond to the best fit to the data. The lower *x*-axis represents the neutron deposited energy inside the detector while the upper *x*-axis represents the energy of the incoming neutrons. The *y*-axis of the graph in the top is given in linear scale, whereas in the bottom graph the *y*-axis is given in logarithmic scale.

These results demonstrate the capability of SCD to determine the beam composition in a mixed DT beam and could be applied on the neutral beams injected in thermonuclear fusion experiments. This was demonstrated in an earlier work [18], where the main features of the neutron spectrum have been observed on the JET tokamak with a mixed D/T beam used to heat the plasma.

Table 1. Summary of the neutron yields of each D/T beam component and the estimated incident particle beam composition derived by the best numerical fit.

Incident particle beam composition	Neutron yield	Concentration (%)
DT^+	2.60×10^{-7}	80.4 ± 6.1
D_2^+	2.79×10^{-6}	9 ± 0.9
T_2^+	6.59×10^{-8}	7.3 ± 2.5
T^+	1.37×10^{-6}	2.7 ± 0.2
D^+	3.85×10^{-6}	0.6 ± 0.1

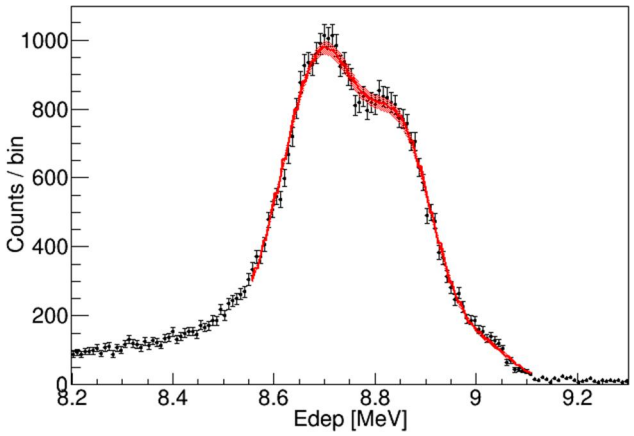

Figure 10. SCD PHS at 0° shown with the best fit of the data together with its 95% confidence interval (red band).

4. New prospects for diagnosing DT plasmas

The unprecedented intrinsic energy resolution <1% of diamond detectors for 14 MeV neutrons opens up new prospects for diagnosing DT plasmas as demonstrated with the detailed analysis of the NG D/T beam composition. In this work we also explore the possibility to use SCDs to study the non-classical slowing down of the beam ions in ITER DT plasmas. As in [8], where this phenomenon was studied for JET, here we apply the analytical formulas of Gaffey [19] to determine the steady-state distribution function $f_b(v)$ of a beam of neutral ions that slows down in an ITER DT plasma due to Coulomb collisions. Following [8], we also introduce a term $L(f)$ in Gaffey's equation which heuristically describes an additional, non-classical ('anomalous') loss mechanism acting on the beam ions. $L(f)$ is given by

$$L(f) = \frac{f_b}{k\tau_s}\left(\frac{v_b}{2v}\right)^{\alpha} = \frac{f_b}{\tau_\alpha(v)}. \qquad (4.1)$$

Here v_b and τ_s represent the initial velocity and the Spitzer slowing down time, respectively. For $v = v_b/2$, the velocity dependent slowing down time $\tau_\alpha(v)$ implied by equation (4.1) is equal to $k \cdot \tau_s$ and the magnitude of k determines the ratio between the classical and anomalous time scales. The exponent α, instead, controls the effect of the anomalous losses on

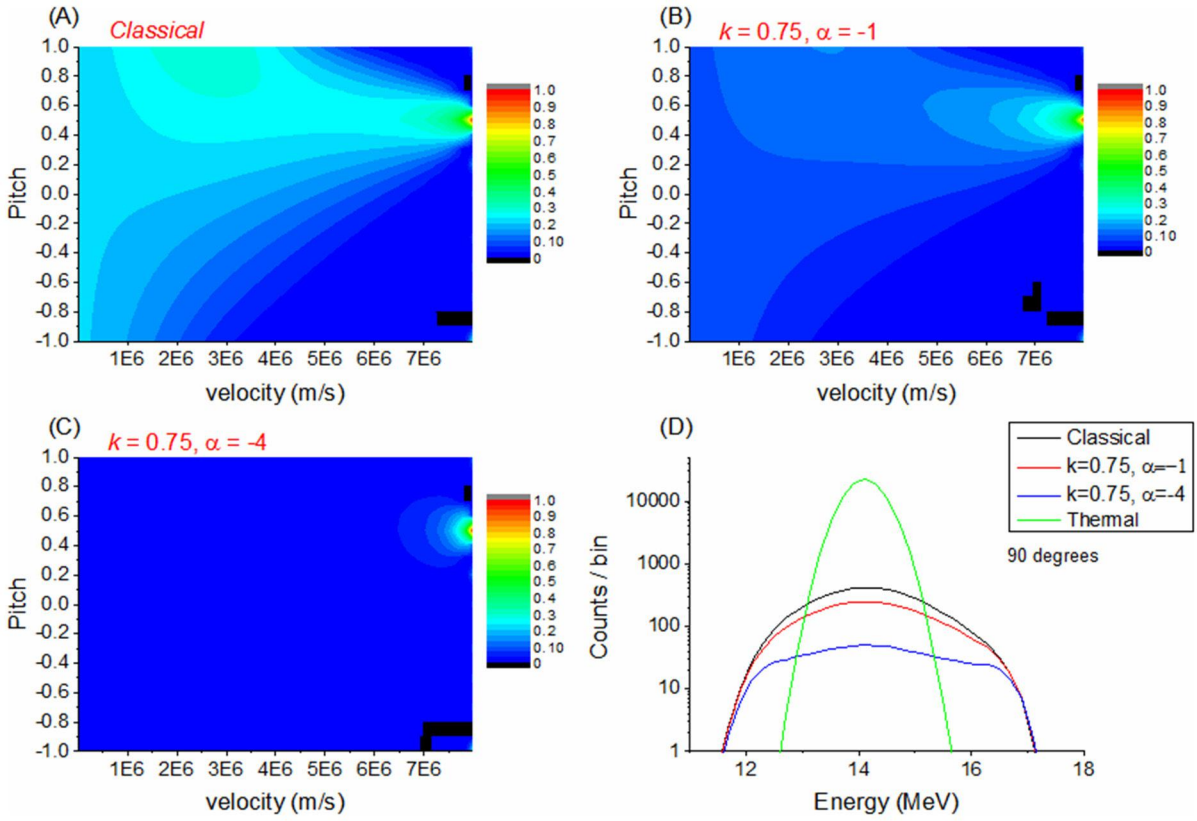

Figure 11. Calculations of the slowing down distributions of 1 MeV NB tritons in hypothetic DT plasma in ITER (ion temperature and electron temperature equal to 20 keV; deuterium and tritium densities equal to $1.0 * 10^{20}$ m^{-3}). The classical solution (A) is compared to the anomalous cases (B) and (C) with $k = 0.75$, $\alpha = -1$ and $k = 0.75$, $\alpha = -4$, respectively. In panel (D), the relative neutron energy spectra (viewed at 90°) generated by the NB tritons and the bulk thermal D (20 keV) plasma are shown, together with the neutron energy spectrum emitted by thermal bulk DT plasma at 20 keV. The neutron energy spectrum corresponding to the classical case contains 5000 events. The FWHM of these three components is 2.3 MeV, 2.6 MeV and 3.6 MeV in cases of classical, $k = 0.75$, $\alpha = -1$ and $k = 0.75$, $\alpha = -4$ slowing down, respectively.

ions at different velocities so that, for example, if $\alpha < 0$ ions with velocities $v > v_b/2$ are preferentially lost.

As shown in [8, 19], equation (4.1) can be solved by standard numerical techniques. The results obtained for an hypothetical ITER neutral beam injection (NBI) scenario in which tritons are injected with energy $E_b = 1$ MeV and pitch angle of 0.5 into a DT plasma (with ion and electron temperature of 20 keV and deuterium and tritium density of 1.0×10^{20} m^{-3}) are shown in figure 11 for three different cases (A–B–C). The classical solution (A) is compared to the anomalous cases (B) and (C) with $k = 0.75$, $\alpha = -1$ and $k = 0.75$, $\alpha = -4$, respectively. For the classic case (figure 11(A)), the ions distribution features a clear anisotropy in the injection energy region. For lower energies instead, the slowing down distribution becomes more isotropic due to the pitch angle scattering caused by collision with bulk ions. When the classic solution is compared to the anomalous cases (figure 11(B)) we note that the anisotropic part is almost unaffected by the loss term $L(f)$, whereas the low energy distribution is less pronounced. This is emphasized in the anomalous slowing down case (figure 11(C)) in which the isotropic distribution at low energies almost disappears due to a lower value of the α exponent which rules the ions dispersion.

Using as input the above simulated tritons velocity distribution, Monte Carlo simulations based on GENESIS code [20] were performed to calculate neutron energy spectra, assuming to have D bulk thermal plasma at 20 keV temperature (see figure 11). Figure 11(D) shows the calculated neutron energy spectra generated by the three NBI distribution cases interacting with the thermal D plasma, together with the thermal bulk DT plasma component (20 keV). Here, the latter is shown as dominant contribution. The thermal component on ITER, in fact, is expected to be between 90% and 95% with respect to the NBI one [21].

In order to study the diagnostic capabilities of the SCD, the classical and the anomalous components viewed from two different angles, together with the thermal contribution, have been convolved with the diamond response function. Figure 12 shows the results in terms of $^{12}C(n,\alpha)^{9}Be$ peak at 90° (top panel A) and 45° (bottom panel B), respectively. The exhibited spectra were normalized in order to have 5000 counts in the classic NBI component whereas in the anomalous cases the number of counts in the NBI components scales with the associated dispersion factor. A counts number equal to 5000 has been chosen according to the expected neutron flux (10^9 n/cm^2/s) at the high resolution neutron spectrometer (HRNS) position [22]. In fact, by considering the diamond

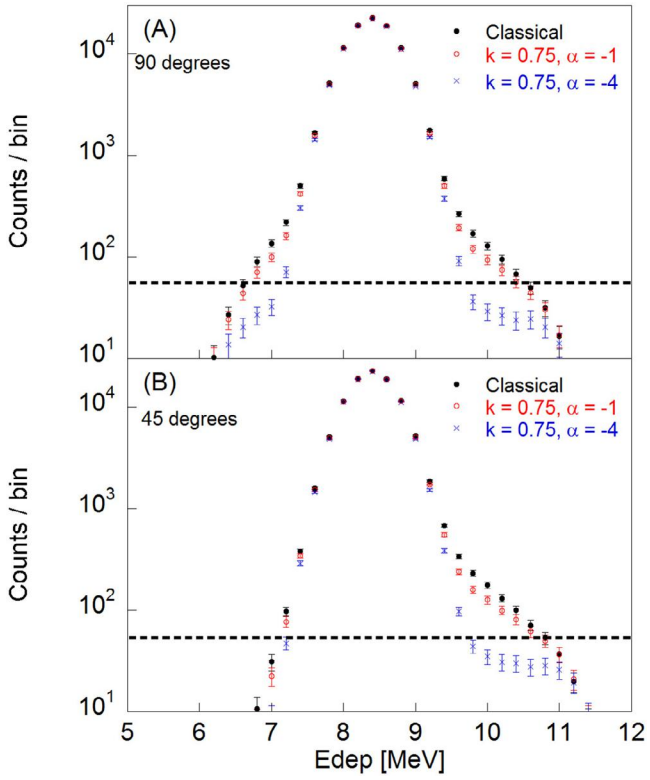

Figure 12. Comparison of the neutron spectra in terms of $^{12}C(n,\alpha)^{9}Be$ peak for the three studied cases after the convolution with diamond response function. The dashed lines represent the level of sensitivity of the SCD. Panel (A) and (B) show the neutron spectra viewed at 90° and 45°, respectively. The y-axis of both the graphs is shown in logarithmic scale.

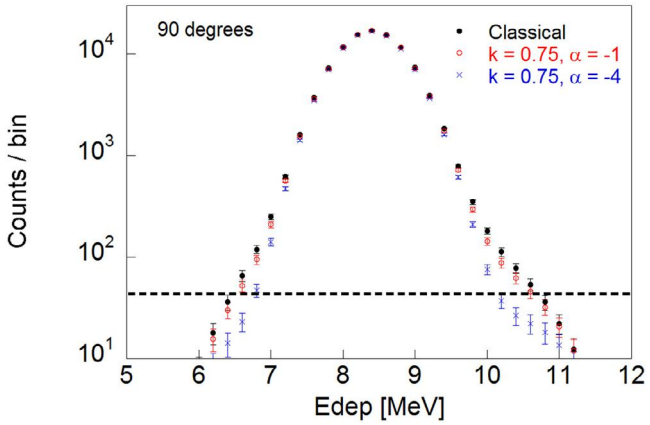

Figure 13. Comparison of the neutron spectra viewed at 90°, in terms of $^{12}C(n,\alpha)^{9}Be$ peak for the 3 studied cases after the convolution with a neutron spectrometer with energy resolution equal to 5% at 14 MeV. The dashed line represents the level of sensitivity of the detector. The *y*-axis is shown in logarithmic scale.

efficiency to 14 MeV neutron to be of about 5×10^{-4} in the n-α peak and the active area of a 12 pixel SCD matrix [7, 10],we can estimate to have on ITER roughly 5000 counts per half second in the classic NBI component at the HRNS position. Consequently, this number is comparable to the number of counts that we can have by integrating for the 1 MeV NB tritons slowing down time, therefore allowing NBI diagnosing. The spectra display a dominant thermal component of about 0.8 MeV FWHM and additional high and low energy tails induced by NBI heating at an amplitude of about 10^{-2} compared to the peak from thermal emission. Compared to the classical slowing down case, the effects of an additional anomalous loss of the beam ions are distinguishable as deviations in the high energy tails of the spectrum at a level above 5×10^{-3} with respect to the main peak. This can be observed with today's sensitivity limit of SCDs. The deviation is better observed at 45° and for the $k = 0.75$, $\alpha = -4$ case. AQ5

In order to study the importance of the high energy resolution enabled by SCDs, in figure 13 we consider the case of an SCD with a poorer energy resolution of 5% at 14 MeV and that views the plasma along a line of sight at 90° with respect to the magnetic field. The dominant thermal DT neutron component has a 1.1 MeV FWHM and the contribution of the NBI component can be separated from the thermal peak at deposited energies $E_d > 10$. When compared to figure 12(A), the spectra have smoother gradients, which makes it harder to observe differences among the classical, $k = 0.75$ $\alpha = -1$ and $k = 0.75$ $\alpha = -4$ cases. The poorer energy resolution results also in a significantly broader spectrum for which the separation of the Thermal and NBI components becomes more difficult.

5. Conclusions

The NGs selected for the JET neutron calibration have been fully characterized and calibrated at the Neutron Metrology Laboratory of the National Physical Laboratory (NPL, Teddington, UK). The unprecedented intrinsic energy resolution (<1% FWHM at 14 MeV) of the SCD neutron spectrometer made possible to resolve for the first time the complex features of the neutron energy spectra resulting from the mixed D/T beam ions reacting with the T/D nuclei present in the target. The dominant NG beam component was found to be the DT molecule. As demonstrated with the detailed analysis of the NG D/T beam composition, the SCDs open up new prospects for diagnosing of DT plasmas, such as for example the studied heuristic case of a non-classical slowing down of the beam ions on ITER DT plasmas. The simulations performed indicate that the diamond detectors would provide good separation of the different neutron components and that information on the NB slowing down can be achieved. AQ6

Acknowledgments

This work has been carried out within the framework of the EUROfusion Consortium and has received funding from the Euratom research and training programme 2014–2018 under grant agreement No 633053. The views and opinions expressed herein do not necessarily reflect those of the European Commission. AQ7

ORCID iDs

D Rigamonti https://orcid.org/0000-0003-0183-0965
M Nocente https://orcid.org/0000-0003-0170-5275

AQ8 ## References

AQ12 [1] Syme D B *et al* 2014 Fusion yield measurements on JET and their calibration *Fusion Eng. Des.* **89** 2766–75

[2] Batistoni P *et al* 2016 Technological exploitation of deuterium–tritium operations at JET in support of ITER design, operation and safety *Fusion Eng. Des* **109–11** 278–85

AQ9 [3] www.vniia.ru

[4] Batistoni P *et al* 14 MeV Calibration of JET neutron detectors—Phase 1: calibration and characterization of the AQ10 neutron source *Nucl. Fusion* submitted

[5] www.mcnp.lanl.gov/

[6] Cufar A *et al* 2017 Calculations to support JET neutron yield calibration: modelling of neutron emission from a compact AQ13 DT neutron generator *Nucl. Instrum. Methods Phys. Res.* A **847** 199–204

[7] Rigamonti D *et al* Capabilities of a diamond detector matrix for neutron spectroscopy measurements at JET AQ11 *PoS(ECPD2015)*

[8] Giacomelli L *et al* 2016 *Rev. Sci. Instrum.* **87** 11D822

[9] Rebai M *et al* 2016 *Rev. Sci. Instrum.* **87** 11D823

[10] Muraro A *et al* 2016 *Rev. Sci. Instrum.* **87** 11D833

[11] Cazzaniga C *et al* 2014 *Rev. Sci. Instrum.* **85** 043506

[12] Nocente M *et al* 2015 *Rev. Sci. Instrum.* **86** 103501

[13] www.e6.com/en/Home

[14] www.cividec.at/

[15] www.caen.it/

[16] Cufar A *et al* Modelling of the neutron production in the mixed beam DT neutron generator *Fusion Eng. Des.* submitted

[17] www.root.cern.ch/

[18] Hellesen C *et al* 2015 *Nucl. Fusion* **55** 023005

[19] Gaffey J D 1976 *J. Plasma Phys.* **16** 149

[20] Tardocchi M *et al* 2011 *Phys. Rev. Lett.* **107** 205002

[21] Eriksson L-G *et al* 2007 *Report on the Task: ICRF, NBI and ITER Diagnostics* TW6-TPDS-DIADEV

[22] Scholz M *et al* 2016 System design description document (DDD) *High Resolution Neutron Spectrometer DDD-PBS 55.BB (Enabled) (22 July 2016)*

[23] Litaudon X *et al* 2017 *Nucl. Fusion* **57** 102001

Acknowledgements

First of all I would like to sincerely thank my supervisor Marco Tardocchi who has been fundamental for the success of this work guiding me during these three fantastic years. You have been a constant source of good incitements and new inputs and I have learned so much things from you! Your passion in neutron and gamma-ray spectroscopy has been contagious for me. My special thanks goes to Prof. Giuseppe Gorini who gave me the opportunity to follow many educational courses and perform experimental activities in many international laboratories.

My colleagues from IFP-CNR and Milano-Bicocca worth a special acknowledgement. In particular thanks to Luca for all the suggestions and for the great moments of hard work and good life that we had mainly at JET. Special thanks to Marica who introduced me in the diamond detectors world and in MCNP simulations. She has always been a good mate during the experimental activities and work travels. Thanks to Massimo because of its precious scientific advice. Many thanks to Andrea, Gabriele and Nicola with whom I shared the office spending good and friendly time both in Milano and in Abingdon. Thanks to Song for the good company and for advice on Chinese food. Thanks to Enrico, Giovanni, Carlo, Giuseppe and Giorgia for the friendly working environment and for all the scientific suggestions. I certainly must acknowledge Valeria and Lorenzo with whom I spent many days working together on the gamma camera project and to Andrea Dal Molin who recently has joined the group. Thanks to Paola with whom I spent many lunch breaks and to Roberta and Giovanni for the administrative help, you have always been very kind with me.

I want also to express my gratitude to Paola Batistoni and Sergey Popovichev who gave me the great opportunity to actively participate in the JET neutron calibration. Thanks to Vasili Kiptily and Joao for their collaboration during the gamma camera upgrade project. Many thanks to Izabella Zychor and the NCBJ group for hosting me in their laboratory for several weeks and for sharing their deep knowledge about Silicon Photomultipliers. Thanks to Mario, Maurizio and Stefano from ENEA-Frascati.

Vorrei ringraziare i miei cari genitori che sono sempre stati una certezza e che vorrei sempre rendere orgogliosi di me. Meritate tutto il meglio. Grazie al mio fratellone che

ammiro e seguo da sempre e grazie ai suoi preziosi consigli mai pretenziosi.

Grazie al mio caro amico Matteo e alla Bea con i quali ho condiviso la nostra Milano, le cene, le serate e i bei momenti. Grazie di nuovo a Matteo per tutti questi anni passati insieme e grazie al Chico e a Morvan sui quali ho la certezza di poter contare. Morvan, non scorderò mai le infinite giornate passate insieme in biblioteca. Grazie a tutti i miei amici, quelli di vecchia data e i più recenti che hanno fatto parte del mio percorso e che hanno lasciato una traccia. Grazie a Pollo e a Roga per i bei momenti passati in università e grazie a Marco e Alessandro con i quali ho condiviso in modo sereno l'appartamento, le serie tv e il pepe nero.

Un grazie gggigante va alla mia amata compagna, Federica, che mi ha tenuto per mano durante questi bellissimi tre anni. GRAZIE.